

UNIVERSITY OF CALIFORNIA

Santa Barbara

Methods of Synthesis of Colloidal Nanoparticles

A Dissertation submitted in partial satisfaction of the
requirements for the degree Doctor of Philosophy
in Inorganic Chemistry

by

Jeffrey A Gerbec

Committee in charge:

Professor Geoffrey F. Strouse, Chairperson

Professor William C. Kaska

Professor Anthony K. Cheetham

Professor Pierre Petroff

March 2006

The dissertation of Jeffrey A. Gerbec is approved.

Professor William C. Kaska

Professor Anthony K. Cheetham

Professor Pierre Petroff

Professor Geoffrey F. Strouse, Committee Chair

March 2006

Methods of Synthesis of Colloidal Nanoparticles

Copyright © 2006

by

Jeffrey A. Gerbec

Acknowledgements

This thesis is dedicated to my family, especially my mom and dad, Bonnie and Dennis. They were always supportive of my goals and wanted nothing less than the best opportunities for me. They have sacrificed a great deal to help me attain my goals. For that I am eternally thankful.

To my wife Karen, thank you for your understanding and support. Over the years of my graduate career, many tests of strength and flexibility have challenged us. Through all the bizarre twists and turns, we still made it. I love you.

A special thanks to my committee, Professors Strouse, Kaska, Cheetham and Petroff. Thank you for the support you have graciously shown me. Your professionalism and honesty has made a lasting impression. One in which I will carry on in my career.

Deedrea, you are an amazing asset to the department. There could never be an equal. Thank you for our conversations during the good times and the bad. You have a gift to know what the right thing to do is in nearly any situation.

To Donny, I am grateful to have known your friendship and company. We have shared many stimulating conversations. If the only advice that I could ever give you when an experiment doesn't seem to work it would be – excite at 400! One more thing, if you ever find yourself in the middle of a quasi Taylor expansion, excuse the pun, substitute A1, A2 and A3 – the expansion will blow your mind.

Greg, I am honored to have had a mentor who could show me how to make lists and prioritize the sub-priorities so that my data analysis could go as efficiently as possible. As per your request, the time was right to kill the legacy with nothing less than a “Viking Funeral”.

Khalid, Kahuna's or Gina's? The indecision will continue until your next visit to SB. Thank you for the friendship and support - SBB in SB!

Travis “penguin smacker” Jennings, I hope that some day you will find intellectual stimulation beckoning you to attend a collegiate football game. Go Seminoles!

I have had many wonderful opportunities to meet researchers from all over the world. Tomohide and Takeshi, it was fun working with you – kampai! Tegi “home boy” Kim, I hope to see you again in Japan soon. Susanthri, I hope you have found happiness, you deserve it.

And to all the other people whom I have come to know during my graduate education, each and every one has been a strikingly memorable experience.

Curriculum Vitae

Education

- 9/2001 to 3/2006
University of California, Santa Barbara, California, PhD. in Chemistry,
Thesis: Methods of Synthesis of Colloidal Nanoparticles
Research Advisor: Prof. Geoffrey F. Strouse
- 8/1998 to 5/2001
California State University, Chico, California, B. S. in Chemistry
Advisor: Prof. David Ball
- 6/1995 to 5/1998
Shasta College, Redding, California, General Education

Work Experience

- | | |
|----------------|--|
| 8/05 – Current | Post Doctoral Research Engineer
<i>Mitsubishi Chemical - Research and Innovation Center,
Goleta, California</i> |
| 3/04 - 6/05 | Visiting Researcher
<i>Department of Chemistry, The Florida State University,
Tallahassee, FL</i> |
| 7/03 – 3/04 | Research Assistant – Mitsubishi Chemical Center for
Advanced Materials
<i>Department of Chemistry, University of California, Santa
Barbara, California</i> |
| 1/03 – 6/03 | ESI/Mass Spec Teaching Assistant
<i>Department of Chemistry, University of California, Santa
Barbara, California</i> |
| 11/99 – 8/01 | Student Assistant
<i>California DOJ, Bureau of Forensic Science, Chico, California</i> |
| 5/99 – 9/99 | Extractions Analyst
<i>Columbia Analytical, Redding, California</i> |

Teaching Experience

- 9/02 – 12/02 Cooperative Chemistry Laboratory
Department of Chemistry, University of California, Santa Barbara, California
- 9/01 – 6/02 General Chemistry Laboratory
Department of Chemistry, University of California, Santa Barbara, California

Undergraduates Advised

- 1/05 – 8/05 Mark Blazer, *Florida State University*
- 11/04 – 7/05 Hina Patel, *University of California, Santa Barbara*

Research Skills

- Synthesis of II-VI and III-V binary and ternary inorganic colloidal semiconductor nanoparticles for phosphor applications by microwave methods.
- Synthesis of high refractory colloidal nanoparticles.
- Use of Dynamic Light Scattering (DLS) to characterize size and polydispersities of colloids and micelles.
- Surface functionalization of nanoparticles with inorganic/organic shells and organic ligands.
- Characterization of size, shape and phase of nanoparticles by powder X-Ray diffraction.
- Imaging of inorganic materials by high resolution transmission electron microscopy (HRTEM).
- Surface characterization of inorganic materials by:
 - ATR-IR, FT-IR.
 - X-Ray Photoelectron Spectroscopy (XPS).
- Elemental analysis by atomic absorption, emission spectroscopy and X-ray fluorescence spectroscopy.

Awards

Distinguished Graduate Fellow 2003 - Mitsubishi Chemical Center for Advanced Materials

Research Publications

- (1) *Rapid Formation of Highly Luminescent Nanoparticles in Superheated Solvents*, Strouse, G.F.; Gerbec, J.A., Patent Pending
- (2) *Method for Synthesis of Colloidal Nanoparticles*, Strouse, G.F.; Gerbec, J.A.; Magana, M., Patent Pending
- (3) *Microwave-Enhanced Reaction Rates for Nanoparticle Synthesis*, Gerbec, J.A.; Strouse, G.F., Journal of the American Chemical Society, Published on the web ASAP
- (4) *Linear programming of inlet pressure or flow-rate in isothermal gas chromatography with near-vacuum outlet pressure*, Nahir, T. M.; Gerbec, J. A., Journal of Chromatography, A (2001), 915(1-2), 265-270

Research Presentations

Doped Nanophosphors: An Industrial Perspective
1st International Workshop on Doping Semiconductor Nanostructures
Naval Research Laboratory, Washington D.C., January 9-11, 2006

Enhanced Nanocrystal Properties Through Microwave Chemistry, Invited Talk,
CEM/ISCO Seminar – Advances in Microwave Chemistry, San Diego, CA
November 2-3, 2005

Retention times in isothermal pressure-programmed gas chromatography.
Gerbec, Jeffrey A.; Nahir, Tal M., Abstracts of Papers, 221st ACS National Meeting, San Diego, CA, United States, April 1-5, 2001

ABSTRACT

Methods of Synthesis of Colloidal Nanoparticles

By

Jeffrey A. Gerbec

Colloidal semiconductor nanocrystals, with unique size-dependent optical properties, have great promise for integration into next generation technologies including solid-state lighting and biological labeling. A general method of reproducible, large scale and environmentally safe synthetic preparation becomes crucial for integration in commercial devices. In addition to the synthetic protocol, an understanding of the surfaces of the as prepared material is critical for obtaining a high quantum yield that is stable for long periods of time in ambient conditions. In this dissertation, a new synthetic approach to general colloidal nanocrystals is presented. Microwave heating of molecular precursors increases the rate of reaction from days to minutes for a host of nanomaterials. The most relevant for the study of inorganic phosphors is CdSe and InP and their respective ternary analogs. Post synthetic surface treatment of the as prepared material show a tremendous increase in the QY for as prepared InP and InGaP. Post synthetic surface treatment is carried out by photoactivated etching with dilute HF. In the case of InGaP, the QY reaches 0.80

from 0.05 in a matter of minutes. Other surface treatment strategies that address the stability is carried out by forming epitaxial core shell structures. It is shown that using ZnS as a wide band gap shelling material, the QY of InP reaches 0.42 in solution and is stable for months. These are significant steps toward the engineering of semiconductor quantum dot phosphors for solid state lighting and biological labeling.

Table of Contents

Chapter 1. General Introduction	1
1.1 Introduction	1
1.2 Thesis Overview	4
1.3 Introduction to Colloidal Semiconductor Nanocrystals	5
1.4 Nanomaterial Synthesis	11
1.4.1 Lyothermal Synthetic Routes	11
1.4.2 Microwave Synthesis	14
1.5 References	19
Chapter 2. The Colloidal Nanoparticle Reaction System	24
2.1 The Reaction System	24
2.2. Solvent Effect	30
2.3. Ionic Liquids	34
2.4 References	38
Chapter 3. Parallel Synthetic Methods for Colloidal Nanoparticles	42
3.1 Introduction	42
3.2. Experimental Methods	45
3.3 Results and Discussion	47
3.3.1 Parallel Synthesis of CdSe Nanoparticles from	
$\text{Li}_4[\text{Cd}_{10}\text{Se}_4(\text{SPh})_{16}]$	47
3.3.2 Parallel Synthesis of InGaP Nanoparticles	51

3.4 Conclusion	53
3.5 References	53
Chapter 4. Microwave Enhanced Reaction Rates for Nanoparticle Synthesis	55
4.1 Introduction	55
4.2 Experimental Methods	56
4.3 Results and Discussion	61
4.3.1 Growth of CdSe by $\text{Li}_4[\text{Cd}_{10}\text{Se}_4(\text{SPh})_{16}]$	71
4.3.2 Growth of CdSe by $\text{Li}_4[\text{Cd}_{10}\text{Se}_4(\text{SPh})_{16}]$ with 1-hexyl-3-methylimidazolium	74
4.3.3 Growth of CdSe by CdO	77
4.3.4 Growth of InGaP	79
4.3.5 Growth of InP with Ionic Liquids	83
4.4 Conclusion	86
4.5 References	88
Chapter 5. Formation Characteristic and Photochemical Etching of InGaP	92
5.1 Introduction	92
5.2 InGaP Size Tunability	93
5.3 InGaP and InP Photochemical Etching	97
5.4 Formation and etching of $\text{In}_{1-x}\text{Ga}_x\text{P}$	105
5.5 Conclusion	114
5.6 References	114

Chapter 6 III-V core/shell heterostructures	119
6.1 Introduction	119
6.2 Synthesis of Core/Shell Nanoparticle Heterostructures	122
6.3 Experimental Methods.	125
6.3.1 Introduction.	125
6.3.2 Preparation of InGaP/ZnS.	125
6.3.3 Preparation of InGaP/GaP and InGaP/GaN	128
6.3.4 Preparation of InP/ZnS	129
6.4 InGaP/ZnS Heterostructures	130
6.5 InGaP/GaP and InGaP/GaN Heterostructures	138
6.6 InP/ZnS Heterostructures	140
6.7 Conclusion	147
6.8 References	148
Chapter 7. Synthesis of Wide Band Gap Semiconductors Nanoparticles by microwave heating	152
7.1 Introduction	152
7.2 Experimental Methods	154
7.3 Synthesis of Ga ₂ O ₃	156
7.4 Synthesis of In ₂ O ₃	158
7.5 Synthesis of Oxynitrides	161
7.6 Conclusion	168
7.7 References	169

Chapter 1. General Introduction

1.1 Introduction

Development of new phosphors capable of being pumped by blue light emitting diodes for alternative display and lighting strategies based on photon down conversion has become a desirable target in greener alternatives to mercury based lighting¹⁻⁵ (fluorescent bulb technology). Down conversion phosphors require high quantum yields ($> 40\%$) to be competitive with existing Hg and Xe lamp based technologies. In addition for LED pumping, the phosphor must efficiently absorb photons in the 400-420 nm (GaN LED based pump source) range and convert the photon energy into blue (450 nm), green (540 nm), and red (610 nm) light to be commercially viable, as well as operate at 150°C due to the operating temperature of standard LEDs. Commercialization of efficient phosphors based on re-engineered classical ion doped oxide or sulfide materials is difficult due to the major hurdle of optimized coupling to blue LEDs. An alternative approach which is viable is the development of white-light phosphors based on semiconductor nanocrystals⁶⁻⁹ that take advantage of the high QE of the current LEDs ($> 50\%$), the broad absorption range of nanocrystals, coupled to the tunability of color achievable for high quantum yield nanoscale semiconductors (figure 1.1) ($\text{QE} > 70\%$). The potential for use of nanocrystalline semiconductors, whose energy is tunable due to particle-in-the-box behavior for materials whose Bohr radius is on the order of 10 nm^{10} has been identified as a critical target in this area. The tunability of color for nanocrystalline

1.2 Thesis Overview

In recent years, research in nanoscale materials has received much attention in part to elucidate size dependant electronic properties, shape characteristics and physical properties. This thesis describes alternative methods for rapid and reproducible semiconductor colloidal nanoparticle formation, as well as post synthetic treatment to obtain room temperature photoluminescent quantum yields (PLQY) up to 0.80 for III-V InGaP colloidal quantum dots.

The first part of the thesis is devoted to the foundation of manipulating inorganic precursors by microwave heating to effectively heat the bulk solution. This approach eliminates thermal gradients allowing more uniform nucleation of nanocrystalline seeds. Microwave methods can be used for existing literature methods and novel green synthetic routes by increased pressure to obtain a PLQY of 0.15 for pre-etched InGaP which is the highest reported to date. The PLQY of post chemical etching is 0.80

The second part of this thesis describes a photo-assisted etching method of III-V semiconductor colloids that can increase the quantum efficiency to a value of 0.80, which is greater than the current literature reports of 0.40. III-V nanomaterials are classically difficult to grow by solution phase chemistry and in bulk thin films due the propensity of the precursors to oxidize and the high activation energy of the growing nanocrystalline colloids. Traditional synthetic methods result in as prepared material that do not exhibit large room temperature photoluminescent quantum yields (PLQY).

Surface modification such as photo-assisted etching has been demonstrated to remove surface defects and fill surface vacancies to increase the band edge luminescence to a maximum of 0.40. In our effort, we have been able to achieve QY's on the order of 0.80 following ambient near UV photo-assisted etching.

The third part of this thesis is devoted to the stabilization of InP and InGaP colloids by core-shelling approaches which puts a high bandgap inorganic passivating layer over the emitting core nanoparticle. The inclusion of the inorganic shell enhances the quantum yield and protects the core particles from surface oxidation which ultimately reduces the PLQY and the material solubility. Native oxidation occurs readily in bulk semiconductors and has been observed to be a significant problem in nanocrystals where owing to the fact that atoms in nanomaterials of a few nanometers in diameter are mostly surface, the entire particle readily oxidizes. Surface stabilization is ultimately the most significant factor for maintaining a high PLQY in ambient conditions such as air and water.

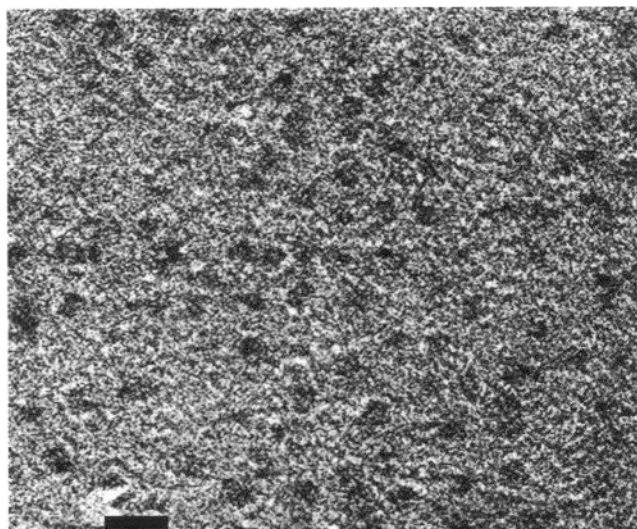
The fourth part of this thesis outlines new synthetic approaches toward colloidal materials for blue and near UV phosphors such as Ga_2O_3 and In_2O_3 . Oxides of indium and gallium are wide band gap semiconductors that have the potential to be used for the near UV PL. In addition, synthesis of other rare colloidal materials that could be used for near UV phosphors Like InN and GaN was attempted.

1.3 Introduction to Colloidal Semiconductor Nanocrystals

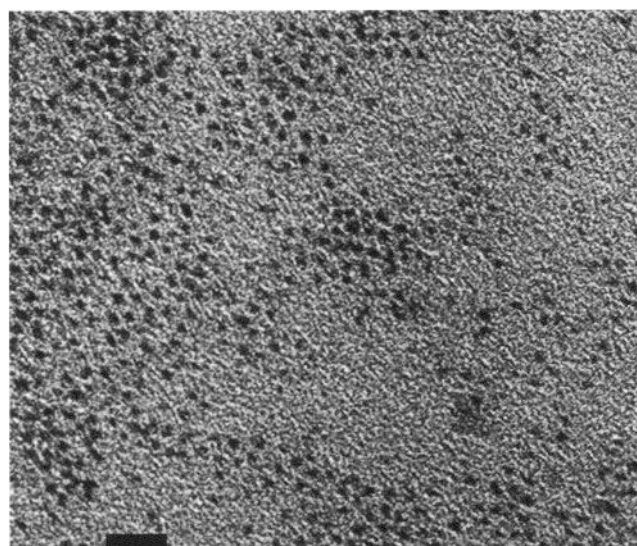
The field of nanomaterials is comprised of a wide range of materials that exhibit size-dependent physical properties including metallic, semiconductor or mixed metal cores. Of greatest interest is the class of semiconducting nanocrystals that are strongly emitting. These nanocrystal colloids are composed of an inorganic core surrounded by an organic shell¹⁸. The organic shell can be composed of long chain alkyl amines or carboxylic acids in which the functional group is bound to the surface of the inorganic core analogous to a metal-ligand interaction in a coordination compound. The strength of the passivant binding can be related to the hardness-softness of the nanocrystal metal component in conjunction with the ligand head group basicity in analogy to Pearson soft-hard acid base theory in Inorganic Chemistry^{19, 20}.

Figures 1.2 and 1.3 depict an ensemble of InGaP quantum dots and a high resolution image of a single quantum dot, respectively. A transmission electron micrograph generates a two dimensional image. The dark areas contrasted against the grey background represent diameters of individual colloidal crystallites. The crystalline inorganic core is resolved in figure 1.3.

The physical dimensions of materials are of fundamental importance and can determine the properties by quantum-confinement effects²¹⁻²³ as the size is reduced below the effective Bohr radius of the materials, in essence their Brillouin zone. As a class of materials nanomaterials can be subdivided into particles and crystals, where nanocrystals represent a sub-class of defect free perfectly formed materials in the



10 nm



20 nm

Figure 1.2. TEM of an ansamble of colloidal InGaP quantum dots grown by microwave methods. The material is deposited on holy carbon coated 400 mesh copper grids.

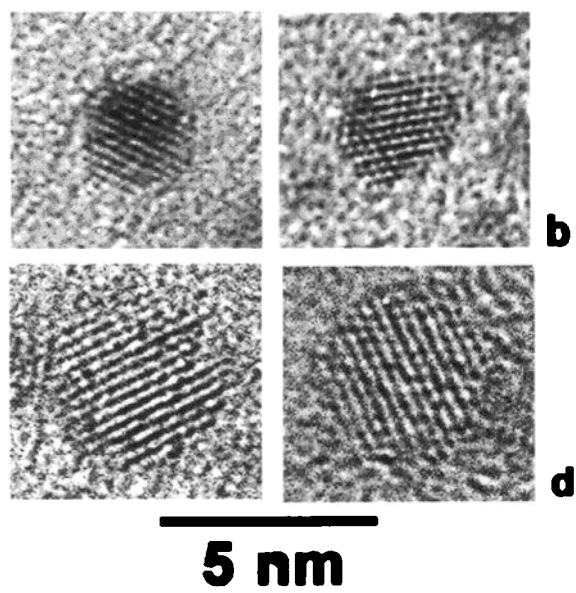


Figure 1.3. (a, b) TEM of 2.5 nm and (c, d) 4.3 nm InGaP quantum dots grown by microwave methods.

nanometer size regime (dimensions less than 100 nm). For well-formed nanocrystals, as the size of the material approaches the Bohr radius, in other words the volume occupied by the electron-hole pair of the exciton, they experience quantum confinement as described by a simple particle in a 3-dimensional box^{10, 24-26}. The result is a shift in the optical properties and electronic levels following the enhanced Coulombic repulsion which follows a quadratic expression. Materials that exhibit quantum confinement are often referred to as quantum dots to distinguish them from merely nano-crystals or nanoparticles.

When the physical dimensions of a semiconductor is smaller than the Bohr radius of the bulk material the electron and hole separation become confined to discrete energy levels giving rise to a separation of the valence and conduction band to higher energy with increasing degree of quantum confinement^{10, 27, 28} (smaller physical dimensions of the material). The size dependant photoluminescence is depicted in figure 2 for two sizes of InGaP, 2nm (green) and 4.5nm (red) respectively. The size tunable electronic properties in the semiconductors are what make CdSe and InP quantum dots so attractive as solid state phosphors. In fact, it is predicted that semiconducting phosphors will be 50% more efficient than tradition phosphors YAG:Ce used in today's lighting technologies

For these materials to be realized, engaging and rewarding challenges need to be overcome before commercial devices such as solid state lighting are realized. Some of the significant challenges are stability and reactivity, the physics of

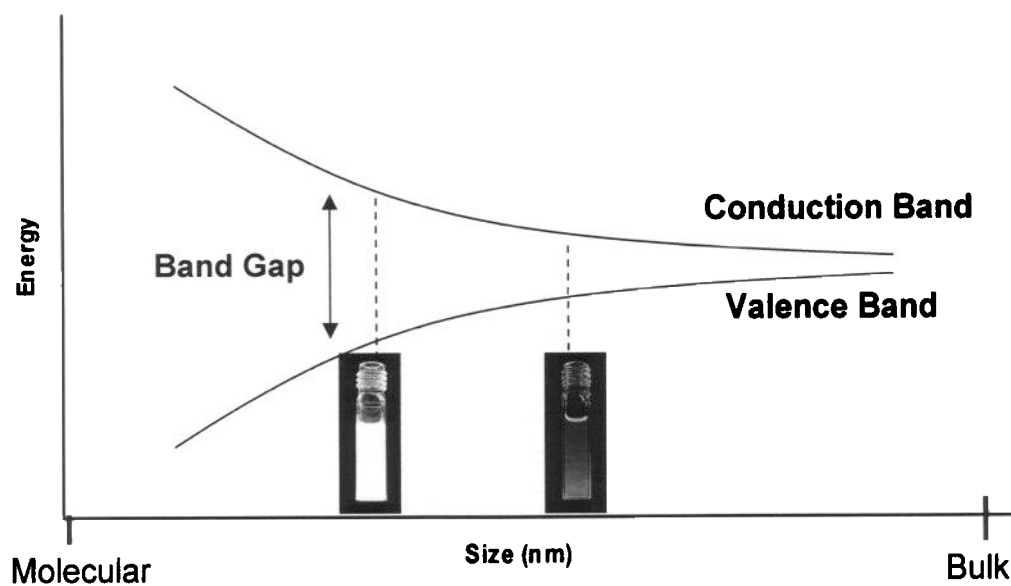


Figure 1.4. Depiction of the size dependant photoluminescence of InGaP quantum dots. As the quantum dot diameter increases from 2 nm (green) to 4.5 nm (orange/red), the band gap energy decreases.

nanoscale materials, control and formation of nanomaterials and high throughput synthesis.

1.4 Nanomaterial Synthesis

1.4.1 Lyothermal Synthetic Routes

Since the early 1990's, a plethora of synthetic approaches have been published for the formation of CdSe nanoparticles. CdSe colloidal nanoparticles have been studied extensively over the past 15 years as the quintessential nanomaterial showing a high degree of crystallinity and size-dependent physical properties that scale well with theoretical predictions. Since the physical properties of nanocrystalline materials are highly dependant on size, the goal of every nanomaterial synthetic methodology is to yield highly crystalline core nanoparticles that are well passivated by organic ligands, and exhibits very narrow size distributions. The foundation of the current lyothermal methods are based on the work of Murray et al²⁹.

In the original work the strategy relied on the separation of nucleation and growth, as well as control over thermodynamics by use of kinetic barriers through the addition of strongly passivating back bonding ligands. The general method involved a rapid injection of the precursors was performed in a hot coordinating solvent, trioctylphosphine oxide (TOPO). Volatile organometallic precursors, Me_2Cd and tri-n-octylphosphineselenide (TOPSe), were chosen so that they would readily decompose to form uniform nuclei which could grow by addition of monomers of Cd

and Se. In this reaction, the precursors were injected at 300°C and the nanocrystals were grown between 280 and 300°C. By this method highly crystalline CdSe nanoparticles could easily be obtained over a range of sizes with narrow size distributions. While this method is adequate, it proved to be expensive, dangerous and not readily transferable to other systems. More importantly it had limited industrial application for producing large the needed scales of g→ Kg quantities of materials that could be reproducibly prepared.

Peng et al.³⁰ later modified the work of Murray to enhance the size distributions and utilize a more chemically stable precursor such as CdO or Cd(OAc)₂. Peng and other researchers work revealed that shape³¹, size distribution³² and PLQY³³⁻³⁵ are highly dependent on the choice of coordinating solvent, whether it be aliphatic amines or acids. The size distribution was improved in these examples, however; due to an injection temperature of 350°C. The technology has limited flexibility for synthesis of new materials and has poor scalability for industrial production. Other synthetic approaches which have been developed such as inverse micelle^{18, 27}, redox^{36, 37} and aqueous microwave synthesis³⁸, and single source precursor approaches³⁹⁻⁴³ have their respective drawback for material quality. The inverse micelle method does not generally yield monodisperse or highly crystalline colloids. Aqueous microwave synthesis is rapid, on the order of minutes, but the size distribution is poor and the colloids are not well passivated by organic ligands. Single source precursor routes have the potential to yield gram quantities, but the reaction rates are on the order of days. Neglecting the fact that II-VI materials are

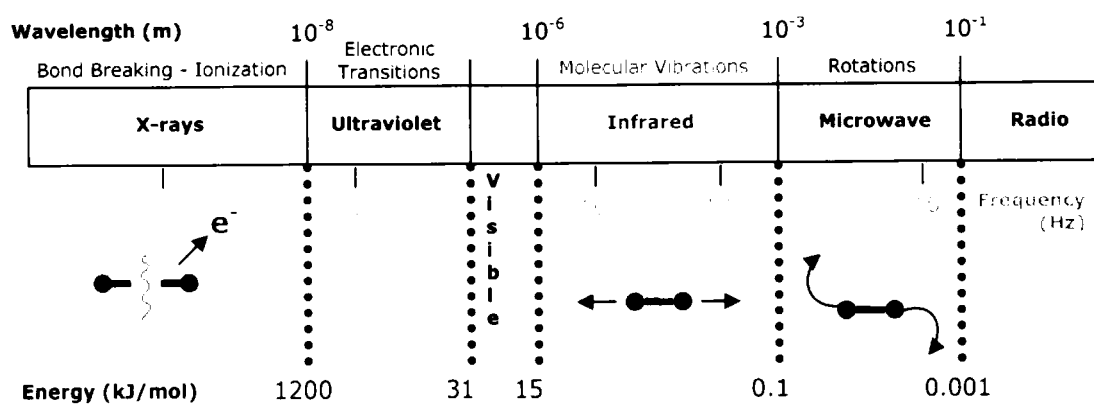


Figure 1.5. Illustration of the degree of molecular interaction with various energies within the electromagnetic spectrum.

unlikely to be commercially integrated into devices, the general method of rapid preparation of high quality, large quantity colloidal semiconductors is lacking and forms the basis of this research effort

1.4.2 Microwave Synthesis

Microwave heating has evolved over the past 50 years from its genesis as high power communications to small convenient systems to rapidly heat liquids and material intrinsically. From the onset of the household microwave in the late 80's, it slowly found uses in chemistry by rapidly heating solvents⁴⁴⁻⁴⁶. Microwaves are low in energy compared to x-rays and the ultraviolet region which is associated with ionization and electronic transitions as depicted in figure 1.5.

Since the mid 1990's, publications citing microwave synthesis has grown exponentially^{35, 47-50}. Much of success has derived from industrial microwaves that are designed specifically for synthetic chemists such as focused microwave, continuous wave and multi-sample automation. Some of the major caveats of microwave synthesis are enhanced reaction rates⁴⁷, greater selectivity^{46, 51, 52} and solvent free reaction⁵³. As stated previously, the energy of microwaves at 2.45 GHz is very low. The energy supplied is much too low to interfere with molecular bonding. For example, the energy supplied to a molecule at 300W of power is calculated to be 0.012 kcal/mol which is far less energy to cleave a typical C-H bond which is on the order of 120 kcal/mol. One explanation to the observed reaction rate increase is the effect of instantaneous heating. Once the sample is irradiated with microwaves the

microscopic temperature is instantly elevated⁵⁴⁻⁵⁶. This may give the reactants an additional driving force to surpass the activation barrier⁵⁶. Another possibility is the coupling efficiency of intermediate states may be much higher than that of the reactant or product.

Not all materials will interact with microwaves effectively to generate heat. Figure 1.6 depicts the ability of a substance to convert microwaves at 2.45 GHz to thermal energy (dielectric loss) as a function of microwave absorption. Insulators are typically transparent at the standard frequency for heating like titania, alumina and quartz. Materials or a molecule that contains polar moieties or polarizability have higher losses than insulators because of the coupling efficiency. For example, water is the classic example because of its characteristic dipole. Molecules with polar functional groups like alcohols, acids and aldehydes typically exhibit high losses. In addition, substances that form ions will couple with microwaves very effectively to produce heat. The displacement of the cation and anion with the phase of the incidence microwave will effectively increase the reaction temperature by the

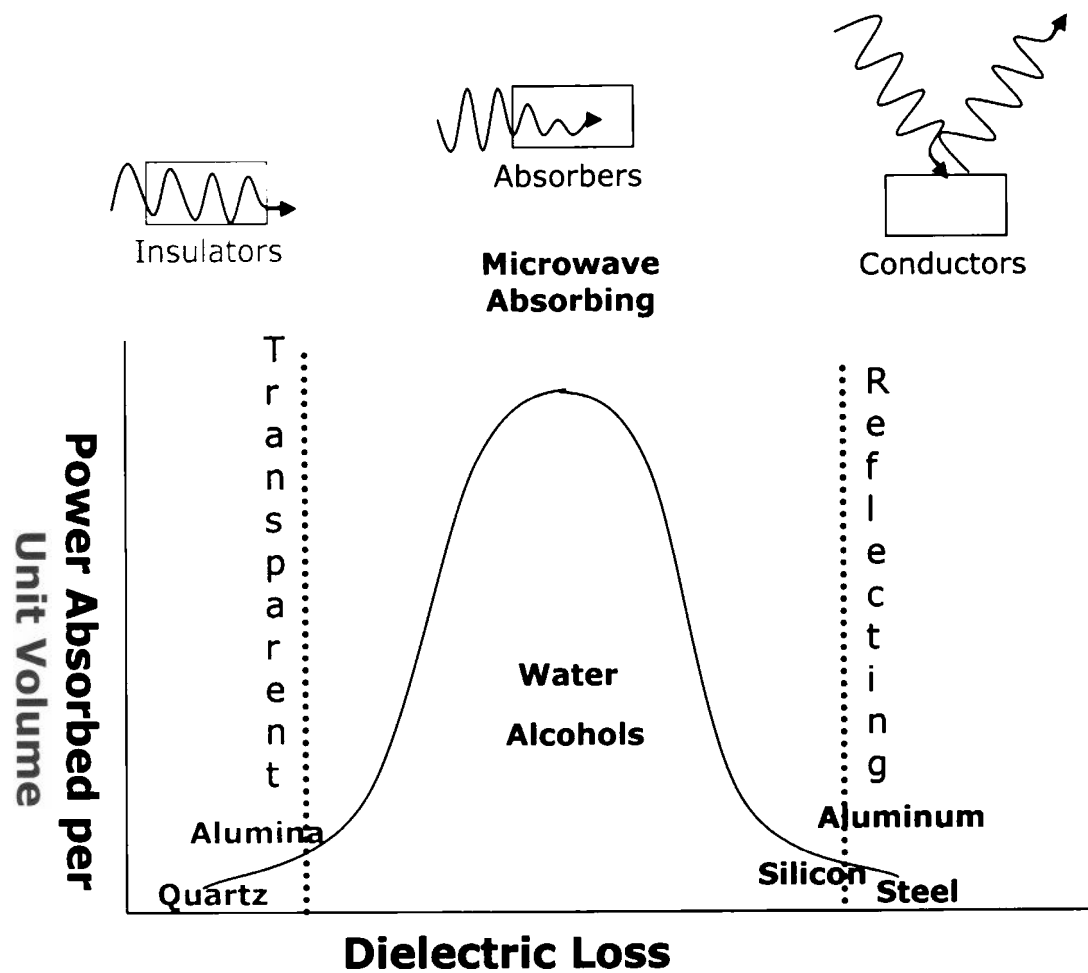


Figure 1.6. Graph depicting selected materials dielectric loss as a function of absorbed microwave power.

conduction mechanism⁴⁶. These mechanisms and the associated theory will be covered in detail in chapter 3. Conversely, conductors such as steel, aluminum and silicon reflect microwaves.

A unique advantage of microwaves that is not readily apparent is the ability to remove latent heat from the reaction allowing a higher thermal input per volume without gradients forming or hot spot formation in large reactions. The efficiency of microwave reaction can sometimes be enhanced further by a process that removes latent heat from the bulk solution where by the incident power is maintained at an elevated level, as seen in figure 1.7. This process is called active cooling⁵⁶. This allows the microscopic temperature to be elevated even higher.

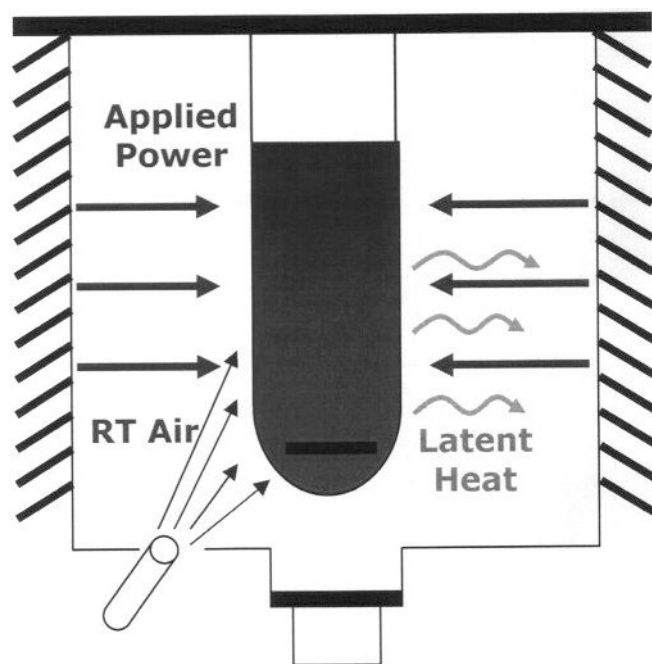


Figure 1.7. Illustration of a microwave reaction undergoing active cooling.

1.5 References

1. Levinshtein, M. E.; Shklovskii, B. I.; Shur, M. S.; Efros, A. L., *Zhurnal Eksperimentalnoi I Teoreticheskoi Fiziki* **1975**, 69, (1), 386-392.
2. Tsao, J. Y., *Ieee Circuits & Devices* **2004**, 20, (3), 28-37.
3. D'Andrade, B. W.; Forrest, S. R., *Advanced Materials* **2004**, 16, (18), 1585-1595.
4. Steigerwald, D. A.; Bhat, J. C.; Collins, D.; Fletcher, R. M.; Holcomb, M. O.; Ludowise, M. J.; Martin, P. S.; Rudaz, S. L., *Ieee Journal of Selected Topics in Quantum Electronics* **2002**, 8, (2), 310-320.
5. Edwards, J. O.; Pearson, R. G., *Journal of the American Chemical Society* **1962**, 84, (1), 16-&.
6. Boilot, J. P.; Gacoin, T.; Lahlil, K.; Buissette, V.; Giaume, D.; Matheron, M., *Actualite Chimique* **2005**, 77-81.
7. Zachau, M.; Konrad, A., Nanomaterials for lighting. In *Functional Nanomaterials for Optoelectronics and Other Applications*, 2003; Vol. 99-100, pp 13-18.
8. Bhargava, R. N.; Chhabra, V.; Som, T.; Ekimov, A.; Taskar, N., *Physica Status Solidi B-Basic Research* **2002**, 229, (2), 897-901.
9. Bhargava, R. N., *Journal of Luminescence* **1997**, 72-4, 46-48.
10. Cava, R. J.; DiSalvo, F. J.; Brus, L. E.; Dunbar, K. R.; Gorman, C. B.; Haile, S. M.; Interrante, L. V.; Musfeldt, J. L.; Navrotsky, A.; Nuzzo, R. G.; Pickett, W. E.; Wilkinson, A. P.; Ahn, C.; Allen, J. W.; Burns, P. C.; Ceder, G.; Chidsey, C. E. D.; Clegg, W.; Coronado, E.; Dai, H. J.; Deem, M. W.; Dunn, B. S.; Galli, G.; Jacobson, A. J.; Kanatzidis, M.; Lin, W. B.; Manthiram, A.; Mrksich, M.; Norris,

- D. J.; Nozik, A. J.; Peng, X. G.; Rawn, C.; Rolison, D.; Singh, D. J.; Toby, B. H.; Tolbert, S.; Wiesner, U. B.; Woodward, P. M.; Yang, P. D., *Progress in Solid State Chemistry* **2002**, 30, (1-2), 1-101.
11. Brus, L., *Journal of Physical Chemistry* **1986**, 90, (12), 2555-2560.
 12. Hirata, G. A.; Ramos, F. E.; McKittrick, J., *Optical Materials* **2005**, 27, (7), 1301-1304.
 13. Orita, K.; Tamura, S.; Takizawa, T.; Ueda, T.; Yuri, M.; Takigawa, S.; Ueda, D., *Japanese Journal of Applied Physics Part 1-Regular Papers Short Notes & Review Papers* **2004**, 43, (8B), 5809-5813.
 14. Haerle, V.; Hahn, B.; Kaiser, S.; Weimar, A.; Bader, S.; Eberhard, F.; Plossl, A.; Eisert, D., *Physica Status Solidi a-Applied Research* **2004**, 201, (12), 2736-2739.
 15. Gessmann, T.; Schubert, E. F., *Journal of Applied Physics* **2004**, 95, (5), 2203-2216.
 16. Mueller-Mach, R.; Mueller, G. O.; Krames, M. R.; Trottier, T., *Ieee Journal of Selected Topics in Quantum Electronics* **2002**, 8, (2), 339-345.
 17. Mueller, A. H.; Petruska, M. A.; Achermann, M.; Werder, D. J.; Akhadow, E. A.; Koleske, D. D.; Hoffbauer, M. A.; Klimov, V. I., *Nano Letters* **2005**, 5, (6), 1039-1044.
 18. Steigerwald, M. L.; Alivisatos, A. P.; Gibson, J. M.; Harris, T. D.; Kortan, R.; Muller, A. J.; Thayer, A. M.; Duncan, T. M.; Douglass, D. C.; Brus, L. E., *Journal of the American Chemical Society* **1988**, 110, (10), 3046-3050.
 19. Pearson, R. G., *Science* **1966**, 151, (3707), 172-&.

20. Pearson, R. G., *Journal of the American Chemical Society* **1963**, 85, (22), 3533
21. Efros, A. L.; Rosen, M., *Annual Review of Materials Science* **2000**, 30, 475-521.
22. Ekimov, A. I.; Efros, A. L.; Onushchenko, A. A., *Solid State Communications* **1985**, 56, (11), 921-924.
23. Efros, A. L.; Efros, A. L., *Soviet Physics Semiconductors-Ussr* **1982**, 16, (7), 772-775.
24. Rossetti, R.; Hull, R.; Gibson, J. M.; Brus, L. E., *Journal of Chemical Physics* **1985**, 83, (3), 1406-1410.
25. Rossetti, R.; Ellison, J. L.; Gibson, J. M.; Brus, L. E., *Journal of Chemical Physics* **1984**, 80, (9), 4464-4469.
26. Rossetti, R.; Nakahara, S.; Brus, L. E., *Journal of Chemical Physics* **1983**, 79, (2), 1086-1088.
27. Alivisatos, A. P.; Harris, A. L.; Levinos, N. J.; Steigerwald, M. L.; Brus, L. E., *Journal of Chemical Physics* **1988**, 89, (7), 4001-4011.
28. Chestnoy, N.; Harris, T. D.; Hull, R.; Brus, L. E., *Journal of Physical Chemistry* **1986**, 90, (15), 3393-3399.
29. Murray, C. B.; Norris, D. J.; Bawendi, M. G., *Journal of the American Chemical Society* **1993**, 115, (19), 8706-8715.
30. Peng, Z. A.; Peng, X. G., *Journal of the American Chemical Society* **2001**, 123, (1), 183-184.
31. Peng, X. G.; Manna, L.; Yang, W. D.; Wickham, J.; Scher, E.; Kadavanich, A.; Alivisatos, A. P., *Nature* **2000**, 404, (6773), 59-61.

32. Peng, X. G.; Wickham, J.; Alivisatos, A. P., *Journal of the American Chemical Society* **1998**, 120, (21), 5343-5344.
33. Donega, C. D.; Hickey, S. G.; Wuister, S. F.; Vanmaekelbergh, D.; Meijerink, A., *Journal of Physical Chemistry B* **2003**, 107, (2), 489-496.
34. Talapin, D. V.; Rogach, A. L.; Shevchenko, E. V.; Kornowski, A.; Haase, M.; Weller, H., *Journal of the American Chemical Society* **2002**, 124, (20), 5782-5790.
35. Loupy, A.; Petit, A.; Hamelin, J.; Texier-Boullet, F.; Jacquault, P.; Mathe, D., *Synthesis-Stuttgart* **1998**, (9), 1213-1234.
36. Tang, J.; Fabbri, J.; Robinson, R. D.; Zhu, Y. M.; Herman, I. P.; Steigerwald, M. L.; Brus, L. E., *Chemistry of Materials* **2004**, 16, (7), 1336-1342.
37. Tang, J.; Redl, F.; Zhu, Y. M.; Siegrist, T.; Brus, L. E.; Steigerwald, M. L., *Nano Letters* **2005**, 5, (3), 543-548.
38. Liang, L.; Qian, H. F.; Ren, J. C., *Chemical Communications* **2005**, (4), 528-530.
39. Raola, O. E.; Strouse, G. F., *Nano Letters* **2002**, 2, (12), 1443-1447.
40. Pickett, N. L.; O'Brien, P., *Chemical Record* **2001**, 1, (6), 467-479.
41. Obrien, P.; Walsh, J. R.; Watson, I. M.; Hart, L.; Silva, S. R. P., *Journal of Crystal Growth* **1996**, 167, (1-2), 133-142.
42. Nair, P. S.; Radhakrishnan, T.; Revaprasadu, N.; Kolawole, G. A.; O'Brien, P., *Chemical Communications* **2002**, (6), 564-565.
43. Cumberland, S. L.; Hanif, K. M.; Javier, A.; Khitrov, G. A.; Strouse, G. F.; Woessner, S. M.; Yun, C. S., *Chemistry of Materials* **2002**, 14, (4), 1576-1584.

44. Langa, F.; DelaCruz, P.; DelaHoz, A.; DiazOrtiz, A.; DiezBarra, E.,
Contemporary Organic Synthesis **1997**, 4, (5), 373-386.
45. Smith, F. E.; Arsenault, E. A., *Talanta* **1996**, 43, (8), 1207-1268.
46. Caddick, S., *Tetrahedron* **1995**, 51, (38), 10403-10432.
47. Lew, A.; Krutzik, P. O.; Hart, M. E.; Chamberlin, A. R., *Journal of
Combinatorial Chemistry* **2002**, 4, (2), 95-105.
48. Lidstrom, P.; Tierney, J.; Wathey, B.; Westman, J., *Tetrahedron* **2001**, 57, (45),
9225-9283.
49. Larhed, M.; Hallberg, A., *Drug Discovery Today* **2001**, 6, (8), 406-416.
50. Rao, K. J.; Vaidhyanathan, B.; Ganguli, M.; Ramakrishnan, P. A., *Chemistry of
Materials* **1999**, 11, (4), 882-895.
51. Perreux, L.; Loupy, A., *Tetrahedron* **2001**, 57, (45), 9199-9223.
52. Mingos, D. M. P.; Baghurst, D. R., *Chemical Society Reviews* **1991**, 20, (1), 1-47.
53. Dittmer, D. C., *Chemistry & Industry* **1997**, (19), 779-&.
54. Jones, D. A.; Lelyveld, T. P.; Mavrofidis, S. D.; Kingman, S. W.; Miles, N. J.,
Resources Conservation and Recycling **2002**, 34, (2), 75-90.
55. Thostenson, E. T.; Chou, T. W., *Composites Part a-Applied Science and
Manufacturing* **1999**, 30, (9), 1055-1071.
56. Hayes, B. L., *Microwave Synthesis - Chemistry at the Speed of Light*. CEM
Publishing: Matthews, 2002.

Chapter 2. The Colloidal Nanoparticle Reaction System

2.1 The Reaction System

The synthesis of nanocrystals from reactive intermediates is often described in terms of a crystallization process, where the rate of formation is counterbalanced by dissolution via an Ostwald ripening mechanism¹⁻⁴. In recent studies, the rate of formation has been nicely correlated to the thermodynamics of the reactants and forming nanocrystal surface governed by the energetics of the passivant with the nanocrystal surface and the reactive precursors⁵⁻⁸.

In general, colloidal nanocrystals can be synthesized by heating a bulk reaction solution containing the necessary reactants in the presence of a strong Lewis base to control the kinetics of growth^{5,6} (Figure 2.1) The nature of heating the material can have a substantial impact on the pathway of a reaction. Microwave heating drives a reaction by heating the reactant through a dielectric coupling⁹⁻¹². This process is described in chapter 4 of this thesis. The general scheme applied in this thesis is the use of microwaves to heat the reactants and drive the nanocrystal reaction. In the microwave driven synthesis of nanocrystals described herein, the solvents and reactants are co-mixed into the reaction vessel at or near room temperature. The growth solvent can be either a pure solvent (passivating or non-passivating) or a mixture of coordinating and non-coordinating solvents. The choice on coordinating versus a coordinating/noncoordinating mixture depends in part on the passivating ligand choice. Acids are used in stoichiometric amounts to the cations

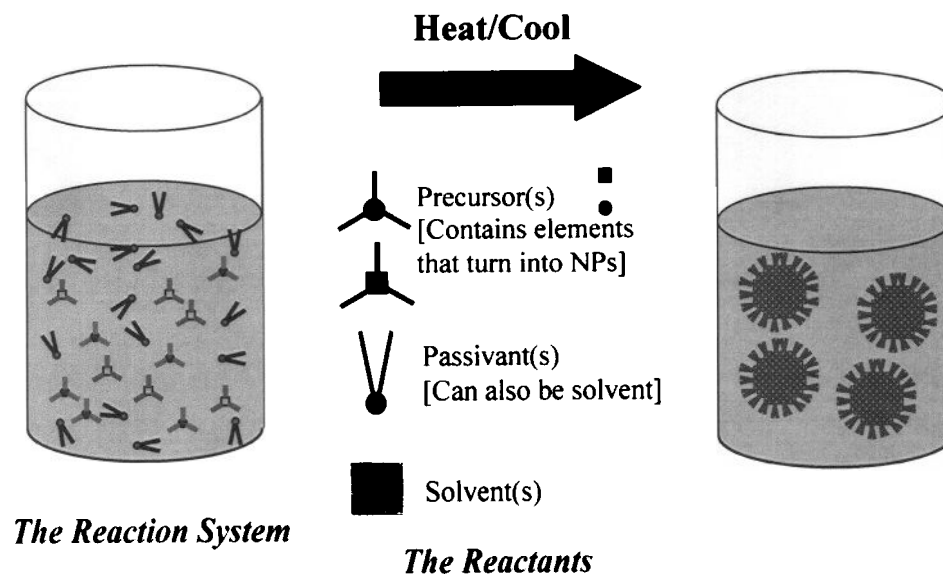


Figure 2.1. Depiction of a typical microwave reaction containing solvent, reactants and growth ligands. In some cases the passivant is the solvent. The reactants are mixed at or near room temperature and heated by microwaves to form the nanocrystalline colloids.

and diluted to a working volume with octadecene. Conversely, basic solvents like amines and phosphine oxides are used as the bulk solvent or a mixture of the two. During the microwave reaction, heating is controlled by microwave power and active cooling to stabilize reaction temperatures¹⁰. The temperature of the reaction is monitored by an IR sensor at the bottom of the reaction vessel, which does not measure reactant temperature, but rather vessel temperature. This can result in measured temperatures that are substantially lower than the actual microscopic reaction temperature. The frequency of the microwave reaction is fixed at 2.45 GHz. Use of focused microwaves is preferred over unfocused, and single-mode is preferred over multimode for efficient heating due to the elimination of hot spots in the reaction vessel which will result in an ensemble of reaction rates over the entire nanocrystal formation.

For self-consistency, in the reactions described in the following chapters, we discuss the main reactant in terms of the element with the largest molar equivalent in the reaction rather than the limiting reagent. In this type of reaction system, if the dielectric constant is over 20 the incident power at time zero of the reaction should be between 50 and 75 W to ensure controlled heating. Incident power over 75 W will lead to rapid temperature spikes within the bulk reaction and will surpass the reaction temperature with significant loss of control. It may also result in loss of stability of the precursors in the system due to the exceedingly high temperature spike. In other words, the heating may proceed out of control.

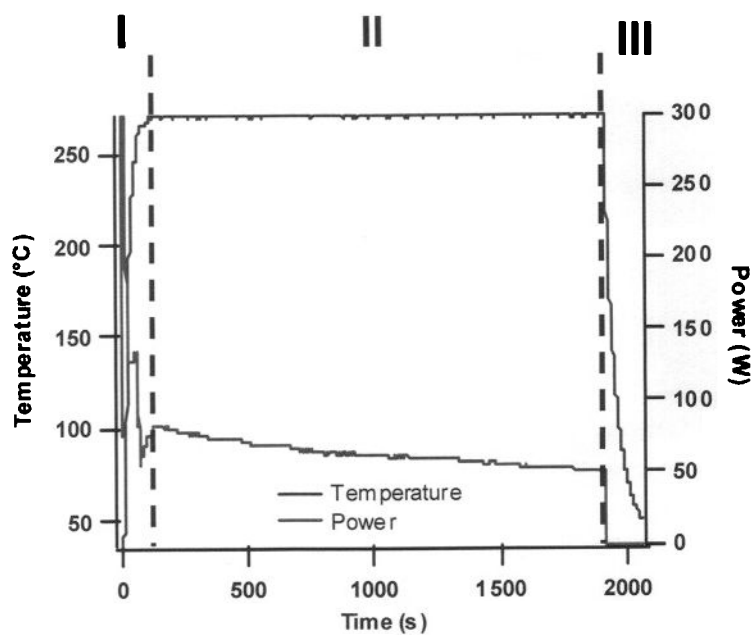


Figure 2.2a. Plot of a typical metal oxide nanoparticle reaction. Region I consists of the ramping and nucleation. Region II is and annealing and size focusing period. Region III is rapid thermal quenching.

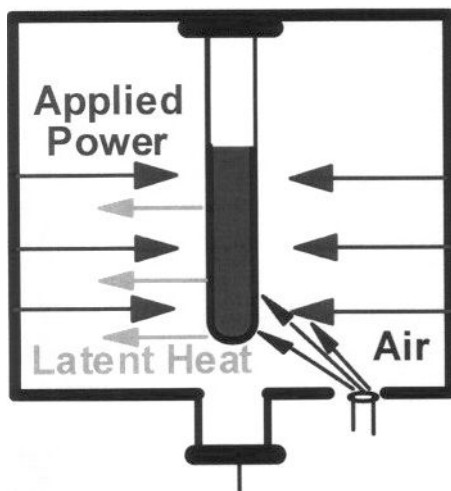


Figure 2.2b. Schematic of the microwave interaction with the reaction vessel in the microwave cavity. The temperature is monitored by an IR sensor below the reaction vessel.

In a nanocrystal growth, we have observed that the material quality is influenced by the initial rate of heating (to ensure uniform nucleation), maintenance of a constant temperature during the growth phase, and rate of cooling following completion of the reaction. A typical reaction trajectory is outlined in figure 2.2a. The average heating rate during the initiation phase of the synthesis can be defined as:

$$\frac{(\text{Temperature at the end of heating (}^{\circ}\text{C)} - \text{Temperature at the beginning of heating (}^{\circ}\text{C)})}{(\text{Duration of heating (min)})}$$

High heating rates are needed to optimize the quality of the nanocrystals that are formed (rate of 30°C/min). When the average heating rate is below 30°C/min, synthesis may result in nanoparticulate materials with unfavorable properties such as higher polydispersities.

Figure 2.2b depicts a typical reaction in a microwave cavity under constant irradiation where the bulk temperature is stabilized by active cooling. The temperature is monitored in real time by an IR sensor below the reaction tube. During the growth stage (II in figure 2.2a) where the temperature is stable at elevated temperature, heating by microwave irradiation is performed together with cooling by using compressed air (figure 2.2b), to balance the input/output of heat to and from the system to hold the temperature constant to within 5°C/min or less.

By balancing the air flow and temperature, one can indirectly elevate the applied power without increasing the reaction temperature of the solution. Increased power correlates to a higher reactant temperature; however it does not translate to an increased solvent temperature (often referred to as the average reaction temperature).

In the third stage of the reaction (2.2 III), the rate of cooling influences the polydispersity due to potential particle growth and dissolution reactions via Ostwald ripening processes. To minimize Ostwald ripening, which tends to dissolve the smaller nanoparticles to the advantage of the larger nanoparticles, the reaction must be rapidly thermally quenched. Upon powering off the microwave the high reactant temperatures are instantly removed, which tends to be an advantage of microwave chemistry. Solvent cooling which can provide energy via thermal transfer is achieved by removing heat from the system by high pressure cooling of the reaction chamber to remove latent heat from the solvent. The average cooling rate of each quenching process is defined as:

$$\frac{(\text{Temperature at the beginning of cooling (}^{\circ}\text{C)} - \text{Temperature at the end of cooling (}^{\circ}\text{C)})}{(\text{Duration of cooling (min)})}$$

A cooling rate of 85°C/min or higher is preferred. When the average cooling rate is below 80°C/min, synthesis may result in nanocrystalline materials with unfavorable properties such as lower dispersibility or wider size distributions.

2.2 Solvent Effect

For typical chemical reactions in solution, the solvent is chosen primarily to maintain solubility and to act as a thermal transfer agent. In a microwave, the solvent choice can impact the nature of the reaction, since in effect the solvent can be transparent to the microwave¹¹ or can absorb the microwave allowing the solvent either to transfer energy conductively to the reactant or act as a thermal bath (heat transfer agent) to maintain reaction temperatures¹³. In addition, the solvent effect can impact the mechanism for nanocrystal formation under microwave heating via acting as a surface passivant to lower the energy of the growing nanomaterial or to influence the reactant activity^{5, 6, 8} (metal-ligand bond strength) which directly influences the thermodynamic and kinetic steps of the reaction¹⁴⁻¹⁶.

Solvent Nanoparticle Interaction. The solvent can be either coordinating or non-coordinating with respect to the precursor molecules, intermediate complexes, or growing nanocrystal formed during nanoparticle formation. Depending on the strength of the passivant to surface, the kinetics of the reaction may be slowed substantially allowing slow nanocrystal growth. Alternatively a strong coordination between the solvent and the precursors will limit the addition of monomers to the growing nanocrystal⁶. Noncoordinating solvents will tend to act primarily as a heat transfer agent on the other hand. Typical non-coordinating solvents used for nanocrystal formation usually consist of long chain, high boiling alkanes and alkenes such as hexadecane, octadecane, eicosane, 1-hexadecene, 1-octadecene and 1-

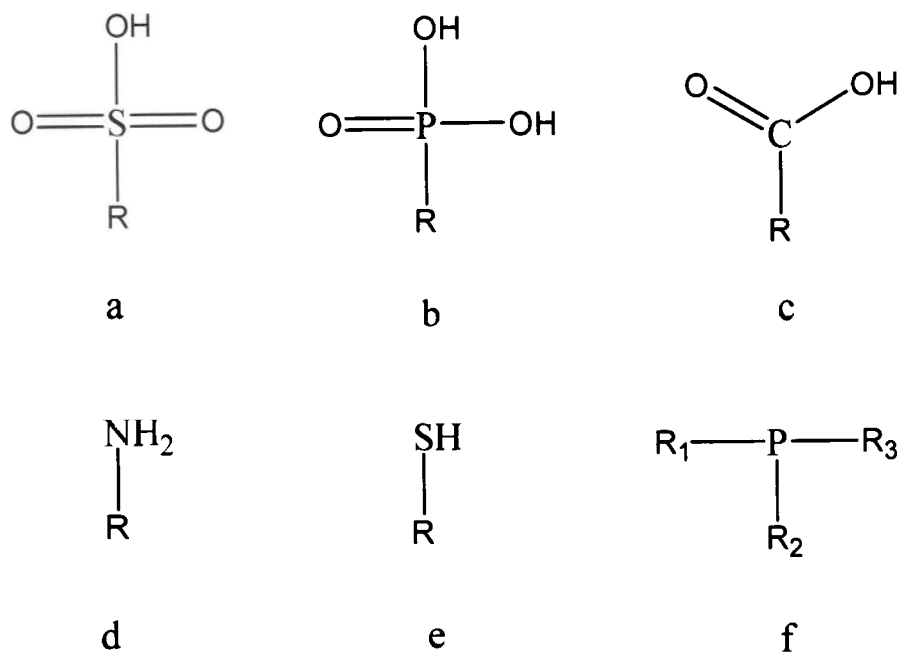


Figure 2.3 Typical functional groups used as the organic passivating layer at the surface of colloidal nanoparticles. The R groups are linear alkanes or alkenes between C₈ and C₁₈ in length: sulfonate (a), phosphate (b), carboxylate (c), amine (d), thiol (e) and phosphine (f).

eicosene. Figure 2.3 shows typical coordinating functionalized alkanes that are either good lewis bases for hard metal ions^{17, 18} (Pearson acid-base description) or can be weak acids for softer metal ions, or pi-backbonding ligands consisting of long alkyl chain organic appendages (backbone of 6 to 20 carbons) to raise the boiling point of the solvent, such as primary alkyl amines, carboxylic acids, sulfonic acids, phosphonic acids, thiols, or phosphines.

Microwave-Solvent Interaction. The ability for a solvent to absorb microwaves is highly dependant on its dipole moment. The reaction temperature of a microwave reaction depends on the absorption cross-section¹², thermal transfer properties of the solvent, and the amount of applied microwave power¹⁹. Clearly reaction temperatures can be lowered by reducing the incident microwave power. This will allow the temperature ramp rate to be tailored to suite a particular nanoparticle formation. Less clearly, the choice of the dipole moment of the solvent will influence the total reaction temperature. A large dipole moment for the solvent will result in strong absorption of the incident microwave power and the reaction will tend to be controlled by the bulk thermodynamic temperature of the solvent. On the other hand a low dipole solvent will tends to be microwave transparent leading to the solvent acting as a thermal moderator of the reaction.

The dipole moment is defined as the product of the distance between two charges and the magnitude of the charge; hence, when a coordinating solvent is used

as the solvent, it has a higher propensity of heating the bulk solution faster than a noncoordinating solvent that has a lower dipole moment by definition.

Solvent	Boiling Point (°C)	Dielectric Constant
Water	100	80.4
Acetone	56	20.7
Hexanes	69	1.9
Octadecene	360	2.2
Hexadecylamine	319	2.1
Tri-n-octylphosphine oxide	385	20

Table 2.1. Comparison of solvent dielectric and boiling point.

Solvent dielectric heating rates for nanoparticle synthesis will depend on several factors: the dielectric constant, the volume of solvent, and its boiling point. For nonpolar solvents such as C₆ - C₂₀ straight chain alkanes, the heating rates are slow for 5 ml of solvent at 300 W of incident power. When comparing the heating rates of trioctylphosphineoxide (760°C/min) to 1-aminohexadecane (30°C/min), trioctylphosphineoxide converts electric energy to heat more efficiently. Comparing these to the heating rate of tetradecene (12°C/min) shows that the choice of solvents

has a substantial influence on the rate at which the heat is transferred to the bulk solution.

Coordinating solvents typically heat faster at lower pressure due to their higher boiling points and functional group-microwave coupling. For example, 5 ml of technical grade hexadecylamine can be heated at 300 W to 280°C in 11 minutes with 1 atm of pressure. In the same manner, trioctylphosphine oxide can be dielectrically heated to 280°C in 15 seconds with 1 atm of pressure. Super-heated octane plateaus at 147°C after 15 minutes of heating at 300 W with 10 atm of pressure. However, in the presence of Cd and Se monomers (57 mM), super-heating octane can reach nanoparticle formation temperatures as high as 250°C in 6 minutes with 15 atm of pressure with 300 W of incident microwave power. The lower boiling point alkanes will have a lower plateau temperature in terms of the maximum sustained temperature at high pressure. The higher boiling alkanes can achieve higher temperatures in a shorter period of time when compared to alkanes. When 5 ml of tetradecene is heated at 300 W, it can reach 250°C in 13 min. The combination of applied power, pressurization of the reaction vessel and microwave cross section of the solvent provides a significant degree of flexibility in the nature of reaction heating and thus reaction thermodynamics.

2.3. Ionic Liquids

Dielectric heating of nonpolar molecules is not only common to inorganic materials synthesis, but it is a common theme in organic synthetic chemistry²⁰⁻²³.

Heating large volumes of benzene, toluene or hexane for industrialization of pharmaceuticals has generated research for heating non-polar matrices. Additives to the reaction solvent can substantially influence the heating rates of the solution. For instance, addition of small amounts of a strong microwave absorber that does not interact with the reactants can have profound effects on the rate of heating²⁴⁻²⁷. The organic synthetic literature has shown that the use of ionic liquids can be used to aid heating of non-polar solvents such as hexanes, toluene and benzene¹¹. The ability of ionic liquids to convert electromagnetic energy to heat has led to growing research on the discovery of new ionic liquids and their structure in solution²⁸⁻³⁴.

Ionic liquids (ILs) translate very well to microwave-assisted formation of nanoparticles. The effect of the ionic liquid to rapidly heat the bulk solution can be traced back to their selective ability to couple with the microwaves and efficiently convert electromagnetic energy into heat. The high dielectric heating ability of ionic liquids at low concentrations compared to the solvent in effect increases the microscopic temperature of the solution. In addition, ILs can be used as unique passivants for nanoparticles³⁵. The effect of the higher heating rate in the presence of the ionic liquids increases the microscopic reaction temperatures at the forming nanoparticles. Whereas microwave power can overcome kinetic barriers, the addition of ionic liquids overcomes thermodynamic barriers in the reaction. It can therefore be imagined that by choosing a cation/anion pair that will not coordinate to the nanoparticles intermediates or the surface of growing nanoparticles, can aid as assisting microscopic heat sources.

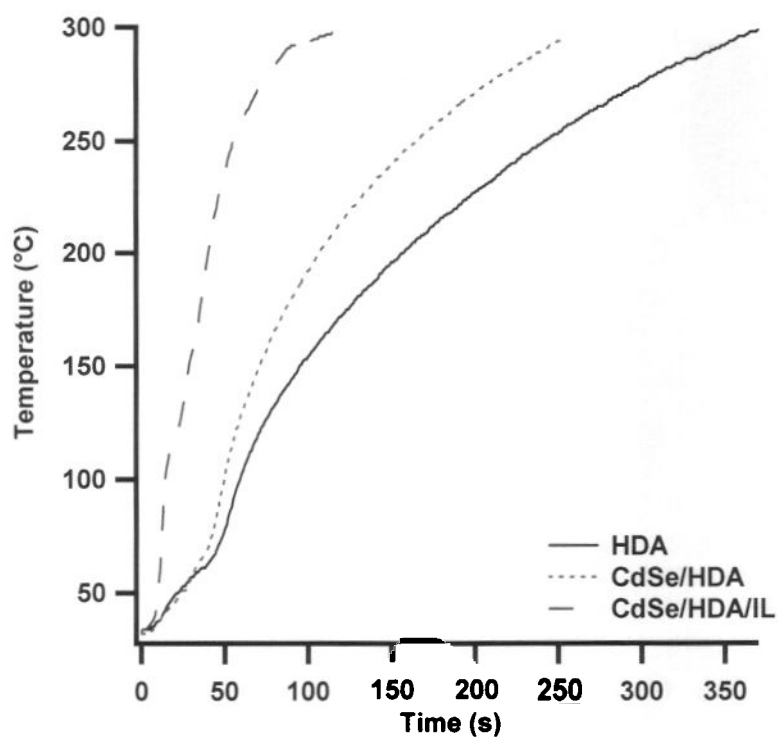


Figure 2.4. Temperature ramping profiles of hexadecylamine, $\text{Li}_4[\text{Cd}_{10}\text{Se}_4(\text{SPh})_{16}]$ in hexadecylamine compared with stoichiometric amounts of 1-hexyl-3-methylimidazolium chloride to increase the efficiency of the temperature ramping.

The heating rate for pure alkyl amine solvents like 1-aminooctane, 1-aminododecane, and 1-aminohexadecane are comparable to non-polar alkanes due to the similar dielectric constants. Upon addition of the ionic liquid 1-hexyl-3-methylimidazolium chloride, the heating rate of the solution increases dramatically as seen in figure 2.4 due to the large microwave cross section for ionic liquids.

The effect of the ionic liquid to rapidly heat the bulk solution can be traced back to their selective ability to couple with the microwaves and efficiently convert electromagnetic energy into heat. The effect of the higher heating rate in the presence of the ionic liquids will increase the microscopic reaction temperatures at the forming nanoparticles is critical for overcoming activation barriers during the growth phase for the II-VI materials.

The choice of the IL is dependent on the desire to apply microscopic reaction control at the nanoparticle surface (passivation) or at the constituent and/or growing nanoparticle reactivity's (microscopic heating). In general, ionic liquids composed of the cation families: imidazolium, phosphonium, pyridinium, ammonium, among the most common summarized in table 2.2, and their family of substituted species are utilized to control the reactions. Lewis acidity and basicity which are involved in constituent reactivity and surface passivation of a growing nanoparticle is tunable by counterion selection. A strong Lewis base increases passivant-like behavior, while a sterically hindered, i.e., tetra-alkyl ammonium salt, increases microscopic temperatures. The choice of the counterion can be as simple as a halide or slightly more sophisticated like long chain derivatized sulfates or phosphates.

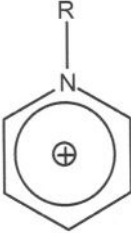
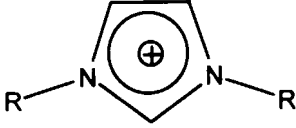
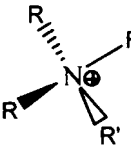
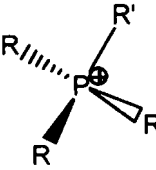
Cation	Structure	Anion
N-Alkylpyridinium		PF_6^- BF_4^- NO_3^- Cl^- $[\text{CF}_3\text{SO}_3]^-$ $[\text{N}(\text{CF}_3\text{SO}_2)_2]^-$
1-Alkyl-3-alkylimidazolium		
Tetraalkylammonium		
Tetraalkylphosphonium		

Table 2.2 Common alkyl cations and anions used in ionic liquids

2.4 References

1. Uskokovic, V.; Drofenik, M., *Surface Review and Letters* **2005**, 12, (2), 239-277.
2. Huber, D. L., *Small* **2005**, 1, (5), 482-501.

3. Li, H. P.; Han, B. X.; Liu, J.; Gao, L.; Hou, Z. S.; Jiang, T.; Liu, Z. M.; Zhang, X. G.; He, J., *Chemistry-a European Journal* **2002**, 8, (24), 5593-5600.
4. Murray, C. B.; Kagan, C. R.; Bawendi, M. G., *Annual Review of Materials Science* **2000**, 30, 545-610.
5. Peng, X. G.; Manna, L.; Yang, W. D.; Wickham, J.; Scher, E.; Kadavanich, A.; Alivisatos, A. P., *Nature* **2000**, 404, (6773), 59-61.
6. Peng, X. G.; Wickham, J.; Alivisatos, A. P., *Journal of the American Chemical Society* **1998**, 120, (21), 5343-5344.
7. Qu, *Journal of the American Chemical Society* **2001**, 124, (9), 2049-2055.
8. Peng, Z. A.; Peng, X. G., *Journal of the American Chemical Society* **2001**, 123, (1), 183-184.
9. Gabriel, C.; Gabriel, S.; Grant, E. H.; Halstead, B. S. J.; Mingos, D. M. P., *Chemical Society Reviews* **1998**, 27, (3), 213-223.
10. Hayes, B. L., *Microwave Synthesis - Chemistry at the Speed of Light*. CEM Publishing: Matthews, 2002.
11. Leadbeater, N. E.; Torenius, H. M., *Journal of Organic Chemistry* **2002**, 67, (9), 3145-3148.
12. Loupy, A., *Microwaves in organic synthesis*. Wiley-VCH: Weinheim ; Cambridge, 2002; p xxiv, 499.
13. Mingos, D. M. P.; Baghurst, D. R., *Chemical Society Reviews* **1991**, 20, (1), 1-47.

14. Talapin, D. V.; Rogach, A. L.; Shevchenko, E. V.; Kornowski, A.; Haase, M.; Weller, H., *Journal of the American Chemical Society* **2002**, 124, (20), 5782-5790.
15. Talapin, D. V.; Gaponik, N.; Borchert, H.; Rogach, A. L.; Haase, M.; Weller, H., *Journal of Physical Chemistry B* **2002**, 106, (49), 12659-12663.
16. Talapin, D. V.; Haubold, S.; Rogach, A. L.; Kornowski, A.; Haase, M.; Weller, H., *Journal of Physical Chemistry B* **2001**, 105, (12), 2260-2263.
17. Pearson, R. G., *Science* **1966**, 151, (3707), 172-&.
18. Pearson, R. G., *Journal of the American Chemical Society* **1963**, 85, (22), 3533.
19. Thostenson, E. T.; Chou, T. W., *Composites Part a-Applied Science and Manufacturing* **1999**, 30, (9), 1055-1071.
20. Lidstrom, P.; Tierney, J.; Wathey, B.; Westman, J., *Tetrahedron* **2001**, 57, (45), 9225-9283.
21. Elander, N.; Jones, J. R.; Lu, S. Y.; Stone-Elander, S., *Chemical Society Reviews* **2000**, 29, (4), 239-249.
22. Loupy, A.; Petit, A.; Hamelin, J.; Texier-Boullet, F.; Jacquault, P.; Mathe, D., *Synthesis-Stuttgart* **1998**, (9), 1213-1234.
23. Huynh, W. U.; Dittmer, J. J.; Libby, W. C.; Whiting, G. L.; Alivisatos, A. P., *Advanced Functional Materials* **2003**, 13, (1), 73-79.
24. Law, M. C.; Wong, K. Y.; Chan, T. H., *Green Chemistry* **2002**, 4, (4), 328-330.
25. Khadilkar, B. M.; Rebeiro, G. L., *Organic Process Research & Development* **2002**, 6, (6), 826-828.

26. Asaki, M. L. T.; Redondo, A.; Zawodzinski, T. A.; Taylor, A. J., *Journal of Chemical Physics* **2002**, 116, (19), 8469-8482.
27. Fraga-Dubreuil, J.; Bazureau, J. P., *Tetrahedron Letters* **2001**, 42, (35), 6097-6100.
28. Zhao, H.; Xia, S. Q.; Ma, P. S., *Journal of Chemical Technology and Biotechnology* **2005**, 80, (10), 1089-1096.
29. Hardacre, C., *Annual Review of Materials Research* **2005**, 35, 29-49.
30. Crowhurst, L.; Lancaster, N. L.; Perez-Arlandis, J. M.; Welton, T.,
Understanding reactions in ionic liquids. In *Ionic Liquids Iiib: Fundamentals, Progress, Challenges and Opportunities: Transformations and Processes*, 2005;
Vol. 902, pp 218-232.
31. Binnemans, K., *Chemical Reviews* **2005**, 105, (11), 4148-4204.
32. MacFarlane, D. R.; Forsyth, S. A., Acids and bases in ionic liquids. In *Ionic Liquids as Green Solvents: Progress and Prospects*, 2003; Vol. 856, pp 264-276.
33. Lagunas, M. C.; Pitner, W. R.; van den Berg, J. A.; Seddon, K. R., Solvent-solute interactions in ionic liquid media: Electrochemical studies of the ferricenium-ferrocene couple. In *Ionic Liquids as Green Solvents: Progress and Prospects*, 2003; Vol. 856, pp 421-438.
34. Martin, J. D., Structure-property relationships in ionic liquids. In *Ionic Liquids*, 2002; Vol. 818, pp 413-427.
35. Antonietti, M.; Kuang, D. B.; Smarsly, B.; Yong, Z., *Angewandte Chemie-International Edition* **2004**, 43, (38), 4988-4992.

Chapter 3. Parallel Synthetic Methods for Colloidal Nanoparticles

3.1 Introduction

In this chapter, a general approach to the formation of high quality CdSe and InGaP colloidal semiconductor quantum dots is explained. CdSe was chosen as a model material to study the growth characteristics and to develop a general method of parallel nanoparticle formation.

The principal of parallel synthesis expands the sampling space of nanoparticle growth characteristics under different reactant concentrations, coordinating/noncoordinating solvent ratios and dopant ion concentrations. Typically, a single reaction is studied for the development of a new material or to study the reaction mechanisms for a certain compound. This approach is cumbersome and is prone to random error such as temperature ramp rates, reactant stoichiometries and cross contamination from reaction to reaction.

Parallel synthesis is a concept that enables multiple reactions to be carried out under identical temperature ramping, reaction times and stirring conditions minimizing random error. Parallel synthesis is most commonly used in organic and polymer chemistry¹⁻⁴, testing catalysts⁵⁻⁷ and constructing combinatorial libraries⁸⁻¹¹.

This is the first report of such a concept applied to solution phase nanoparticle synthesis. It is a common misconception that nanoparticle growth must occur under continuous inert gas purging over the course of the reaction. In the parallel method, growth is carried out in sealed reaction vials. Parallel synthesis opens an additional

dimension to the sampling space of a typical synthesis. Under these conditions, for example, time, reactant concentration and reactant stoichiometry can be studied in a single synthesis for an array of samples.

Due in part to the reaction conditions of highly luminescent colloidal nanoparticles explained in chapter 1 of this thesis, no commercial parallel synthesis apparatus is available. A simple apparatus was constructed from stock aluminum to sit atop a standard stirring hot plate to contain commercially available vials (figure 3.1a and b). A 9" by 9" block of stock 2" thick aluminum was milled to fit a standard hot plate (Fisher Scientific). Nine wells were bored in a square pattern at 1" deep to accommodate 27 ml headspace vials with crimp top seals (National Scientific). A small well was recessed near the center to accommodate a thermocouple for temperature sensing. Flea stir bars were optimum for stirring in the reactor vials sitting in the aluminum thermal wells. This crude and simple method was the first stage of the microwave development discussed in chapter 4 of this thesis.

Chapter 3. Parallel Synthetic Methods for Colloidal Nanoparticles

3.1 Introduction

In this chapter, a general approach to the formation of high quality CdSe and InGaP colloidal semiconductor quantum dots is explained. CdSe was chosen as a model material to study the growth characteristics and to develop a general method of parallel nanoparticle formation.

The principal of parallel synthesis expands the sampling space of nanoparticle growth characteristics under different reactant concentrations, coordinating/noncoordinating solvent ratios and dopant ion concentrations. Typically, a single reaction is studied for the development of a new material or to study the reaction mechanisms for a certain compound. This approach is cumbersome and is prone to random error such as temperature ramp rates, reactant stoichiometries and cross contamination from reaction to reaction.

Parallel synthesis is a concept that enables multiple reactions to be carried out under identical temperature ramping, reaction times and stirring conditions minimizing random error. Parallel synthesis is most commonly used in organic and polymer chemistry¹⁻⁴, testing catalysts⁵⁻⁷ and constructing combinatorial libraries⁸⁻¹¹.

This is the first report of such a concept applied to solution phase nanoparticle synthesis. It is a common misconception that nanoparticle growth must occur under continuous inert gas purging over the course of the reaction. In the parallel method, growth is carried out in sealed reaction vials. Parallel synthesis opens an additional

dimension to the sampling space of a typical synthesis. Under these conditions, for example, time, reactant concentration and reactant stoichiometry can be studied in a single synthesis for an array of samples.

Due in part to the reaction conditions of highly luminescent colloidal nanoparticles explained in chapter 1 of this thesis, no commercial parallel synthesis apparatus is available. A simple apparatus was constructed from stock aluminum to sit atop a standard stirring hot plate to contain commercially available vials (figure 3.1a and b). A 9" by 9" block of stock 2" thick aluminum was milled to fit a standard hot plate (Fisher Scientific). Nine wells were bored in a square pattern at 1" deep to accommodate 27 ml headspace vials with crimp top seals (National Scientific). A small well was recessed near the center to accommodate a thermocouple for temperature sensing. Flea stir bars were optimum for stirring in the reactor vials sitting in the aluminum thermal wells. This crude and simple method was the first stage of the microwave development discussed in chapter 4 of this thesis.

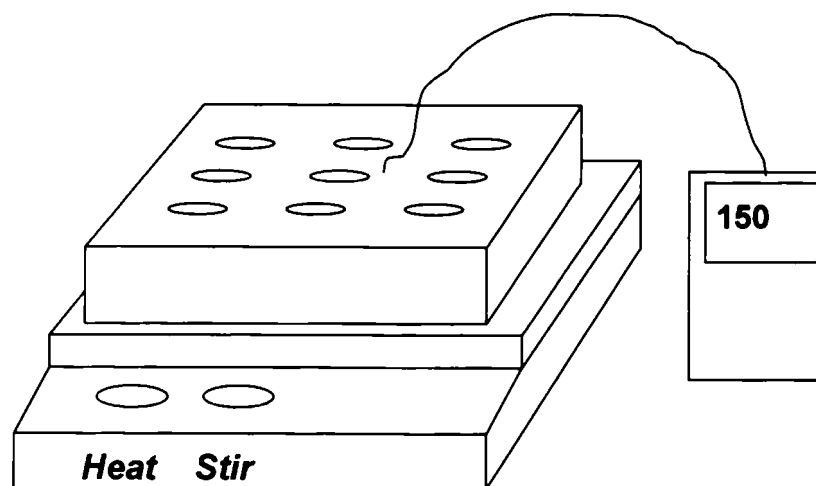


Figure 3.1a. Illustration of the 3 well by 3 well parallel reactor apparatus mounted on a standard stirring hot plate. A temperature sensing thermocouple is situated near the center of the plate for the most accurate measurement.

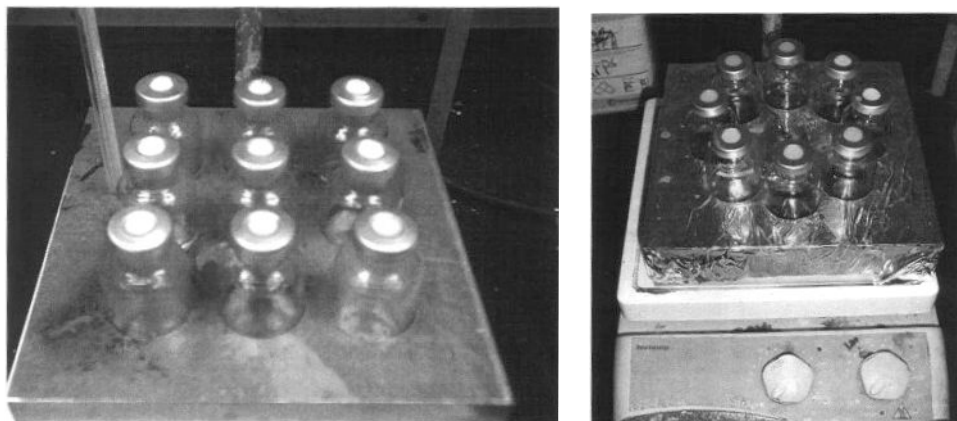


Figure 3.1b. Pictures of two parallel reactor designs with reactions of CdSe (left) and InGaP (right) illustrating different plate configurations.

3.2 Experimental Methods

Preparation of CdSe. The starting material for the formation of the CdSe nanoparticles was based on the single source precursor $\text{Li}_4[\text{Cd}_{10}\text{Se}_4(\text{SPh})_{16}]$ ¹². For a typical synthesis, a stock solution of the precursor was prepared by dissolving 1.62 g of $\text{Li}_4[\text{Cd}_{10}\text{Se}_4(\text{SPh})_{16}]$ in 1,3-Dimethyl-3,4,5,6-tetrahydro-2(1*H*)-pyrimidinone in a argon atmosphere. In a glove box, 13 g of hexadecylamine (HDA), previously fractionally distilled, was massed into nine 27 ml headspace vials (20 mm crimp seals from National Scientific). Aluminum crimp seals fitted with high temperature septa were placed on the vials before they were removed from the glove box.

The vials were placed in the room temperature thermal wells of the parallel reactor. With mild stirring, the vials were slowly heated to melt the HDA. The temperature was monitored by a type J thermocouple. At approximately 80°C after the HDA was melted, 0.5 ml of the CdSe precursor solution was injected to each vial. All nine injections were made less than 10 seconds apart to minimize the nucleation time difference. Upon injection, the solution turned from clear colorless to clear yellow indicating the nucleation of the CdSe nanoparticles.

Using the rheostat on the hot plate the temperature was slowly ramped over the course of nine hours. The temperature was monitored in real time by the thermocouple. Vials were removed at different time intervals and temperatures: vial 1 170°C, 0.2 hr; vial 2 187°C, 2.0 hr; vial 3 196°C, 4.1 hr; vial 4 203°C, 5.5 hr; vial 5 210°C, 6.4 hr; vial 6 215°C, 7.5 hr ; vial 7 222°C, 8.4 hr; vial 8 225°C, 9.5 hr; vial 9 230°C, 10.5 hr .

Preparation of CdSe/TOPSe. The preparation follows the protocol that was previously described above. TOPSe was prepared by making a 1.5M solution of Se in trioctylphosphine. TOPSe was injected into the reaction at 100°C. The stoichiometry of TOPSe was based on Cd from the precursor cluster. The mole ratio of TOPSe:Cd for a series of 8 parallel reactions was 0.00, 0.62, 1.36, 2.07, 3.02, 4.53, 6.40, and 9.01. The reactor plate temperature was then increased to 195°C and held constant for 2 hours and cooled to room temperature inside the reactor plate.

Preparation of InGaP. The preparation of InGaP is based on a modification of literature methods¹³. The In and Ga intermediates were prepared by mixing 2.71 mmol indium (III) acetate and 0.271 mmol of gallium (III) 2,4-pentanedionate and 8.94 mmol hexadecanoic acid with 190 ml of octadecene (ODE) in a three neck flask. The cation intermediates were formed by heating the solution to 110°C under vacuum for two hours with four cycles of Ar backfilling. The temperature of the solution was allowed to cool to 50°C. The In/Ga precursor solution was kept under Ar at 50°C as a stock solution for later use. 10 ml portions of the cation stock solution were injected into pre heated headspace vials. Under vigorous stirring, the temperature of the parallel block was raised to 295°C. At this time, TMSP was swiftly injected into each vial from a 96.0mM TMSP stock solution in ODE.

3.3 Results and Discussion

3.3.1 Parallel Synthesis of CdSe Nanoparticles from $\text{Li}_4[\text{Cd}_{10}\text{Se}_4(\text{SPh})_{16}]$

For proof of concept of the parallel reactor, two reactions were performed; a control in which all reaction positions were verified to yield identical results and a time dependant reaction in which vials were sequentially removed. The optical absorbance and photoluminescence of the control reactions were compared in figure 3.2a. The absorbance profiles are identical in shape and wavelength position for three individual reactions. The PL occupies the same shape, bandwidth and QY within experimental error. It is clear that individual reactor wells can yield identical heating and stirring profiles for an array of individual reactions.

One advantage the parallel method has is the flexibility to study time dependant growth for a series of identical reactions. For the time dependant reaction, the temperature was quickly raised from 80°C to 210°C. Time zero began once the reaction temperature was reached. Vials were removed as a function of reaction time. Figure 3.2b shows the absorbance profile of the nine reactions as they were thermally quenched. The particles follow the same time dependant growth as the previous report¹².

From figure 3.2b it is observed that multiple sizes can be isolated from one parallel reaction sequence. These reactions follow the typical time dependant growth. A 6.2 nm particle can be isolated in 10.5 hours while a 1.5 nm particle is isolable in 2 hours under slow temperature ramping conditions.

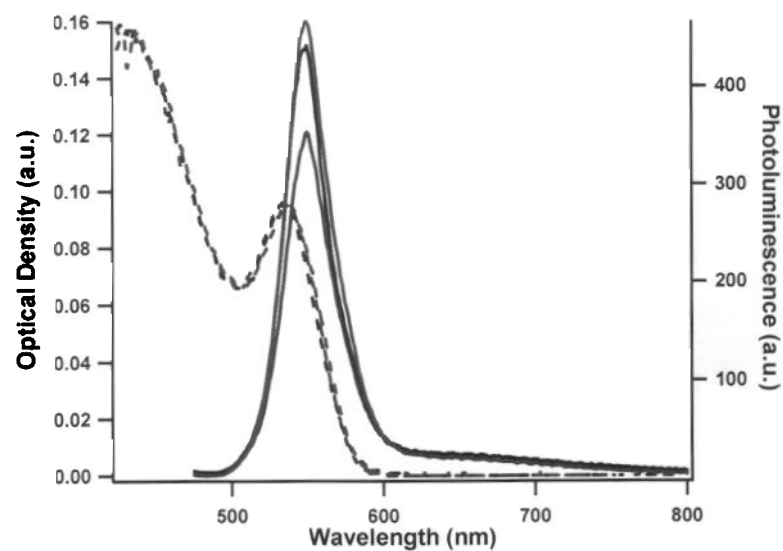


Figure 3.2a. Parallel control reactions performed under the same reactant concentration, temperature and time

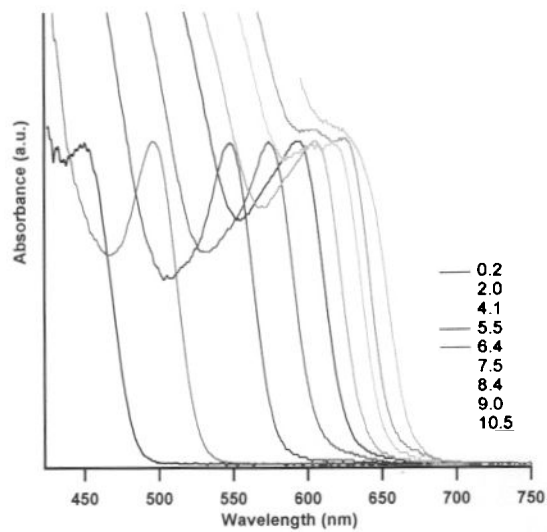


Figure 3.2b. Room temperature absorbance profiles of the nine reactions as they were thermally quenched once removed from the parallel reactor. The legend indicates the reaction time for each sample.

Another advantage the parallel approach has is the study of additives on the formation characteristics of colloidal nanoparticles. The precursor $\text{Li}_4[\text{Cd}_{10}\text{Se}_4(\text{SPh})_{16}]$ cluster has 2.5 mol Cd for every mol Se. To investigate the formation rate of CdSe nanoparticles stoichiometric amounts of TOPSe was added such that the Se:Cd mol ratio was as follows: 0.00, 0.62, 1.36, 2.07, 3.02, 4.53, 6.40, and 9.01.

Figure 3.3 shows the absorbance and photoluminescence profiles of each reaction. For the reactions that consisted of 0.00 to 6.40 Se:Cd ratio, a slight red shift is observed in the absorbance. The corresponding PL shows minimal defect emission and an asymmetric blue tail. This is indicative of a broad sized distribution of smaller particles. The reaction with the highest ratio of Se shows two distinct features; a faster formation rate of larger particles and a broader size distribution consisting of two distinct sizes. The blue edge of the PL in trace f reveals a distinct population of approximately 4 nm within the ensemble of the 5.5 nm.

One explanation may be that a rapid nucleation and growth occurs upon the addition of the TOPSe. Increasing the Se concentration has a significant effect on the formation rate of larger particles and temperatures below 200 °C.

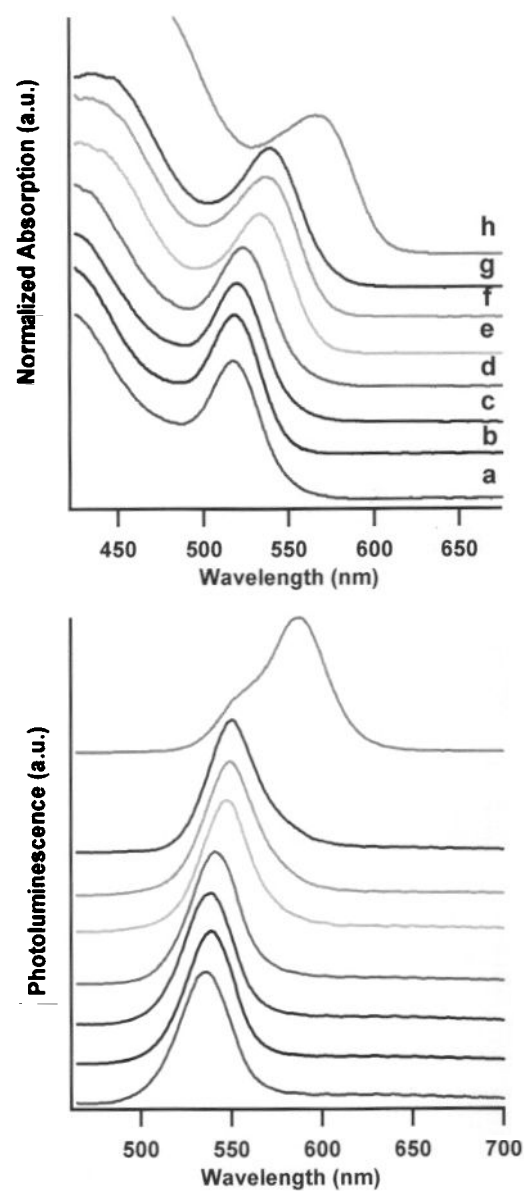


Figure 3.3. Absorbance spectrum (top) and photoluminescence (bottom) of CdSe growth influenced by TOPSe. TOPSe : Cd mole ratio for each reaction: 0.00 (a), 0.62 (b), 1.36 (c), 2.074 (d), 3.02 (e), 4.53 (f), 6.40 (g), 9.01 (h).

3.3.2 Parallel Synthesis of InGaP Nanoparticles

Nanoparticle formation in coordinating/noncoordinating solvent mixtures has an additional component necessary for optimum growth over colloidal formation in purely coordinating solvents. The coordinating/noncoordinating growth requires optimum total ion concentration as well as cation:anion mol ratio and cation:ligand mole ratio.

To optimize the cation:anion concentration for the thermal preparation of InGaP, a series of separate reactions were prepared with equal cation:ligand ratios. The cation solutions were heated in a parallel block to 280°C. Various amounts of TMSP were injected into each vial and the reactions were left to anneal at 280°C for 2.5 hours.

The reactions performed with In:P ratios of 3.9 to 2.7, the size distribution is broad observed by the poorly resolved exciton in figure 3.4. When the In:P ratio approaches 2.1 the size distribution is maximized observed by the exciton and the corresponding PL bandwidth narrowing. The In:P ratio proceeded beyond 2.1 evidence of broadening is seen in the absorbance spectrum indicating the size distribution begins to increase. By this method, optimization of the cation:anion mole ratio was conducted. It is clear that these types of parallel reaction are very versatile and efficient towards nanomaterial synthesis optimization.

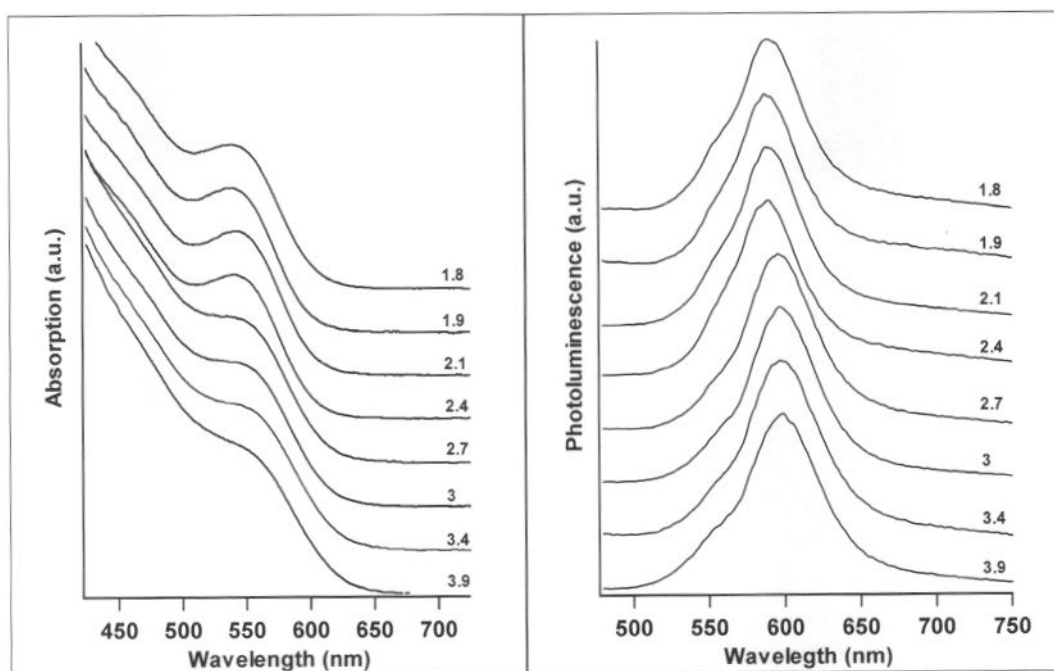


Figure 3.4. Room temperature absorbance (left) and photoluminescence (right) of InGaP prepared by the parallel method with increasing cation:anion mole ratio.

3.4 Conclusion

The parallel method offers greater dimensional investigation of reaction trajectories for colloidal nanoparticles. For both II-VI and III-V colloidal nanoparticles, optimum reaction conditions can quickly be elucidated. Additive influence like TOPSe in CdSe growth can efficiently and reproducibly be investigated. Moreover, difficult synthesis such as the phosphides nanoparticle systems can be rapidly optimized. The basic premise of the sealed vial parallel method preceded the microwave development, but was instrumental in establishing a foundation of reproducible synthesis under sealed headspace conditions.

3.5 References

1. Shuttleworth, S. J.; Allin, S. M.; Wilson, R. D.; Nasturica, D., *Synthesis-Stuttgart* **2000**, (8), 1035-1074.
2. Dolle, R. E., *Journal of Combinatorial Chemistry* **2000**, 2, (5), 383-433.
3. An, H. Y.; Cook, P. D., *Chemical Reviews* **2000**, 100, (9), 3311-3340.
4. Parlow, J. J.; Devraj, R. V.; South, M. S., *Current Opinion in Chemical Biology* **1999**, 3, (3), 320-336.
5. Klanner, C.; Farrusseng, D.; Baumes, L.; Mirodatos, C.; Schuth, F., *Qsar & Combinatorial Science* **2003**, 22, (7), 729-736.
6. Hagemeyer, A.; Jandeleit, B.; Liu, Y. M.; Poojary, D. M.; Turner, H. W.; Volpe, A. F.; Weinberg, W. H., *Applied Catalysis a-General* **2001**, 221, (1-2), 23-43.
7. Dahmen, S.; Brase, S., *Synthesis-Stuttgart* **2001**, (10), 1431-1449.

8. Ley, S. V.; Baxendale, I. R., *Nature Reviews Drug Discovery* **2002**, 1, (8), 573-586.
9. Boyle, N. A.; Janda, K. D., *Current Opinion in Chemical Biology* **2002**, 6, (3), 339-346.
10. Abel, U.; Koch, C.; Speitling, M.; Hansske, F. G., *Current Opinion in Chemical Biology* **2002**, 6, (4), 453-458.
11. Ripka, W. C.; Barker, G.; Krakover, J., *Drug Discovery Today* **2001**, 6, (9), 471-477.
12. Cumberland, S. L.; Hanif, K. M.; Javier, A.; Khitrov, G. A.; Strouse, G. F.; Woessner, S. M.; Yun, C. S., *Chemistry of Materials* **2002**, 14, (4), 1576-1584.
13. Battaglia, D.; Peng, X. G., *Nano Letters* **2002**, 2, (9), 1027-1030.

Chapter 4. Microwave Enhanced Reaction Rates for Nanoparticle Synthesis

4.1 Introduction

Microwave heating methods can address the problem of heating inhomogeneity, while providing a scalable platform for industrial applications. In fact, microwave heating has been demonstrated to enhance reaction rates, selectivity and product yields in organic chemistry¹. By judicious choice of the solvents, passivating ligands and reactants, the nanomaterial precursors can be selectively heated over the solvent or passivating ligand. Selective heating in the microwave cavity²⁻⁴ is advantageous in organic synthesis and in general these microwave synthetic methodologies are quite adaptable to reactions that have high energies of activation and slow reaction rates⁵⁻⁸. This effect alone has advantages to colloidal nanostructured materials synthesis.

The development of microwave synthetic methodology and the influence of additives for a range of organically passivated binary and ternary III-V (InGaP, InP) and II-VI (CdSe) materials is described. The nanomaterials are reproducibly prepared in less than 20 min in a focused 2.45 GHz, single mode high power microwave (300-400W/cm²) capable of operating at 300°C for extended reaction times. The as prepared materials are crystalline with a size distribution of 5-6% and spherical in shape. Exploration of the power, temperature, time, and additive dependent growth is investigated. Microwave chemistry appears to enhance reaction rates either by overcoming local intermediates which act as traps along the reaction trajectory or by

increasing the microscopic reaction temperature of the reaction. The difference in the effect of additives and the microwave variables (temperature, time, and power) for the II-VI and III-V materials suggest that local intermediates and transition states in the reaction trajectory are substantially different. The III-V materials show no time, temperature, or power dependent growth in the microwave; however when the typical high boiling non-coordinating solvent, ODE is replaced with a low boiling solvent, decane, the colloidal size distribution is significantly narrowed and the quantum efficiencies are increased (PLQY = 15%) presumably due to increase reaction pressures that may anneal out vacancy or defects in the forming nanocrystals. CdSe growth and properties are dependent on the addition of ionic liquids, as well as reaction temperature in concert with the applied microwave power and reaction time.

4.2 Experimental Methods

The reactants were purchased from Aldrich Chemical and used without further purification. Decane was purified previously by distillation over activated 4 Å molecular sieves. Isolation of all nanomaterials is achieved under an Ar atmosphere by dissolution of the room temperature reaction mixture in a minimum of toluene, addition of a 2:1 anhydrous butanol / methanol solution to induce particle precipitation, and collection of the solid via centrifugation. The process is repeated 3 times to remove unwanted reactants. All glassware was dried prior to use.

Microwave nanoparticle synthesis⁹ was carried out in a modified CEM Discover microwave using single mode and continuous power 2.45 GHz. Although the reactions can be carried out in any microwave, reaction temperature, microwave

power, and mode quality is critical in producing the highest structural, size dispersity, and optical quality. The CEM microwave cavity was commercially modified by CEM with a Teflon insert to allow sustainable heating at 300°C at powers up to 400W. Each example reaction was carried out in a sealed reaction vessel with 5ml of the respective starting solution. To maintain stable power and temperature during the reaction, the microwave cavity was actively cooled by compressed air to remove latent heat from the reaction. Active cooling via compressed air allows higher powers to be applied without increasing the reaction temperature. It should be noted that the use of compressed air results in thermal gradients from the reaction vessel inwards towards the reaction center. Reaction temperatures are measured at the vessel wall in the microwave, which will mean that the actual microscopic reaction temperature is not measured; rather the average vessel temperature is reported.

Initiation of the reaction is carried out a maximum power to achieve a desired reaction temperature as rapidly as possible. During the growth phase for nanocrystal chemistry the power and reaction temperature were varied to maximize the quality of the individual materials as measured by TEM, powder X-ray diffraction, and optical absorption and fluorescence. The results of the growth phase studies suggest the temperature and power parameters are unique to the material type, but dictate material quality in the microwave reactions for all nanomaterials studied.

Preparation of CdSe by $\text{Li}_4[\text{Cd}_{10}\text{Se}_4(\text{SPh})_{16}]$. The CdSe was prepared using the single source precursor $\text{Li}_4[\text{Cd}_{10}\text{Se}_4(\text{SPh})_{16}]^{10}$. The additive study with added ionic liquid was carried out using a stock solution of the precursor cluster prepared by

adding 635 mg of $\text{Li}_4[\text{Cd}_{10}\text{Se}_4(\text{SPh})_{16}]$ and 0.0448g of 1-hexyl-3-methylimidazolium chloride to 45g of degassed 1-aminohexadecane at 90°C. The solution was degassed under Ar, and 5 ml aliquots were injected into the microwave reaction vials prior to the reaction. Sample quality for all reactions was monitored by absorption spectroscopy, photoluminescence (PL), and pXRD.

Preparation of CdSe by CdO. In order to investigate other reactions and the effect of a strong microwave absorber (tri-octyl phosphine oxide, TOPO), the microwave studies were carried out using CdO and TBPSe as precursors by the method of Peng, et al¹¹. The Cd and Se precursors were prepared according to literature methods in a mixture of 50:50 (w:w) HDA and TOPO as the solvent¹¹. The Se precursor was injected into the Cd solution at 50°C and mixed for 15 minutes. The solution was maintained at 50 °C to allow the reactants to remain in the liquid state for transfer into the microwave reaction vials. The ramping power was set to 300W until the desired reaction temperature was reached. At this time active cooling was employed to maintain a high power density at 280W for the duration of the reaction. Each reaction time consisted of a duration of 30 seconds. The ramping period ranged from 30 seconds to 1 minute depending on the reaction temperature. Sample quality for all reactions was monitored by absorption spectroscopy, photoluminescence (PL), and pXRD.

Preparation of InGaP in Octadecene. The preparation of InGaP is based on a modification of literature methods^{9, 12}. The In and Ga intermediates were prepared by mixing 2.71 mmol indium (III) acetate and 0.271 mmol of gallium (III) 2,4-

pentanedionate and 8.94 mmol hexadecanoic acid with 190 ml of octadecene (ODE) in a three neck flask. The cation intermediates were formed by heating the solution to 110°C under vacuum for two hours with four cycles of Ar backfilling. The temperature of the solution was allowed to cool to 50°C at which time 1.50 mmol of tris(trimethylsilyl)phosphine was injected TMSPh. The In/Ga/P precursor solution immediately turned from colorless to yellow. The In/Ga/P precursor solution was kept under Ar at 50°C as a stock solution for later use. For a typical reaction, 5 ml of the stock solution was removed by Teflon syringe and placed in a reaction tube (CEM Corporation). The ramp period was set to 300W to achieve the reaction temperature in the least amount of time. Once the desired reaction temperature was reached, the active cooling was employed by stabilizing the power at 280W by applying compressed air (~ 3 – 7psi) to the reaction vessel. Once the reaction was complete the power was reduced to 0 W and the compressed air flow was increased to 70 psi for maximum cooling. Sample quality for all reactions was monitored by absorption spectroscopy, photoluminescence (PL), and pXRD). In addition, TEM was measured on the InGaP samples to measure their shape and crystallinity

Preparation of InGaP in Decane. The reaction stoichiometry and method in decane is identical to the reaction in ODE. The preparation of the cations consisted of placing 710 μmol indium (III) acetate and 74.1 μmol of gallium (III) 2,4-pentanedionate and 2.36 mmol hexadecanoic acid in a three neck flask. The cations (In/Ga) were prepared in the absence of the non-coordinating solvent due to its low boiling point (174°C.). This was achieved by heating the salts to 150°C under

reduced pressure. The melt was clear and colorless and was backfilled with Ar four times at this temperature. The reactants were allowed to cool to room temperature at which time 50.0 ml of decane was injected into flask under inert conditions. The temperature was raised to 50°C to afford a clear and colorless solution at which time 393 μmol of tris(trimethylsilyl)phosphine was injected. The solution slowly turned pale yellow over a 30 minute time period. 5ml of the stock solution was placed in microwave reaction tubes and immediately placed in the microwave chamber for various reaction times (from 30 s to 7 minutes) at 280°C with a stable power at 280W by active cooling. The ramping and cooling parameters were identical to the InGaP prepared in octadecene. Sample quality for all reactions was monitored by absorption spectroscopy, photoluminescence (PL), and pXRD.

Preparation of InP in Octadecene. The InP nanomaterials is prepared in the same manner as InGaP prepared in octadecene, keeping the cation:anion mol ratio 2:1 and the cation:ligand mol ratio at 1:3, and maintained at 50°C under Ar. 78.5 μmol of 1-hexyl-3-methylimidazolium chloride, trihexyltetradecylphosphonium decanoate and trihexyltetradecylphosphonium bromide were massed into separate microwave reaction vials inside of an Ar filled dry box and sealed to later be taken into the fume hood. 5ml of the InP stock solution was injected into the microwave reaction tubes prior to each reaction. Sample quality for all reactions was monitored by absorption spectroscopy, photoluminescence (PL), and pXRD.

4.3 Results and Discussion

Microwave chemistry has become a widely used synthetic methodology in organic chemistry that takes advantage of the selective nature of microwave heating for materials that have high dielectric losses, namely polar systems⁴. Dielectric heating in contrast to convective heating, heats the total volume of the reactants by transferring energy selectively to microwave absorbing materials. The larger the microwave cross-section for a particular constituent, the more dramatic the heating process is. It can therefore be imagined that the intrinsic temperature localized around the ions is significantly higher in temperature than that of the bulk solution.

Owing to the fact that precursors and intermediates along a given reaction trajectory can have different dielectric constants, microwaves can be used to overcome high activation energies for product formation by selectively coupling to intermediates in the transition states. In organic chemistry the better understanding of the reaction trajectories leads to the so-called “specific microwave effect” to systematically manipulate the products generated from a given reaction¹³. In organic reactions, the nature of the selective heating of microwave absorbing materials therefore allow both rapid heating rates and high temperatures to be reached which in turn drive chemical reactions. In addition, it is established that volumetric heating with microwaves reduces the overall thermal gradients in the reaction, producing a more uniform product formation. For nanocrystal growth the higher reaction temperatures, greater thermal control, and lower thermal gradients are needed to produce high quality materials^{14, 15}. If the inorganic precursor or the forming

nanoparticle has a higher cross-section for microwave absorption relative to the reaction solvent, higher reaction temperatures will be achieved in comparison to convective heating with the solvent acting as a thermal mediator absorbing energy from the reactants rather than transferring the heat to the reaction. This suggests if the nanoparticle or intermediates are selectively heated relative to the solvent, that the temperature of the reaction in the microwave, measured at the vessel and/or solvent, can be potentially much higher. This provides exquisite control over the reactions by providing temperature, time, microwave power, and absorption cross-section as mediators for materials synthesis.

Figure 4.1 illustrates a typical reaction trajectory for a nanomaterial grown in a non-polar solvent. The microwave reaction can be divided into three reaction stages: temperature ramping or instantaneous heating to initiate nucleation; a growth regime manipulated by reaction time and temperature; and a rapid thermal quenching step to control Ostwald ripening (reaction termination). In the microwave, the nucleation process is achieved by rapidly increasing the temperature from RT to 280°C at full microwave power (300W to 400W). During the growth phase the power is reduced to maintain a controlled growth stage. The temperature of the reaction is held constant by active cooling of the reaction vessel with forced air to allow power and temperature to be controlled independently. The drawback of active cooling is thermal gradients may be higher than measured. Active cooling carries latent heat away from the vessel during the reaction to stabilize the applied power at a

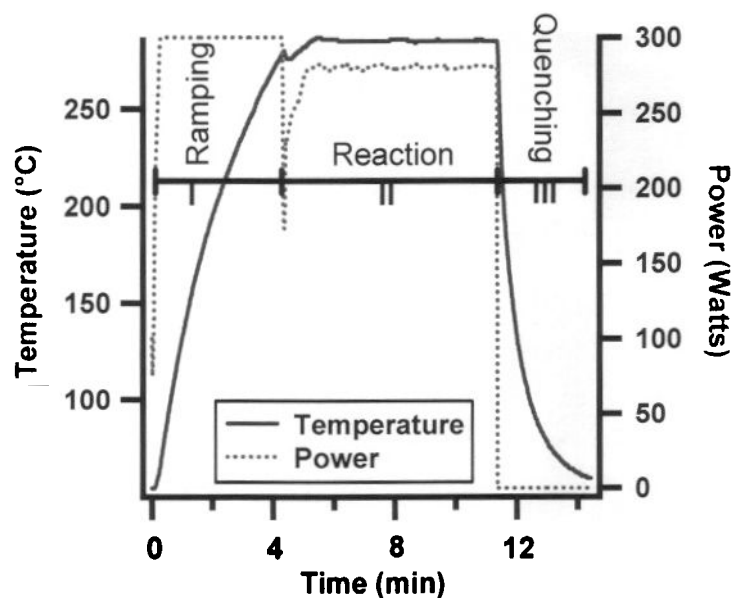


Figure 4.1. Temperature (°C) and power (W) profiles of a typical InGaP reaction. Region (I) shows the temperature ramp carried out at 300W until the desired temperature is reached (280°C). During the reaction time (II), the power and temperature are maintained at 280°C and 280W. Once the reaction is complete, the reaction is thermally quenched by compressed air.

given reaction temperature allowing a high power density to be applied to the reaction constituents. In this case it is probable that there is an inside-out thermal gradient in which the highest temperature is found near the center of the solution.

Reaction times are based upon the time at a desired temperature and are chosen according to the desired reaction and nanomaterial size. Once the reaction is complete, the microwave power is turned off to terminate the reaction and the airflow is increased to rapidly cool the solution, quenching the reaction which minimizes colloidal size distributions resulting from Ostwald ripening. All three stages in the microwave are critical in the formation of a narrow size distribution of colloids with high optical qualities as measured by absorption and photoluminescence and will be discussed separately below.

Initiation Phase. The quality of the final nanomaterials is dependent on the initiation of the reaction. It has been suggested that uniformity in heating, introduction of the precursor, and controlled temperature over the course of the reaction are crucial to final product quality^{8, 16, 17}. In standard lyothermal synthetic methods, this tends to be achieved by rapid injection of the precursors at high temperature with the solvent acting to provide the convective heat. To eliminate out-of-control growth in the lyothermal synthesis, the innate cooling of the reaction upon injection of a cold reactant controls the growth phase, although reactant concentration and activity are also important. In the microwave, we believe nanoparticle formation and growth is initiated by selective microwave heating of constituents in the reaction. The selective heating can either be to the precursors or to an organic constituent in the

reaction depending on the reaction type. In either case the local temperature is escalated and forms a uniform thermal field free of gradients. This in turn must provide energy to drive the desired product by overcoming transition states in the reaction trajectory. Unfortunately, while in organic chemistry the microwave dependent effects can be specifically discussed in terms of the reaction trajectory, the lack of an in-depth mechanistic picture for nanoparticle growth makes determination of the exact influence of the microwave on the transition states for nanoparticle formation to be unclear.

The influence on the product formation under microwave heating will depend on the applied microwave power (P) and the competitive microwave cross section of the reactants and passivants in solution, as measured by the heating rate. This of course will be dependent on the microwave cavity design, but the general observations will be relevant to all designs. The heating rate (dT/dt) in a microwave reactor correlates with the real (ϵ') and imaginary (ϵ'') components of the complex dielectric constant (ϵ^*) for the individual components in the reaction mixtures. The microwave absorption cross section is described by the real component while the ability to transfer microwave energy into heat is described by the loss tangent ($\tan \delta = \epsilon'' / \epsilon'$)¹⁴. Molecules with large permanent dipoles will absorb microwave irradiation selectively over molecules with small dipoles. The magnitude of the microwave absorption cross section is therefore dependent on the materials dielectric constant or

permittivity (ϵ'). This value tends to be small for non-polar organic moieties (~2.0 for benzylic molecules) and values of up to 80 for water¹⁴.

Since selective heating in the microwave requires a large dipole, the rate of heating of the reactants in an applied electric field (E) is described by eqn. 1

$$dT/dt = \sigma[E]^2 / \rho C \quad (1)$$

where ρ is the density and C is the specific heat capacity of the molecule, and the molecular conductivity (σ) is related to the imaginary part (ϵ'') of the permittivity function using a Debye relationship, $\epsilon^* = \epsilon' + i\epsilon''$ ¹⁴. In general the value of E is dependent on the cavity design, and therefore not calculable; however the expression indicates that initiation of the nanomaterial reaction is controllable by the dielectric constant of the reactants and therefore the heating rate of the reaction. The temperature ramping depends on the ability of each of the constituent elements in the reaction to absorb microwaves (ϵ) and the solvent thermal conductivity.

The element in the reaction mixture that couples with the microwaves the strongest will give rise to the major component of the heat transfer. If the element is a transition state intermediate along the reaction path it can assist in product formation. If the element is a polar or ionic species, including organic salts or ionic liquids, not involved in the transition states they will contribute to an average increase in the overall reaction temperatures which can also be advantageous.^{18,19}

In the microwave, interpretation of heating rates is complicated by the fact that the temperature is measure at the reaction vessel and is not a direct reflection of

the microscopic reaction temperature. Inspection of the rates does provide insight into the effects of additives to reactions and therefore can provide insight into how to control reaction trajectories. In Figure 4.2, the effect of solvent and reactant choice on reaction heating rates is illustrated for a series of reactions for CdSe at 400W, and InP and InGaP at 300W. In the CdSe reactions, it is clear in Figure 4.2A the heating rates for the reactions with CdSe/HDA/IL (12°C/s) and with TOPO/HDA/CdO (9°C/s) are enhanced relative to heating pure HDA (3°C/s) or the reaction CdSe/HDA (4°C/s). The deviation at 62°C for the HDA and CdSe/HDA curves in Figure 4.2A arise from melting of the HDA (1-aminohexadecane). Upon addition of the ionic liquid 1-hexyl-3-methylimidazolium chloride, the heating rate of the solution increases dramatically due to the large microwave cross section for ionic liquids, as previously observed in microwave driven reactions¹⁸. Likewise, the large heating rate for TOPO/CdO is due to the high absorption cross section for TOPO. The effect of the ionic liquid and TOPO to rapidly heat the bulk solution can be traced back to their selective ability to couple with the microwaves and efficiently convert electromagnetic energy into heat. The effect of the higher heating rate in the presence of the ionic liquids will increase the microscopic reaction temperatures of the reaction. In turn these accelerated heating rates translate to rapid particle growth as discussed below.

The effect of reaction conditions on heating rates in the formation of InP and InGaP are less conclusive and are shown in Figure 4.2B. The rate of heating for the InP and InGaP reactions in ODE and decane are slow, 2°C/s . The largely invariant

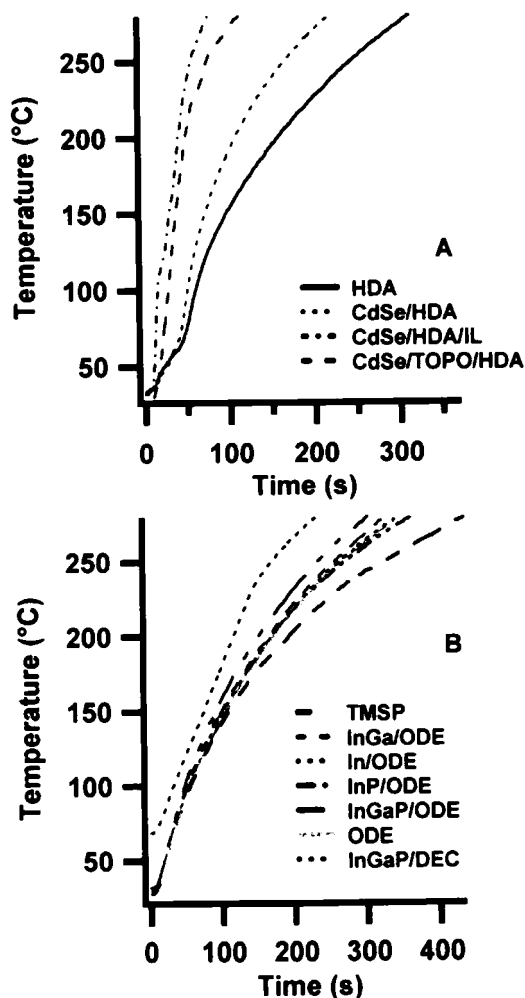


Figure 4.2. Temperature ramping rates for molecular precursors and solvents used in the formation of CdSe at (A) 400W and (B) III-V nanoparticles at 300W. In 2A, HDA is for 5 ml of hexadecylamine, the curve for CdSe/HDA is for a solution containing $\text{Li}_4[\text{Cd}_{10}\text{Se}_4(\text{SPh})_{16}]$ dissolved in HDA, the curve CdSe/HDA/IL represents a solution containing $\text{Li}_4[\text{Cd}_{10}\text{Se}_4(\text{SPh})_{16}]$ in HDA with the ionic liquid (IL) 1-hexyl-3-methylimidazolium chloride added, and the curve for TOPO/HDA/CdO is for a 50:50 V:V mixture of the solvents with CdO and TBPSe added. In 2B, TMSP represents a solution containing tris(trimethylsilyl)phosphine in octadecene; InGa/ODE and InGaP/ODE represents solutions containing the metal salts in a mixture of hexadecanoic acid and ODE; InP/ODE and InGaP/ODE represent identical solutions with TMSP added. The curve for ODE is for 5 ml of technical grade octadecene.

heating rates observed for the different reaction conditions is not surprising when considering the polarizability of the group III precursors is small and the precursor concentrations is low in solution. The observation that octadecene (ODE) and decane show identical heating rate of 2°C/s to the InP and InGaP reactions suggest that only the solvent is absorbing the MW energy. However, this assumption is incorrect since the actual microscopic temperature of the reaction may be substantially higher than measured. The measured rate of solvent heating in Figure 4.2 is dictated by solvent thermal conductivity and thermal load on the solvent. In the case of nanoparticle growth without added ILs, the thermal load is likely to be small since the nanoparticles should thermalize rapidly due to their small size and exist in low concentration.

Growth Phase. During the growth phase for nanomaterials uniform volumetric heating is important to maintain the size focus. In the microwave, the reaction temperature is achieved by uniform volumetric heating which is influenced by the power dissipation to the solvent and the applied power. The dissipation of power per unit volume (P) is described by $P = \sigma[E]^2$, where σ is the conductivity and E is the applied electric field. The applied power influences the temperature of the reaction solution. The temperature of the reaction is mediated by thermal transfer of latent heat from the reactant to the solvent and dissipation by active air-cooling in the microwave. Excess heat will tend to drive Ostwald ripening processes in nanomaterial synthesis.

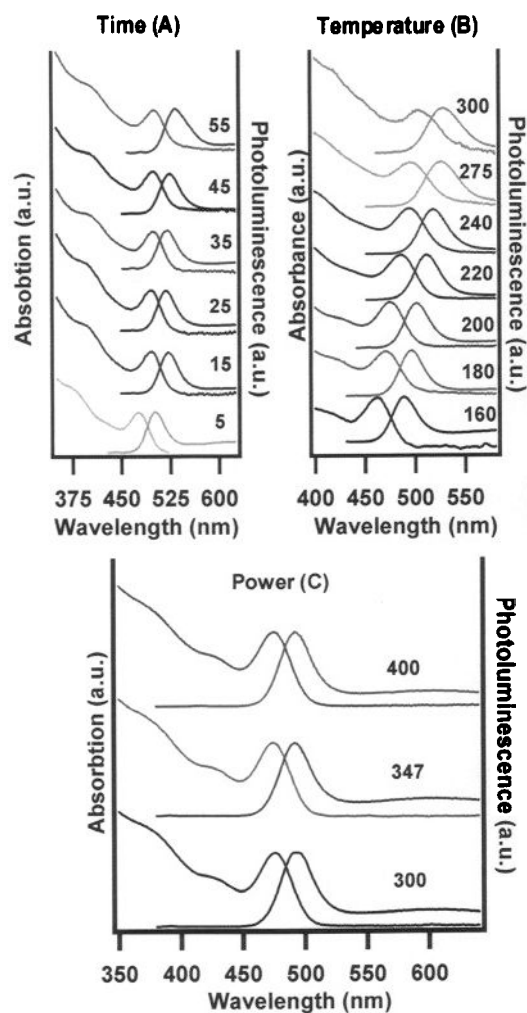


Figure 4.3. Room temperature absorption and photoluminescence of toluene isolated CdSe nanoparticles grown from $\text{Li}_4[\text{Cd}_{10}\text{Se}_4(\text{SPh})_{16}]$ synthesized at various A) power (W), B) time (min) and C) temperature ($^{\circ}\text{C}$). In these graphs, one parameter is varied while the other two parameters (time, power or temperature) remain constant. The variables at which the reactions were carried out are indicated next to the trace.

4.3.1 Growth of CdSe by $\text{Li}_4[\text{Cd}_{10}\text{Se}_4(\text{SPh})_{16}]$

The growth of CdSe nanoparticles is an ideal platform to compare the quality and the rate of growth for nanoparticles grown by convective heating and microwave heating methods. In the following discussion, we separate the influence of additives on the growth of CdSe from a single source precursor route using $\text{Li}_4[\text{Cd}_{10}\text{Se}_4(\text{SPh})_{16}]$ and an added ionic liquids; and the effect of having a solvent that is a strong microwave absorber (TOPO) using a CdO method developed by Peng, et al¹¹. The prepared materials, whether grown convectively or by dielectric heating, are identical with similar absorption features, photoluminescence quantum yields, and similar size dispersities for a given reaction methodology. Significant differences exists between convective and dielectric heating in regards to material handling, where the reactants can be added at room temperature without the need for high temperature injection to produce high quality materials; material growth, where the growth times even for III-V materials is under 15 minutes; and in increased reproducibility from reaction batch to reaction batch.

The influence of microwave power, reaction time, and reaction temperature is demonstrated for CdSe formed from $\text{Li}_4[\text{Cd}_{10}\text{Se}_4(\text{SPh})_{16}]$ in Figure 4.3. In Figure 4.3A the influence of varying time (0-55 m) at fixed power (400W) and fixed temperature (300°C) is investigated. The effect of increasing reaction times past 10 minutes is minimal with regards to size (2nm) as evidenced by the position of the first exciton feature. A change in size distribution is observed for distribution for times longer than 45 min as measured by PL shape and absorption bandwidth. Inspection of

Figure 4.3B shows at a fixed reaction time (40 min) and microwave power (400W) a dependence of size on temperature is clearly observed. The nanoparticle size increases with increasing temperature. Figure 4.3C demonstrates increasing the microwave power from 300 to 400 W for a reaction of 10 min at 210°C does not have a marked effect on the nanomaterial size or the optical quality as measured by absorption excitonic features and photoluminescence. Lower powers are not presented due to the observation of slow heating rates, a difficulty to achieve the necessary reaction temperatures, and poor optical performance of the resultant materials.

The observation of small nanoparticles (~2 nm) even at high power, long reaction times, and high temperature is surprising given that convective heating allows 9 nm CdSe nanocrystals to be isolated after several hours of reaction time¹⁰. We believe this suggests local minima may exist in the reaction trajectory for growth of nanocrystalline CdSe from the precursor methods that require long reaction times to overcome. Local minima along a reaction trajectory may arise even for reactions that are thermodynamically downhill to bulk but due to reconstruction or kinetics may be slow to progress over their transition state to the final product. In fact, surface reconstruction event coupled to surface passivation, as has been suggested by Yu, et al.²⁰ Consistent with this observation, in a recent manuscript Burda, et al indicated a unique stabilization at 2 nm is observed in the growth of nanocrystalline CdSe²¹.

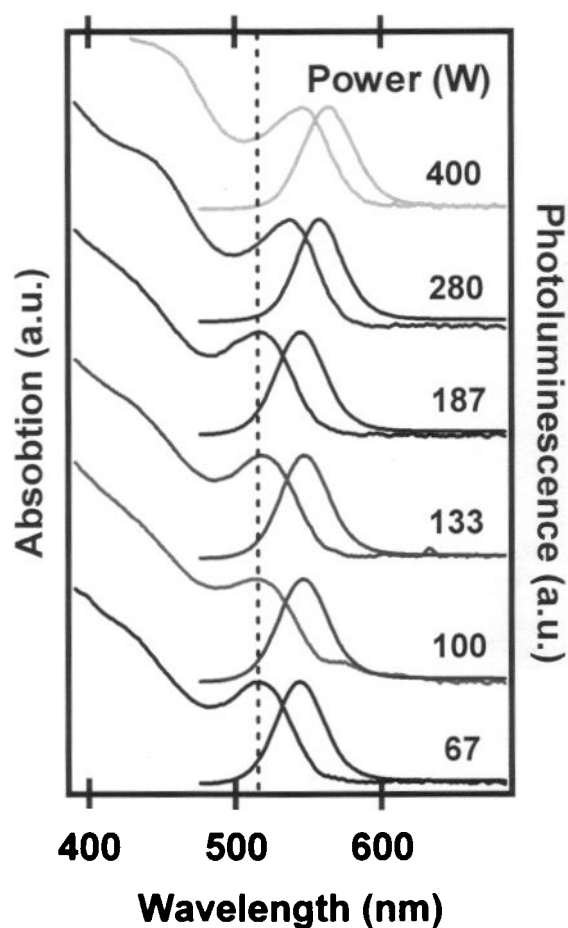


Figure 4.4. Power dependant (W) size characteristics of CdSe nanoparticles formed by microwave heating with ionic liquid addition (1-hexyl-3-methylimidazolium). The applied power was increased from 160 to 400 W keeping the reaction time at 3 minutes and the reaction temperature fixed at 210°C.

4.3.2 Growth of CdSe by $\text{Li}_4[\text{Cd}_{10}\text{Se}_4(\text{SPh})_{16}]$ with 1-hexyl-3-methylimidazolium

The addition of an ionic liquid (IL) to a reaction can increase reaction temperatures due to their strong microwave cross-section, can stabilize transition state species, and can act as catalyst towards growth²². The observed heating rate differences in Figure 4.2, suggests that addition of ionic liquid to HDA in the formation of CdSe may increase the microscopic reaction temperature and in turn may influence nanoparticle growth. Addition of a strong microwave absorber to a reaction has been shown in microwave organic chemistry to increase the microscopic temperature of the reaction, overcome local minima, and push the reaction towards the thermodynamic product²³. In Figure 4.4, it is clear that for CdSe nanoparticles grown in the presence of a 1.1 mol ratio of 1-hexyl-3-methylimidazolium chloride (IL) to the inorganic cluster, a large increase in nanoparticle size from 2 nm to greater than 5 nm in less than 10 minutes is observed. This is further shown in a direct comparison in Supplemental Figure 4.3. A plot of the nanoparticle size versus reaction condition (Figure 4.5) shows a dependence on time, temperature and power in the presence of the ionic liquid. At fixed temperature and time a steady growth is observed without a clear asymptote for size vs. power, suggesting increasing power will increase size (Figure 4.5A). At fixed power and temperature (Figure 4.5B), the nanoparticle approaches an asymptote at ~3.5 nm rapidly. At fixed power and time (Figure 4.5C) the growth is slow to initiate at temperatures below 180°C (3.0 nm), but shows steady growth between 180°C and ~220°C (5.5 nm). The lines in the figure provide a guide to the eye. It is clear that the addition of the IL results in a strong

dependence on the reaction conditions, which was not previously observed. In addition the reaction rate is accelerated, suggesting that reaction barriers are overcome by heat transfer to the reactants mediated through the solvent or by displacing the amine passivating ligands, as has been observed when ODE is added as a non-passivant to lyothermal synthesis²⁴.

A plot of the change in QY with reaction condition appears in Figure 4.5. The measured QY²⁵ for the cluster grown materials is within experimental error as a function of power (56 - 64%), but not for time (20 - 52%), and temperature (28-70%). In all cases, the QYs are experimentally similar for a given size and the observed variance with time and temperature may reflect the larger change in size for these conditions. It is important to note that the maximum QY obtained for the single source materials for a core-only nanocrystal achieved a reproducible maximum value of ~70% for a 5.5 nm dot (Figure 4.5C). Further changes in passivant and core-shelling would allow QYs to be obtained at the same level as the best reported materials to date. Due to the high self-absorptivity of these materials, the QY measurements were conducted in thin path configurations analogous to methods applied for high efficiency laser dyes as outlined in the experimental.

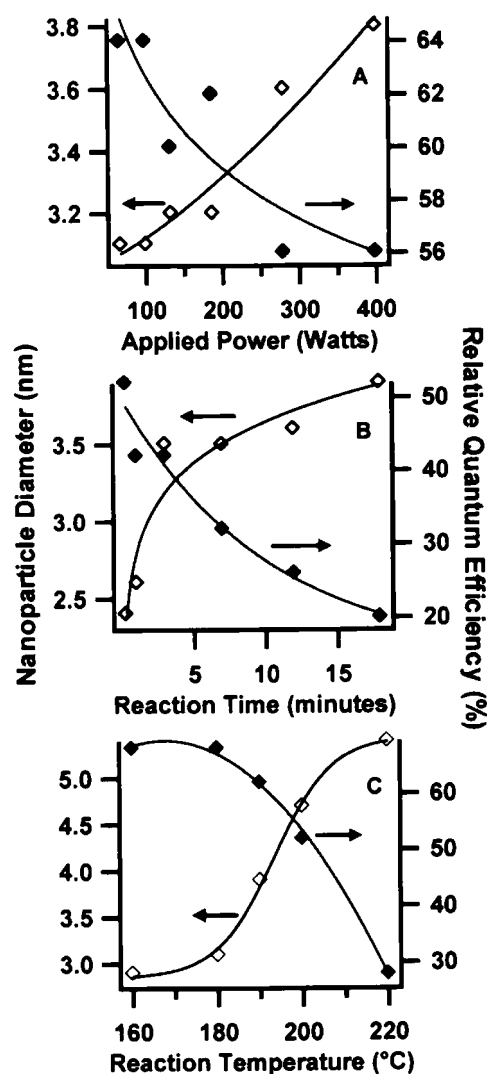


Figure 4.5. Nanoparticle diameter and quantum efficiency (QY) of CdSe synthesized at (A) various power (W) at 3 minutes and 210 °C, (B) various time (min) at 100 W and 220 °C and (C) various temperatures for 10 minutes at 220 W. The QY was measured at RT in a thin path configuration using a 4 mm x 10 mm quartz cuvette on a 10⁻⁸ M solution of the nanoparticle in toluene relative to Rhodamine R6G in ethanol at RT.

4.3.3 Growth of CdSe by CdO

Strong microwave absorbers in a reaction can drastically accelerate the rate of material formation. This is very evident upon inspection of the synthesis of CdSe from CdO in TOPO (tri-octylphosphine oxide). TOPO, which has a large static dipole, is a strong microwave absorber, as evidenced by the rapid heating rate observed in Figure 4.2. Figure 4.6 illustrates the growth of CdSe as a function of temperature in a microwave reactor at 300 W and a fixed power of 160W. The CdSe nanomaterials have well-defined excitonic features and QYs on the order of 74% consistent with previously published materials in the literature³⁴. More importantly, these materials are combined at 50°C (to maintain reaction liquidity), require no high temperature injection step, no multiple injection for size focusing, and can be isolated within 30s of initiating the reaction regardless of the desired size. It is clearly observed that a very narrow size distribution is maintained throughout the reaction for all sizes with no PL defect emission.

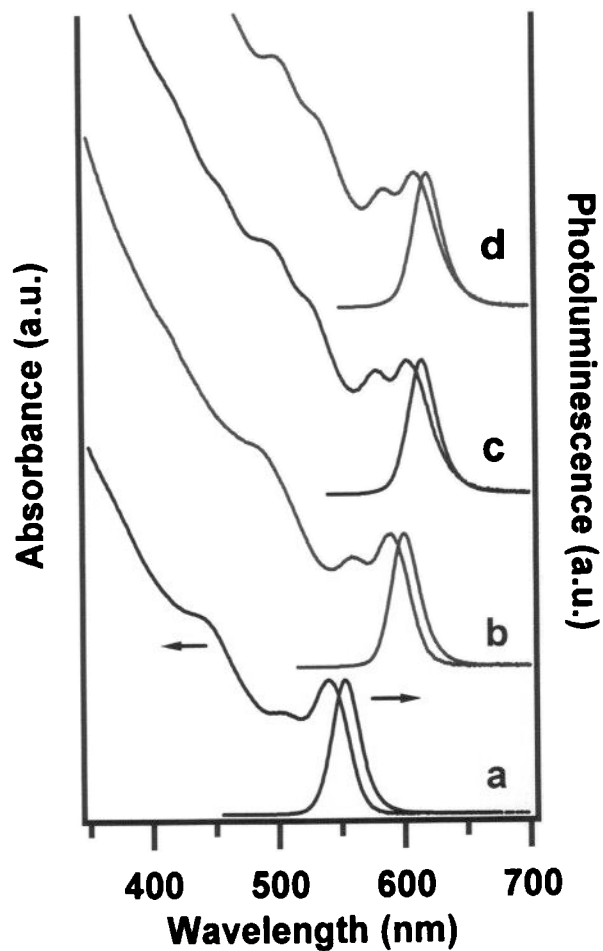


Figure 4.6. Absorption and photoluminescence in toluene of CdSe prepared in the microwave by CdO in hexadecylamine and triethylphosphine oxide. The reactions were carried out at a) 200 °C, b) 240 °C, c) 280 °C, d) 300 °C for 30 s at 160 W to achieve different sizes. No active cooling was applied.

4.3.4 Growth of InGaP

Formation of III-V materials is notorious for its difficulty and required long reaction times (h). Microwave heating has been shown to be advantageous in such cases. In organometallic reactions in the microwave, superheating of the solvent and vessel pressurization has been shown to give rise to a 1000 fold increase in reaction rate²⁶. More interestingly, it has been observed that when the polarity of the solvent is decreased (i.e. when the solvent becomes more transparent) for some synthesis, the observed reaction rate and product yield increase. This implies that there is a stronger microwave – material interaction in the more transparent solvents giving rise to microwave specific effects²⁷.

The formation characteristics for InGaP nanoparticles by microwave heating are compared between a high boiling, non-coordinating solvent ODE and a low boiling solvent decane. ODE and other alkane and alkene non-coordinating solvents provide an ideal reaction system to study the effects of microwave – material interaction due to their relative transparency to the microwave field. As seen in figure 4.7A, the formation of InGaP in ODE under constant temperature and power shows a focusing of size distribution⁸ with a reduction of size at longer reaction temperatures during a reaction time from 30 seconds to 7 minutes.

At 7 minutes, the size distribution and PL are maximized, when the applied power is 280 W and the reaction temperature is 280°C. With time, the onset of the first exciton and the quality of the PL becomes more resolved with a final size of 4.0 nm. Inspection of the reaction at variable temperature (P = 280W, t = 7m) and

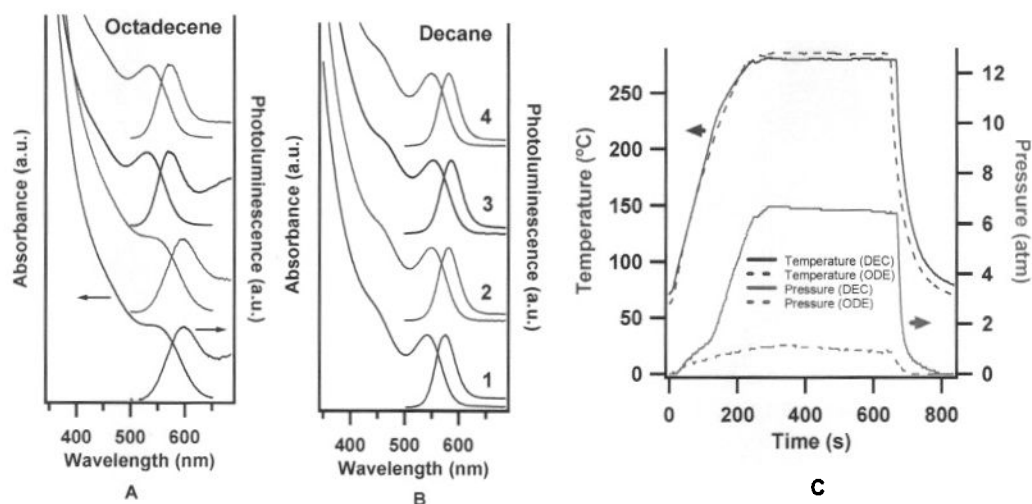


Figure 4.7. Growth characteristics of InGaP at 280 °C and 280 W in a high boiling non-coordinating solvent (A) octadecene (ODE) and a low boiling (B) decane (DEC). The reaction time in both solvents was (B1) 30 seconds, (B2) 1 minute, (B3) 3 minutes, and (B4) 7 minutes. (C) Shows the temperature (°C) and pressure profiles (atm) of the reaction consisting of the high boiling, ODE and low boiling, decane, non-coordinating solvents.

variable power ($T = 280^{\circ}\text{C}$, $t = 7\text{m}$) suggests that while reaction temperature is critical for observing a clear excitonic feature ($>280^{\circ}\text{C}$), no effect on the excitonic feature is observed for power between 230 and 300 W/cm^2 with a fixed reaction temperature of 280°C . Inspection of the PL is more informative. The QY increases steadily with increasing applied power from a value $< 1\%$ ($P = 230\text{ W}$) to a value of 4% at 300 W in ODE. While this number is low compared to CdSe, it is on the order of QY's measured for thermally grown InP samples isolated from reaction²⁸. Following chemical etching in HF, as described in the literature, the QY increases to a maximum value of 68% due to removal of surface defects^{29, 30}.

The influence of reaction pressurization on the rate of growth and quality of materials for InGaP nanocrystals is clearly observed in Figure 4.7B. The same reaction carried out in decane rather than ODE produce astonishingly well-resolved excitonic features for InGaP of roughly the same size. It is clear that the size remains nearly constant and that the size distribution becomes focused around 1 minute (Figure 4.7B-2) and remains constant up to 7 min. The PL quantum efficiency for the decane reaction ranges from 9% for a 30s reaction to 15% for the 7 min reaction. This is the first report, to our knowledge, of quantum efficiencies of a chemically non-etched, un-size selected III-V system that exhibits quantum efficiencies of this magnitude. Comparing the formation rate of InGaP in ODE and decane, it is apparent that the quality and rate is dramatically enhanced in decane. Chemical etching with HF produces QYs of the same level as the samples grown in ODE. This suggests that

a reaction in super-heated solvents overcomes local defect driven minima in the reaction trajectory producing more narrowly sized and optically better materials.

Although no size dependent trends are observable for InGaP in either decane or ODE, the change in the absorption features and the PL properties are indicative of particle annealing and size focusing. Different sizes of InGaP can be obtained by microwave methods, although the details do not appear in the manuscript to maintain the focus on the methodology rather than the specific material. Details on size dependence and optical properties of InGaP, InP, and InP/ZnS core shell prepared in the microwave will be reported in a future manuscript³¹. With increasing reaction temperature or applied power, the PL shows a loss of defect emission coupled to increased quantum efficiencies for the nanomaterials. These effects are more important in the ODE grown materials suggesting the reaction may be moderated by nanoparticle reconstruction or defect formation, such as vacancies or glide plane defects influencing the growth of these materials. Consistent with the experimental observations, at higher temperature or longer reaction times, particle annealing would be enhanced due to an increase in diffusion of the vacancies to the nanomaterial surface following a Boltzman dependent diffusion process and the expectation of defect migration by Fick's law towards the surface of the nanomaterial. In contrast to the material formed in ODE, decane appears to promote a stronger coupling of the microwave - nanomaterial interaction. This is seen in the superheated decane reaction compared with that of ODE (Figure 4.7C). When the reaction containing decane approaches 200°C the pressure increases rapidly until it is sustained at 6.2 atm

for the duration of the reaction. It is observed from both reactions in ODE and decane that there is a rise in pressure at the onset of the reaction suggesting that there is a volatile bi-product that is liberated as the nanoparticle reaches its maximum size. This is possibly a low boiling organic that diffuses back into solution when the reaction is cooled.

4.3.5 Growth of InP with Ionic Liquids

InP Nanoparticle Formation. The influence of vacancies, defects, and surface energies on nanomaterials surface is apparent when the reaction conditions required for formation of InGaP and InP are compared. The InP materials exhibit a significantly longer reaction time for a maximum in the PL quantum efficiency to be observed. For growth of InP in ODE, the optimum reaction time was found to be 15 minutes at 280°C with an applied power of 280W (Figure 4.8a) without any additives. InP shows similar trends in material size distribution and optical quality with power, and temperature in analogy to the InGaP samples. The quantum efficiency of the as prepared (non HF etched) InP material under optimal reaction condition is 4% with a value of 38% following HF etching.

The drastic increase in reaction time suggests that the surface in InGaP more easily anneals than the binary system. This is not surprising in that a defect ion has been observed to increase reaction rates in II-VI materials^{32, 33} Alternatively, the enhanced rate for InGaP growth may be influenced by the formation of an In/Ga flux at the nanomaterial surface during the synthetic reaction. Burho, et al. has suggested

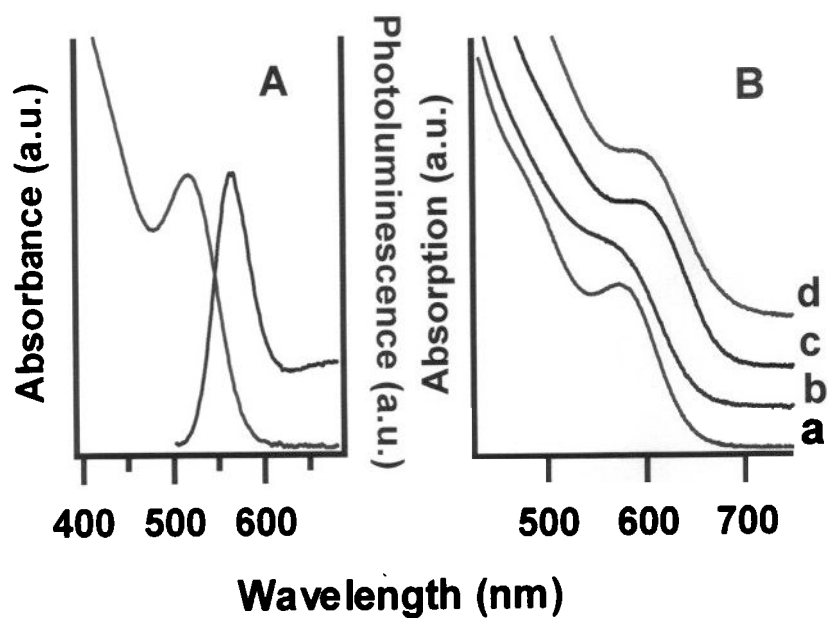


Figure 4.8. Absorbance and photoluminescence of InP in toluene (A). Absorbance of a series of InP nanoparticles in formed in the presence of ionic liquids at 280 °C for 15 minutes at 280W: a) as prepared InP nanoparticles with no ionic liquid present, b) InP with trihexyltetradecylphosphonium decanoate, c) InP with trihexyltetradecylphosphonium bromide, d) InP with trioctylphosphine oxide

that InP grows at the interface of an In^0 droplet. In this case the In/Ga flux may lower the activation barriers in the reaction and the Ga would be expected to isolate at or near the nanoparticle surface. In fact, recent NMR and XPS studies suggest the Ga isolates at or near the surface (unpublished results). Continuing studies to elucidate the growth mechanism in low boiling solvents and the influence of ionic liquids on the formation characteristics are ongoing in the laboratory.

Inspection of the influence of strong microwave absorbers (IL's and TOPO) on the growth of InP is a more complicated issue than for the II-VI materials, possibly due to interactions of the IL with the precursors. The observations are dependent on the nature of the IL (imidazolium vs. phosphonium) and require further studies to fully elucidate the influence on the reaction mechanism on InP growth. In the presence of the 1-hexyl-3-methylimidazolium chloride IL, the nanomaterial precipitates to form an insoluble orange residue. This is presumably either a cluster or a small coordination complex although clear identification of the product is still under investigation. When a phosphonium based IL is added such as trihexyltetradecylphosphonium decanoate or trihexyltetradecylphosphonium bromide, no precipitation is observed; however, the onset of the first exciton is shifted relative to the reaction carried out in the absence of the IL (Figure 4.8B) and show no visible PL. The addition of TOPO results in a broadening of the absorption feature and has substantially lower quantum efficiency. In both additive cases (IL or TOPO) etching does not produce a substantial improvement of the PL performance over the reaction carried out in the absence of the additive. In addition, additives appear to broaden the

size distribution. While additives have a marked effect on nanoparticle growth and quality, the effect is not advantageous in the III-V family. At this time the negative influence on quality would only be speculative in the absence of a well-understood reaction mechanism.

4.4 Conclusion

Dielectric heating is advantageous to the formation of nanocrystals. High operating powers and temperatures in the MW cavity allow nearly mono-disperse high quality nanomaterials with QY's up to 74% to be rapidly generated in under 20 min. The use of the microwave eliminates thermal gradients by volumetric heating, eliminates the need for high temperature injection for size focusing, and is scalable for commercialization. The influence of additives, power, temperature, and time is demonstrated for both the II-VI and III-V nanocrystalline systems. While the exact nature of the microwave specific effect is difficult to define for these materials due to their complex reaction trajectories, it is clear that the method can be tuned to optimize reaction conditions for specific materials. For instance, addition of ionic liquids that raise the rate of heating improves the growth rate for CdSe, while higher reaction pressures enhance the formation of III-V materials. This suggests that the nature of the transition states for growth in these systems is different and may be influenced by surface or defect formation.

The observed reaction rate enhancement and size focusing in nanocrystalline materials grown under dielectric heating conditions may arise from elevated reactant

temperatures due to selective heating coupled to rapid cooling through thermalization. Because in the microwave, the reactions are volumetrically heated, thermal gradients tend to be minimized which results in a more uniform reaction. Selective heating arises from the relative differences in solvent and reactant dielectric constants. This means that the microscopic temperature instantly rises when the microwave field is applied. The implication is that the internal temperature of the reaction at or near the nanoparticle surface is significantly higher than what is detected by the infrared detector which ultimately reads the vessel temperature. Rapid thermalization to focus the nanoparticle size is achieved because of the high surface to volume ratio of nanoparticles below 7 nm coupled with the fact that they are colloidally suspended in solution. This tends to enhance the thermal field within the reaction matrix regardless of which direction the heat is transferred, either from particle to solvent or solvent to particle.

In addition the observations in this manuscript indicate that additives or pressurization can accelerate growth and suggests vacancy, defect, or reconstruction processes influence the growth behavior of these materials along the reaction trajectory. This synthetic strategy can be tailored to a host of nanomaterials to enhance the efficiency of the nanomaterial discovery and the optimization of nanostructured materials. Moreover, the III-V nanomaterials and the harsh environment and high temperatures needed for growth is no longer a limiting factor governing industrial scalability of such materials. The ability to control the reaction with microwaves offers a more environmental approach to colloidal semiconducting

nanoparticles. The demonstration of microwave techniques effectively automates the synthetic process, and more importantly demonstrates the use of a continuous flow microwave reactor for nanoparticle formation.

4.5 References

1. Gedye, R. N.; Wei, J. B., *Canadian Journal of Chemistry-Revue Canadienne De Chimie* **1998**, 76, (5), 525-532.
2. Nuchter, M.; Ondruschka, B.; Bonrath, W.; Gum, A., *Green Chemistry* **2004**, 6, (2), 128-141.
3. Kappe, C. O., *Angewandte Chemie-International Edition* **2004**, 43, (46), 6250-6284.
4. Lidstrom, P.; Tierney, J.; Wathey, B.; Westman, J., *Tetrahedron* **2001**, 57, (45), 9225-9283.
5. Guzelian, A. A.; Katari, J. E. B.; Kadavanich, A. V.; Banin, U.; Hamad, K.; Juban, E.; Alivisatos, A. P.; Wolters, R. H.; Arnold, C. C.; Heath, J. R., *Journal of Physical Chemistry* **1996**, 100, (17), 7212-7219.
6. Heath, J. R.; Shiang, J. J., *Chemical Society Reviews* **1998**, 27, (1), 65-71.
7. Talapin, D. V.; Rogach, A. L.; Mekis, I.; Haubold, S.; Kornowski, A.; Haase, M.; Weller, H., *Colloids and Surfaces a-Physicochemical and Engineering Aspects* **2002**, 202, (2-3), 145-154.
8. Peng, X. G.; Wickham, J.; Alivisatos, A. P., *Journal of the American Chemical Society* **1998**, 120, (21), 5343-5344.

9. Strouse, G. F. G., J.A.; Magana, D. Method for Synthesis of Colloidal Nanoparticles., Patent Pending
10. Cumberland, S. L.; Hanif, K. M.; Javier, A.; Khitrov, G. A.; Strouse, G. F.; Woessner, S. M.; Yun, C. S., *Chemistry of Materials* **2002**, 14, (4), 1576-1584.
11. Qu, *Journal of the American Chemical Society* **2001**, 124, (9), 2049-2055.
12. Battaglia, D.; Peng, X. G., *Nano Letters* **2002**, 2, (9), 1027-1030.
13. Loupy, A., *Microwaves in organic synthesis*. Wiley-VCH: Weinheim ; Cambridge, 2002; p xxiv, 499.
14. Thostenson, E. T.; Chou, T. W., *Composites Part a-Applied Science and Manufacturing* **1999**, 30, (9), 1055-1071.
15. Jones, D. A.; Lelyveld, T. P.; Mavrofidis, S. D.; Kingman, S. W.; Miles, N. J., *Resources Conservation and Recycling* **2002**, 34, (2), 75-90.
16. Murray, C. B.; Kagan, C. R.; Bawendi, M. G., *Annual Review of Materials Science* **2000**, 30, 545-610.
17. Talapin, D. V.; Rogach, A. L.; Shevchenko, E. V.; Kornowski, A.; Haase, M.; Weller, H., *Journal of the American Chemical Society* **2002**, 124, (20), 5782-5790.
18. Leadbeater, N. E.; Torenius, H. M., *Journal of Organic Chemistry* **2002**, 67, (9), 3145-3148.
19. Antonietti, M.; Kuang, D. B.; Smarsly, B.; Yong, Z., *Angewandte Chemie-International Edition* **2004**, 43, (38), 4988-4992.

20. Yu, W. W.; Wang, Y. A.; Peng, X. G., *Chemistry of Materials* **2003**, 15, (22), 4300-4308.
21. Chen, X. S., A.; Lou, Y.; Burda, C., *Journal of the American Chemical Society* **2005**, 127, (12), 4372-4375
22. Chiappe, C.; Pieraccini, D., *Journal of Physical Organic Chemistry* **2005**, 18, (4), 275-297.
23. Eames, J.; Kuhnert, N.; Sansbury, F. H.; Warren, S., *Synlett* **1999**, (8), 1211-1214.
24. Peng, Z. A.; Peng, X. G., *Journal of the American Chemical Society* **2001**, 123, (1), 183-184.
25. The relative quantum efficiencies were obtained using the following expression,

$$\phi_{em} = \phi'_{em} (I / I') (A' / A) (n / n')^2$$
 Where I (sample) and I' (reference) are integrated emission peak areas. A (sample) and A' (reference) are the absorbances at the excitation wavelength, and n (sample) and n' (reference) are the refractive indices of the solvents. ϕ'_{em} is the quantum efficiency of the reference
26. Mingos, D. M. P.; Baghurst, D. R., *Chemical Society Reviews* **1991**, 20, (1), 1-47.
27. Loupy, A.; Perreux, L.; Liagre, M.; Burle, K.; Moneuse, M., *Pure and Applied Chemistry* **2001**, 73, (1), 161-166.
28. Lucey, D. W.; MacRae, D. J.; Furis, M.; Sahoo, Y.; Cartwright, A. N.; Prasad, P. N., *Chemistry of Materials* **2005**, 17, (14), 3754-3762.

29. Micic, O. I.; Nozik, A. J.; Lifshitz, E.; Rajh, T.; Poluektov, O. G.; Thurnauer, M. C., *Journal of Physical Chemistry B* **2002**, 106, (17), 4390-4395.
30. Talapin, D. V.; Gaponik, N.; Borchert, H.; Rogach, A. L.; Haase, M.; Weller, H., *Journal of Physical Chemistry B* **2002**, 106, (49), 12659-12663.
31. Unpublished Results.
32. Hanif, K. M.; Meulenberg, R. W.; Strouse, G. F., *Journal of the American Chemical Society* **2002**, 124, (38), 11495-11502.
33. Treadway, J. A. Z., D.A. Luminescent Nanoparticles and Methods for Their Preparation. 20030017264, 2003.

Chapter 5. Formation Characteristic and Photochemical Etching of InGaP

5.1 Introduction

Research in colloidal semiconducting nanoparticles have centered around applications in solid state lighting¹, ultra thin display² and fluorescent biological tagging³⁻⁵. In recent years many advances have been made for the integration of fluorescent semiconducting nanoparticles, namely CdSe, into polarized fluorescence devices⁶⁻⁹, biological assemblies^{3, 4, 10-12} and solar cells¹³⁻¹⁶.

The commercial applications of these devices are limited in part due to the toxicity associated with cadmium and selenium. InP is a more suitable choice for realistic device application because of its integration into current commercial devices. However, the limiting factors for device quality InP nanoparticles are inherently slow reaction rates in concert with high temperatures for the growth and more important, low quantum yields (QY) associated with the as prepared material.

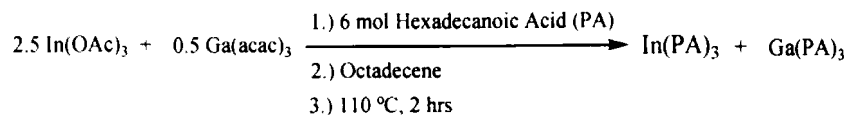
In chapter 4 of this thesis a microwave synthesis approach was introduced as a technique that showed to be useful for the rapid preparation of II-VI and III-V nanoparticles, on the order of minutes which eliminates the need for high temperature injections. This method relies on heating at the atomic scale rather than bulk scale. This is directly advantageous to nanoparticle formation because much of the quality of the as prepared material is centered on uniform nucleation (rapid heating) and controlled sized distribution (uniform thermal field).

This chapter is an extension of the chapter 4 to the study of a ternary III-V semiconducting nanoparticle $\text{In}_{1-x}\text{Ga}_x\text{P}$. The formation characteristics, crystallite size tunability and photochemical etching is examined with dilute solutions of HF to increase the as prepared quantum efficiency from 0.04 to a maximum of 0.80.

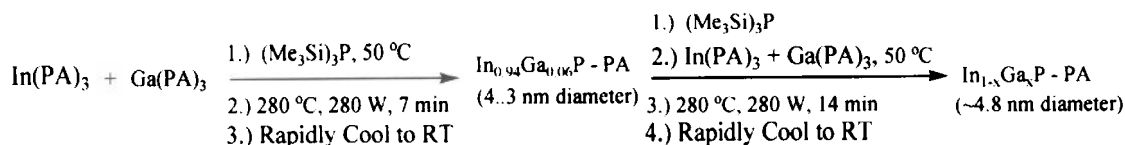
5.2 InGaP Size Tunability

This section will describe how to tune crystallite diameters by choosing the appropriate additives and multiple injections of precursors. The importance in maintaining a strict cation:anion ratio was explained chapter 4. Unlike the II-VI coordinating/noncoordinating solvent growth (ref), the size is highly dependant on stoichiometric additives like tertiary amine and phosphine solvents. A larger crystallite diameter particle is isolable if additional reactants are injected after the initial growth period. Scheme 5.1 illustrates the synthetic approach that was used to achieve the larger sizes, ~ 4.8 nm.

The preparation of the In and Ga precursors (Scheme 5.1) is described in chapter 4 in detail. Briefly, 55 μmol of cations are placed in a microwave vessel with 27.5 μmol of TMSP. The reactants were heated to 280 $^{\circ}\text{C}$ for seven minutes. The vessel was cooled to room temperature and an additional 55 μmol of cations and 27.5 μmol of TMSP were injected. The mixture was then heated to 280 $^{\circ}\text{C}$ for 7 minutes and cooled to room temperature. Figure 5.1 shows that the exciton shifts to the red



Scheme 1



Scheme 2

Scheme 5.1. Synthetic scheme used to isolate multiple sizes of InGaP nanoparticles in octadecen/palmitic acid upon multiple injections by dielectric heating.

with more pronounced structure in the higher level excitonic states. The photoluminescence shows a blue shoulder most likely due to smaller particles from the secondary injection. At a reaction time of 14 minutes, the size distribution begins to narrow while the exciton shifts slightly to the red. This growth mechanism is thought to go by Ostwald ripening process where the smaller InGaP serve as the nuclei that add to the surface of the larger, more stable, particles. These materials are estimated to be 5.2 nm by absorbance spectra and TEM.

Scheme 5.2 outlines the general synthetic strategy to achieve multiple sizes by addition of tertiary ligands. Keeping all reactant concentrations equal and reaction temperature and time the same, the addition of a tertiary Lewis base has a marked effect on the diameter of the nanocrystals keeping the reaction temperature, power and

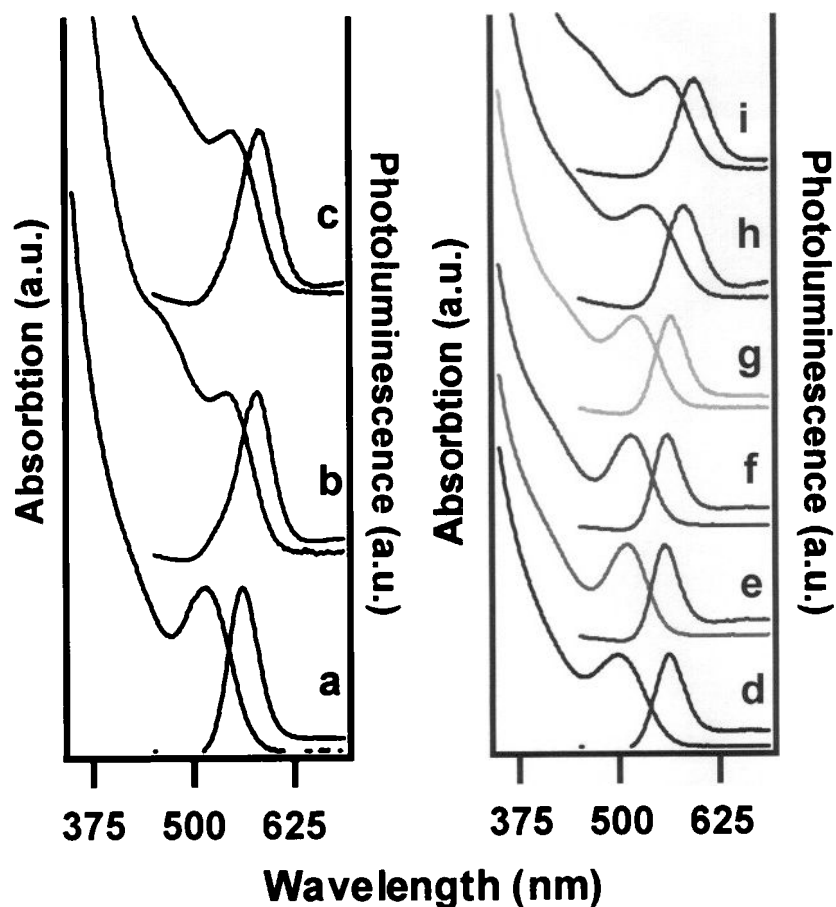
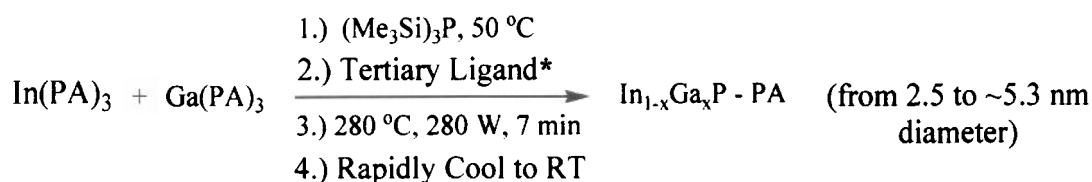


Figure 5.1. Room temperature absorption and photoluminescence of InGaP nanoparticle size dependence on multiple reactant injections: as prepared (a), injection of equal mole reactants with additional 7 min reaction time (b) and 14 min reaction time (c). Traces d-i represent tertiary ligand effects. TOP:cation ratio is 41 (d), 20 (e), 4.1 (f), no tertiary ligand (g), TOA:cation is 4.2 (h), 21 (i).

time constant. Trioctylamine (TOA) was added in place of trioctylphosphine (TOP) to examine whether the binding affinity of TOA towards In^{3+} has an effect on the final diameter. Factors to consider in the ligation ability of N vs P towards In^{3+} is hard/soft basicity and steric effects (chapter 2).



*Trioctylphosphine (TOP) or Trioctylamine (TOA)

Scheme 1

Scheme 5.2. Synthetic scheme used to isolate multiple sized of InGaP nanoparticles in octadecen/palmitic acid with secondary tertiary ligands by dielectric heating

Originally the presumption was the addition of TOP produced smaller diameter particles by simply diluting the precursors where the particle growth proceeds by an inversmicell mechanism. However, the addition of TOA at the same concentrations as TOP (figure 5.1) promotes larger particle growth.

Figure 5.1d-i illustrates opposite effects in terms of final particle size when the tertiary ligand to In^{3+} mol ratio is the same for each experiment. Tertiary nitrogen is a harder Lewis base than phosphorous, and a tertiary nitrogen has increasing back strain as the alkyl chain length increases which reduces the sigma binding ability of the nitrogen.

In the case of TOP, the optical properties are actually enhanced in the range from 4 to 20 mol excess to In^{3+} with narrow FWHM and more intense photoluminescence. There is no distinguishable difference in the optical properties when TOA is used between 1 and 10 mol excess. However, when the mol excess becomes greater than 10, the photoluminescence intensity begins to decrease along with an increase in the size distribution. This is consistent with size dependant CdSe photoluminescence.

The tertiary ligand does not affect diameter when it is injected after the cations and anion have been mixed. Injection of TMSP into the cation solution at 50 °C makes a clear yellow precursor solution that is stable for days. The absorbtion of the yellow solution shows an exciton centered at 450 nm indicating a preassociated InGaP complex.

5.3 InGaP and InP Photochemical Etching

This section examines photo-assisted fluoride etching and its influence on the photoluminescent quantum yield of InGaP. Hydrofluic acid (HF) etching of III-V semiconductor nanocrystals has been shown to significantly improve the quantum efficiency, especially InP^{17, 18}. In recent years, researchers have studied the correlation between optical properties and molecular structure in HF etched InP quantum dots¹⁹⁻²². Nozik et al. has suggested that HF etching of InP quantum dots passivates surface phosphorus vacancies by F^- through electron paramagnetic resonance (EPR) and optically detected magnetic resonance (ODMR)^{23, 24}.

Talapin and co-workers have examined the F^- etching by synchrotron photoelectron spectroscopy^{22, 25, 26} (XPS) and demonstrated the removal of unpassivated surface phosphorus atoms from the quantum dot. Their conclusion was that an excess of trioctylphosphineoxide (TOPO) in solution or fluorine from the etching process increases surface passivation, hence there is a significant increase in the observed quantum efficiency.

Bulk photochemical etching studies on InP (refs) have proposed a mechanism for the photolytic etching process²⁷⁻³⁰. When InP is subjected to near UV irradiation or incident light higher in energy than the band gap, the photogenerated hole is captured by the phosphorous surface. This activates the phosphorous surface atom for fluorine attack which in turn promotes the slow dissolution of InP molecular species.

A typical photo-chemical etching experiment follows the schematic shown in figure 5.2. A solution of InGaP (or InP) is suspended in toluene. The optical density is between 0.25 and 0.3. The solution is irradiated by a 365 nm diffuse light source. The photo-etching process is initiated by the addition of a 5 % HF/BuOH solution. During the etching process, mechanical stirring is needed to enhance the uniformity since the intensity of the incident light falls off exponentially in towards the bulk solution.

Figures 5.3a and b show the absorbance and photoluminescence profiles of InGaP after 12 hours of photochemical etching. Both the wavelength of the excitation and the concentration of HF have an influence on the etching rate. Figure

5.3a shows the etching rate increases with increasing HF concentration under 367 nm excitation. As the concentration of HF increases in solution, the etching rate increases to yield smaller ensembles of quantum dots based on the blue shift in the first exciton. It is also noted that as the HF concentration approaches 13 μM , the monodispersity decreases as seen in the loss of the exciton and an increase in the band width of the photoluminescence. The quantum yields are 0.05, 0.13, 0.21, 0.28 and 0.41 respectively as the concentration of HF increases.

Figure 5.3b shows a similar etching rate at 458 nm excitation. As the HF concentration approaches 13 μM , the exciton shows a greater degree of monodispersity is maintained coupled with a slower etching rate. The quantum yield increases and follows the increasing HF concentration: 0.05, 0.15, 0.17, 0.22 and 0.30.

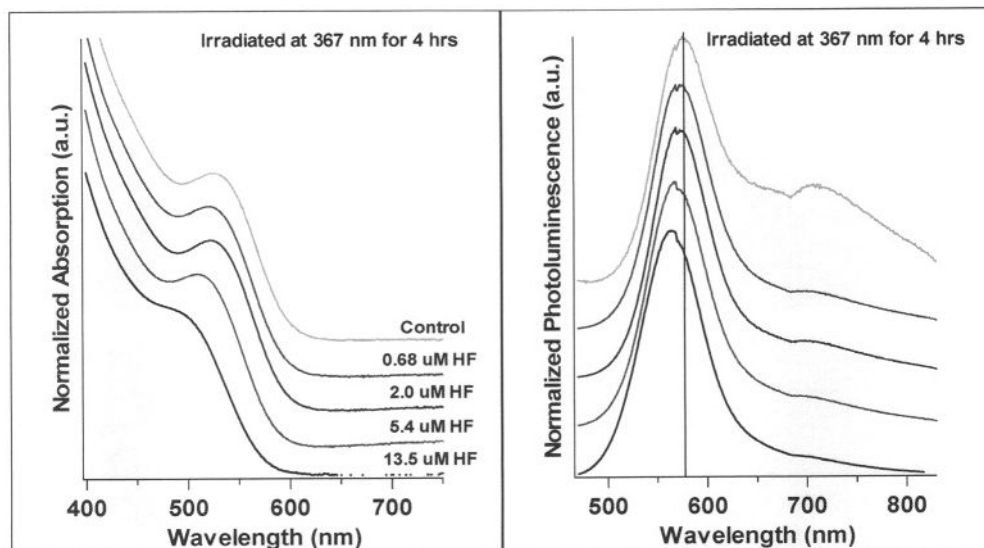


Figure 5.3a. Photo-assited HF etching of InGaP nanoparticles in toluene at various concentration of F^- . The excitation wavelength was set at 367 nm from an Ar ion source. The reaction time was 12 hours at room temperature in sealed vials to prevent evaporation of the solvent.

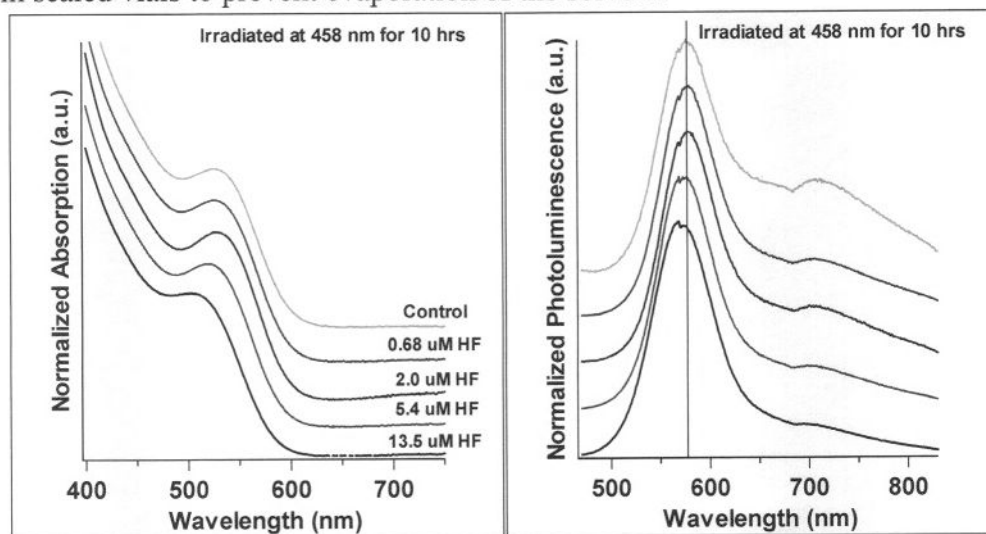


Figure 5.3b. Photo-assited HF etching of InGaP nanoparticles in toluene at various concentration of F^- . The excitation wavelength was set at 458 nm from an Ar ion source. The reaction time was 12 hours at room temperature in sealed vials to prevent evaporation of the solvent.

The size distribution increase during photo-chemical etching is an interesting phenomenon. It is known from the literature that the etching rate of InP is specific to different faces^{19, 28, 31-33}. In combination with face selective etching and inhomogeneous excitation in solution will contribute to broader size dispersity within the ensemble. Figure 5.4a shows the optical absorbance and photoluminescence of pre and post HF etched InGaP using the same method previously discussed. The TEM of two distinct sizes of quantum dots highly irregular shapes which may indicate face specific etching.

The crystallinity and phase is maintained during the etching process. Figure 5.4b shows the pXRD of pre and post etched InGaP. It is clear that the cubic phase of InP is maintained with a loss of the minor reflection centered at 20 2theta. This is not associated with the structure of the nanoparticle but a bi-product of the reaction in the form of SiO₂. Upon HF etching, the SiO₂ is readily dissolved. This is further in the following sections.

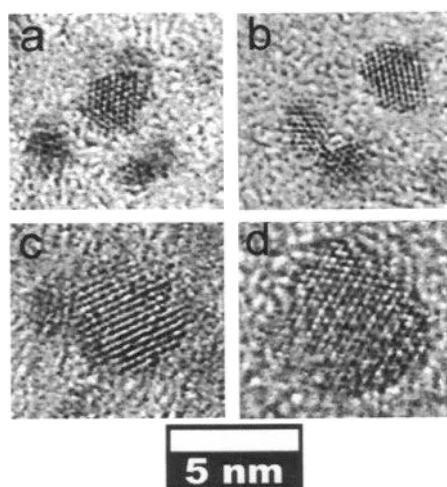
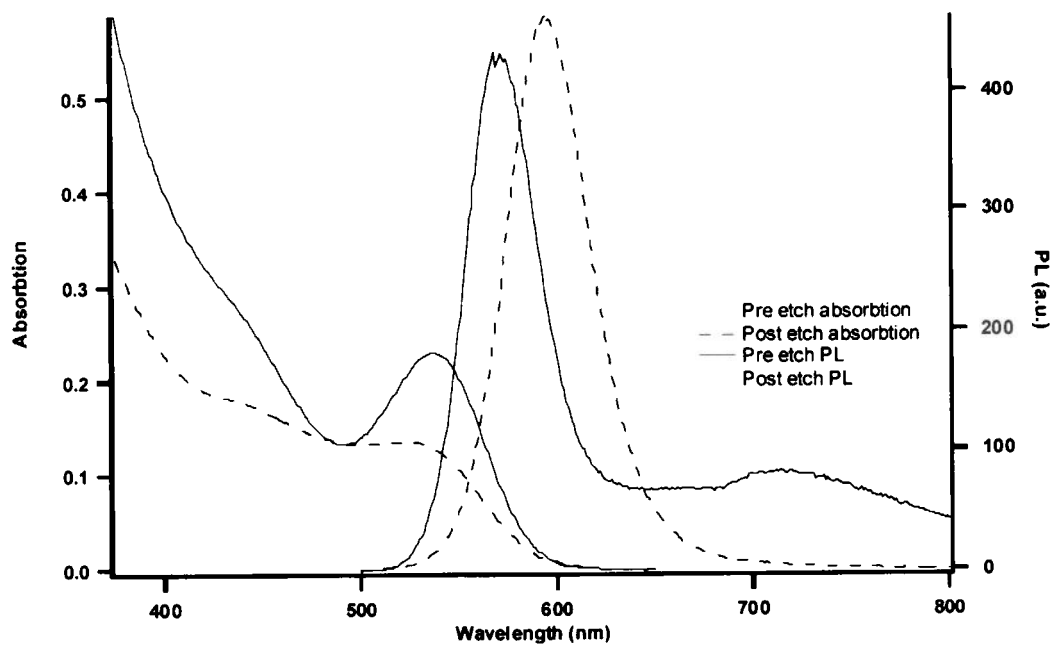


Figure 5.4a. Room temperature absorbance and photoluminescence of pre and post etched InGaP and representative TEM images of post etched colloids

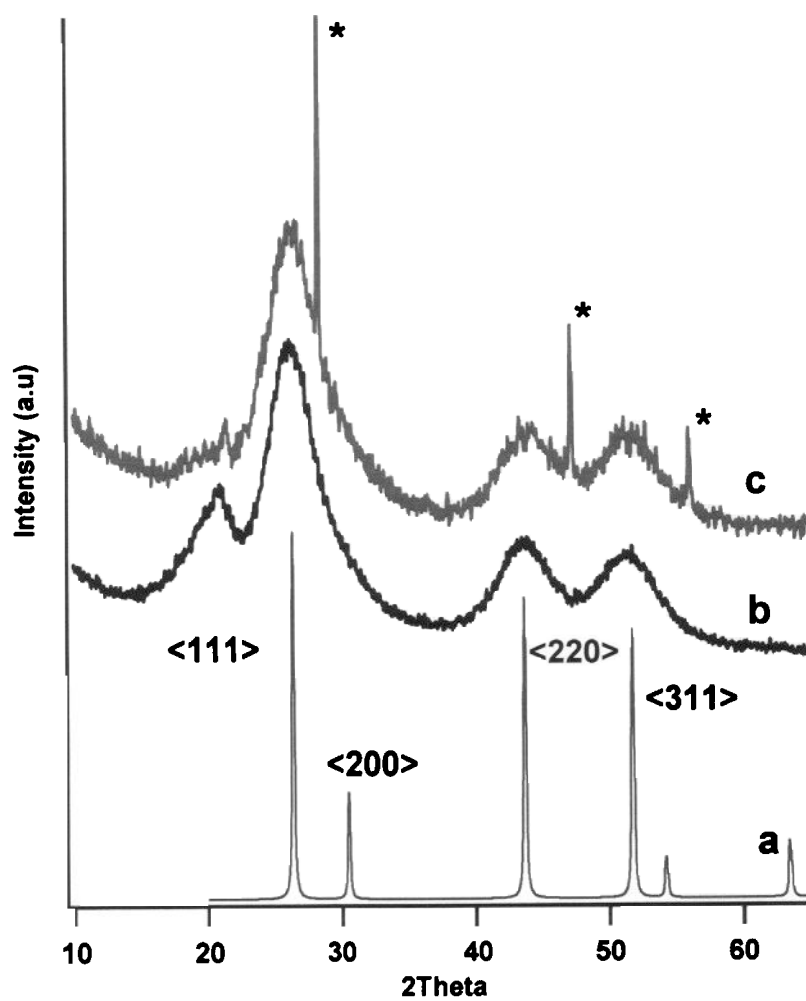


Figure 5.4b. XRD of pre and post etched InGaP.

5.4. Formation and etching of $\text{In}_{1-x}\text{Ga}_x\text{P}$

In this section, the formation characteristics by microwave methods and ambient photochemical HF etching of InGaP nanoparticles are examined as a function of Ga concentration. It was found that small concentrations of Ga in the nanoparticle drastically increase the rate of photochemical etching. Quantum efficiencies of 0.80 were achieved for nanoparticles containing $\text{In}_{0.970}\text{Ga}_{0.0297}\text{P}$. At present elemental analysis is being carried out on the calculated 9 and 16% Ga concentration, therefore they will be referred to as 9 and 16 % Ga in the text. Lower QY's were measure 0.40 and 0.50 for InP and 16 xx InGaP respectively.

As discussed in chapter 4 of this thesis and a recently publish manuscript³⁴, InGaP nanoparticles approach a size of approximately 4 nm after 1 minute reaction time at 280 °C. The size distribution is poor. As the reaction proceeds, the nanoparticles size distribution becomes focused at approximately 7 minutes. Figure 1 shows a series of $\text{In}_{1-x}\text{Ga}_x\text{P}$ with a reaction time of 5 minutes. It is apparent that there is a red shift in the onset of the first excitation as the mole percent of gallium increases. This could be due to a reaction with an acetylacetonate bi-product in the reaction mixture. Peng et al³⁵ noted that the indium to phosphorous ratio needed to be strictly 2 : 1. If the ratio deviated, the resulting reaction exhibited a poor colloidal size distribution. In this example, a side reaction of the phosphorous with a gallium-III-acetylacetonate which reduces the effective moles of phosphorous for the formation of the nanoparticles may cause this increased size distribution.

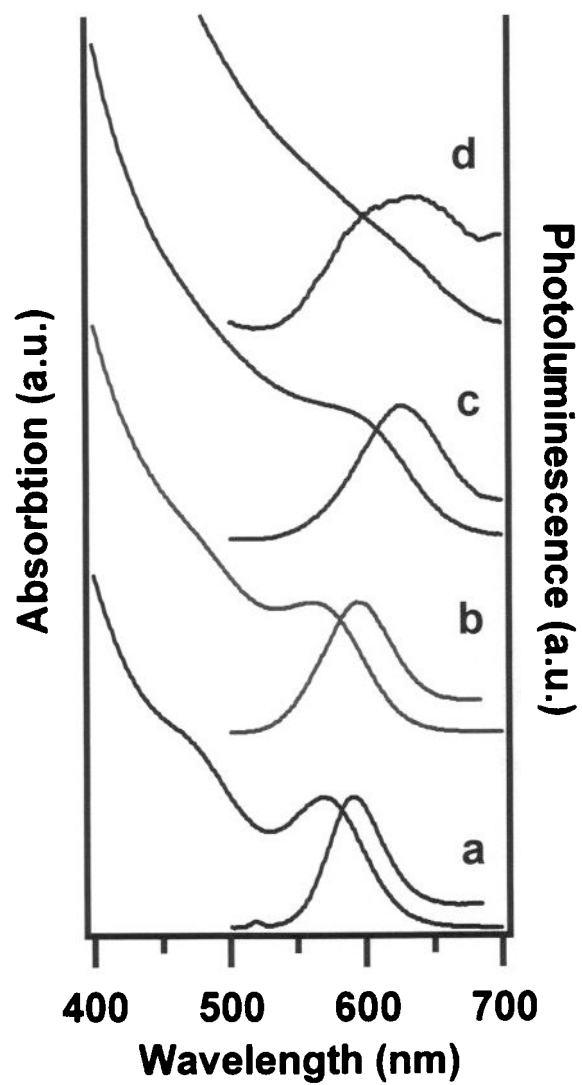


Figure 5.5. Room temperature absorption and fluorescence in toluene of as prepared InP (a), $\text{In}_{0.970}\text{Ga}_{0.0297}\text{P}$ (b), 9% Ga : $\text{In}_{x-1}\text{Ga}_x\text{P}$ (c), 16% Ga : $\text{In}_{x-1}\text{Ga}_x\text{P}$ (d).

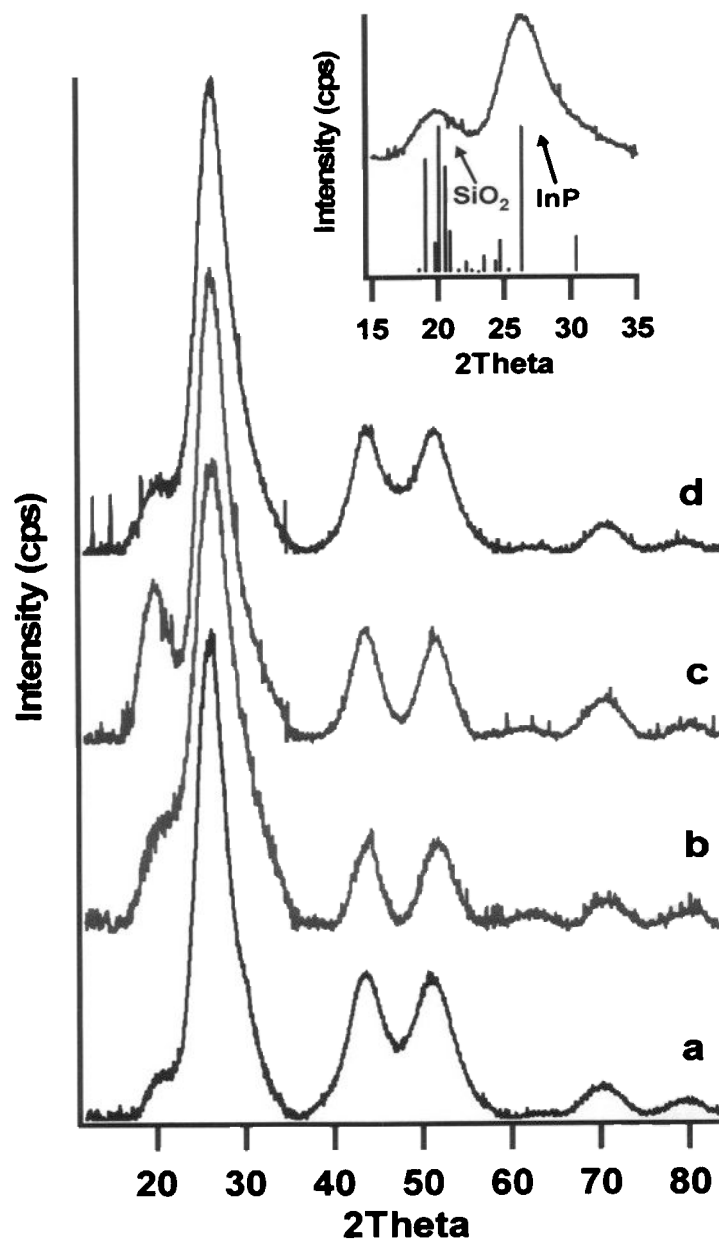


Figure 5.6. Powder X-ray diffraction of InP (a), $\text{In}_{0.970}\text{Ga}_{0.0297}\text{P}$ (b), 9% Ga : $\text{In}_{x-1}\text{Ga}_x\text{P}$ (c), 16% Ga : $\text{In}_{x-1}\text{Ga}_x\text{P}$ (d). The inset shows a magnified view of $\text{In}_{x-1}\text{Ga}_x\text{P}$ with the broadened reflection centered 20 2Theta which was identified as a side product of SiO_2 (PDF#01-089-1350).

The calculated mole percent gallium to indium for the reactions shown in figure 5.5 is as follows: 0% (a), 5% (b), 9% (c), 16% (d). The actual incorporation of the gallium into the nanoparticles to form the alloy is as follows: $\text{In}_{0.970}\text{Ga}_{0.0297}\text{P}$ (b), 9% Ga : $\text{In}_{x-1}\text{Ga}_x\text{P}$ (c), 16% Ga : $\text{In}_{x-1}\text{Ga}_x\text{P}$ (d).

Figure 5.6 shows powder X-Ray diffraction of InP, $\text{In}_{0.970}\text{Ga}_{0.0297}\text{P}$ (b), 9% Ga : $\text{In}_{x-1}\text{Ga}_x\text{P}$ (c), 16% Ga : $\text{In}_{x-1}\text{Ga}_x\text{P}$ (d). A bi-product of the reaction was identified as SiO_2 . At this time is not clear if the SiO_2 is in the form of nanoparticles or formed on the surface of the $\text{In}_{x-1}\text{Ga}_x\text{P}$. In either case, the SiO_2 gives rise to the broad reflection centered at $19.5^\circ 2\theta$. SiO_2 is the most likely species since Si is present by 3 moles excesses than phosphorous and a large amount of oxygen from the gallium (III) 2,4-pentanedionate is present in solution. The SiO_2 reflection is most apparent in the 9 and 16 % reactions. Upon HF etching, the reflection diminishes leaving the crystalline reflections of $\text{In}_{x-1}\text{Ga}_x\text{P}$ (figure 5.4b).

The SiO_2 bi-product originates from the nucleation stage of the nanoparticles. As nuclei form, trimethyl silanes are eliminated from the phosphorous to form the In-P bond. The displacement of a trimethylsilane presumably occurs with the elimination of a ligand from the indium leaving a silyl ester. As the reaction progresses, remaining acac in solution reacts with Si to form SiO_2 nanoparticles. This is evident in the XRD as the mole percent of gallium III acetylacetonate increases. The particles become increasingly difficult to isolate and purify to a powder from the mother solution.

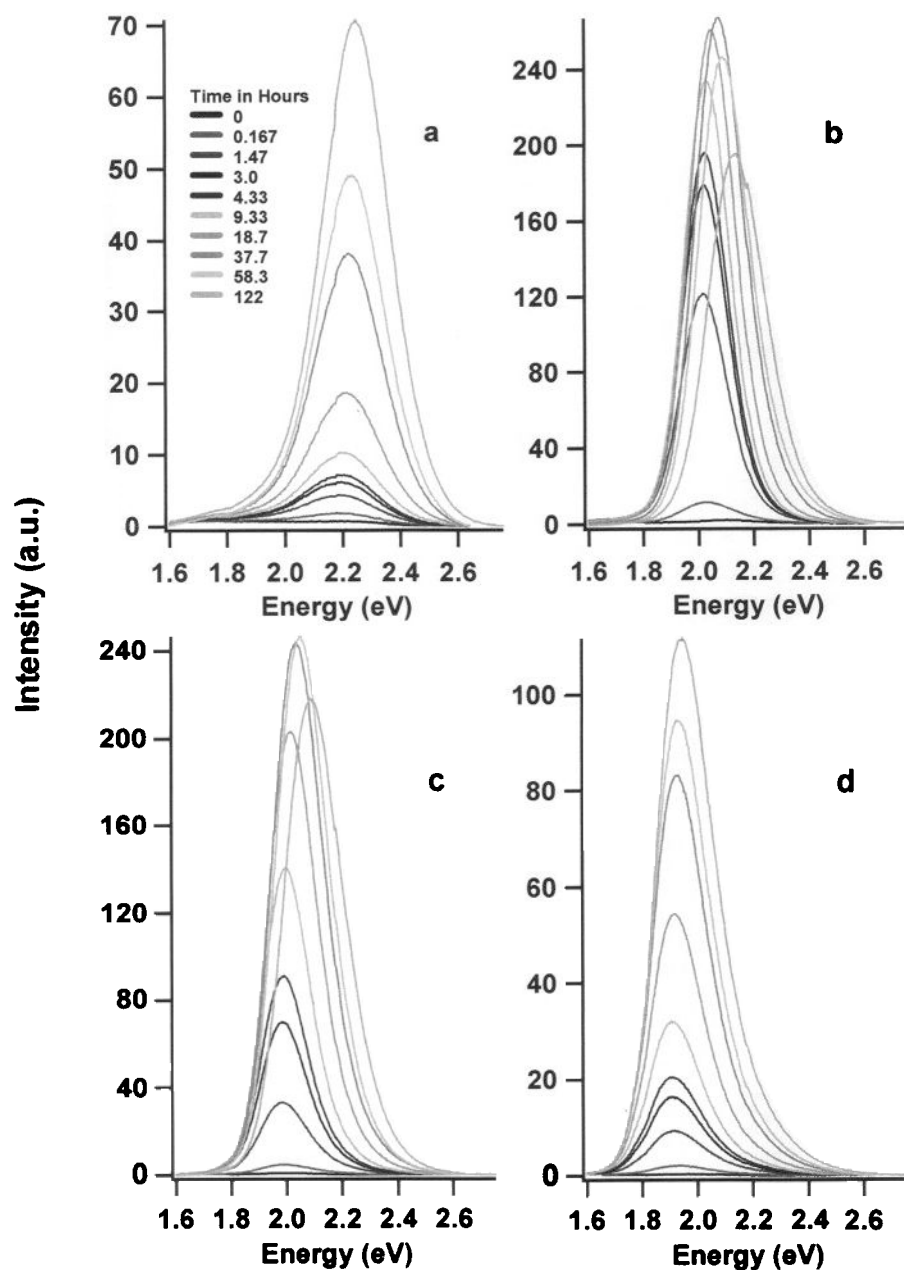


Figure 5.7. PL evolution of a series of InGaP nanoparticles in the presence of HF; InP (a), $\text{In}_{0.970}\text{Ga}_{0.0297}\text{P}$ (b), 9% Ga : $\text{In}_{x-1}\text{Ga}_x\text{P}$ (c), 16% Ga : $\text{In}_{x-1}\text{Ga}_x\text{P}$. The photochemical reaction were conducted in ambient lighting conditions and room temperature for 122 hours. The samples were left undisturbed other than incremental spectral acquisition during the 122 hours.

As mentioned earlier, the current synthetic procedures used to prepare nanoparticles of InP are lengthy and require long reaction times. In most reports, the as prepared nanoparticles do not exhibit band edge luminescence. Nozik et al. proposed that trap states occur in the as prepared nanoparticle due to P vacancies at the surface²⁴. Removal of the vacancies can be accomplished by photochemical etching with HF enhancing the band edge luminescence. Furthermore, Talapin et al.^{17, 26} observed a quantum efficiency of etched InP up to 40%. They attribute this to the removal of surface P with dangling bonds. Bulk etching studies invariably state that bulk InP readily oxidizes natively in air to produce InPO₄ on the indium rich faces and P₂O₅ on the phosphorous rich faces²⁷. These native oxide layers adopt octahedral unit cell crystal symmetries intimately reconstruct the cubic InP / octahedral oxide interface. This interface can introduce Schottky defects²⁷ and glide plane defects and a large as well as a large variation in the stoichiometry. Collectively these defect induced interfaces can cause radiative trap centers for quantum confined luminescent nanoparticles. Hence the historically poor luminescence efficiency of the III-V phosphide nanoparticle phosphors.

The quantum efficiency of the nanoparticles can be enhanced by the action of photochemical etching in the presence of dilute solution of HF. Photochemical etching of InP nanoparticles has been studied previously by Micic et al. They concluded that fluorine fills phosphorous vacancies whereby surface traps are passivated giving rise to enhanced band edge luminescence³⁶. Talapin et al. showed that InP nanoparticles can size selected under controlled photo etching conditions using

various fluorine sources¹⁷. The results of the photo chemical etching presented in this chapter is similar to previous reports for InP, however, the rate of the PL enhancement and QY are quite different when compared to $\text{In}_{x-1}\text{Ga}_x\text{P}$.

Briefly, the solutions of nanoparticles were prepared by a modification of literature methods^{17, 18}. The samples were isolated from the reaction mixture by precipitation with acetone/methanol and dispersion in toluene. This procedure was performed two times to ensure metallic bi-products were separated from the nanoparticles solution. The optical density of the solutions was adjusted to 0.09 at 480 nm (for QY standardization). Subsequently, 50 mg of hexadecanoic acid was mixed with 5 ml of nanoparticles/toluene solutions. Finally, 3 μL of 4.8 % HF/butanol was injected into each solution.

Prior to the injection of the HF solution, the PL spectra was recorded as time zero. Spectra were recorded at time intervals spanning several days. Figure 5.7 shows the PL evolution profiles of the samples. These nanoparticles were etched in ambient room light and temperature. It is shown that there is a more rapid increase in the PL in the initial four hours from time zero when InP is compared to $\text{In}_{x-1}\text{Ga}_x\text{P}$. It is also illustrated in figure 5.7 that as the PL profile increases in intensity it is accompanied with a red shift. This is most apparent in the $\text{In}_{0.970}\text{Ga}_{0.0297}\text{P}$.

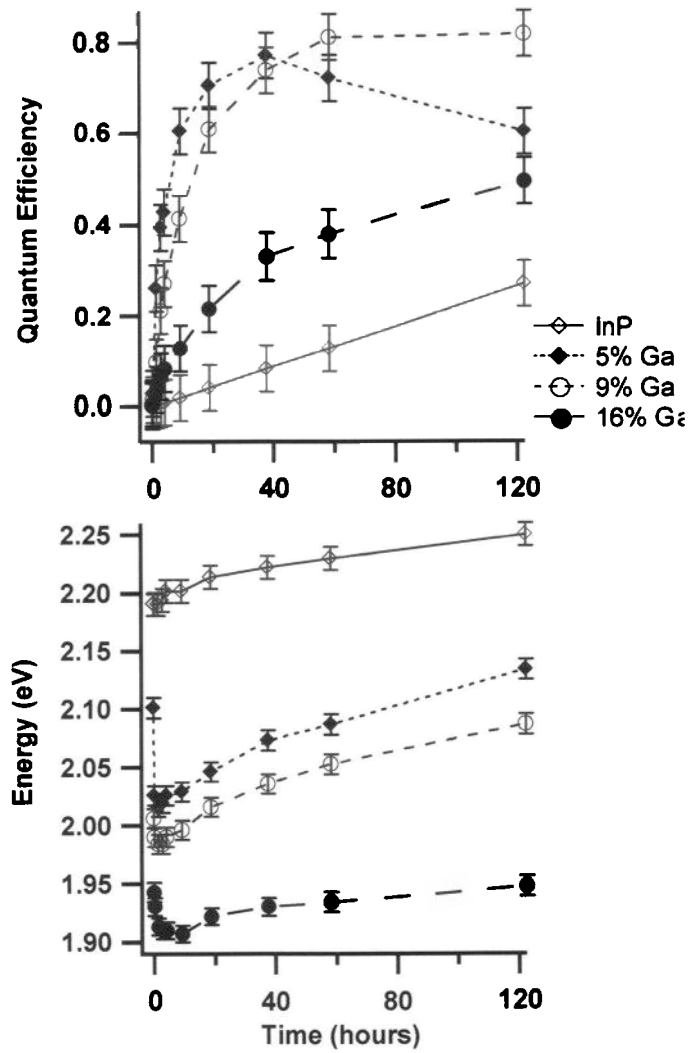


Figure 5.8. Quantum efficiency and PL red shift of $\text{In}_{x-1}\text{Ga}_x\text{P}$ as a function of photo chemical etching time. Each color trace represents InP (green), $\text{In}_{0.970}\text{Ga}_{0.0297}\text{P}$ (blue), 9% Ga : $\text{In}_{x-1}\text{Ga}_x\text{P}$ (red), 16 % Ga : $\text{In}_{x-1}\text{Ga}_x\text{P}$ (black).

The red shift is more clearly illustrated in figure 5.8 as the QY's of the samples are compared as a function of time. Within the first 20 hours, the 5 and 9 % samples show a dramatic increase in the QY in contrast to the 16 % sample and InP. Around 30 hours the 5 and 9 % samples approach a QE of 0.80. Surprisingly the 5 % sample QY drops rapidly after 30 hours. This can be explained by oxidation of the nanoparticles. InP is known to undergo oxidation easily. As noted above, reports have identified the native oxide of InP to consist of InPO_4 ^{27, 37, 38}. Most likely, the formation of InPO_4 creates nonradiative traps due to surface reconstruction resulting in a loss in the QY.

The observed red shift in $\text{In}_{x-1}\text{Ga}_x\text{P}$ is due to aggregation of the nanoparticles when the etching process is initiated and the subsequent blue shift is the dissolution of the aggregates over the course of the etching. The first excitonic peak position remains constant while the PL red shifts. This phenomenon has been observed for close packed films of the CdSe and InP nanoparticles. Kagan et al³⁹⁻⁴¹ ascribed the PL red shift in close packed films of CdSe to electronic energy transfer from nearest neighbor dipole-dipole interactions. Micic and co-workers^{36, 42} also observed PL red shift of close packed multilayer films of InP where the exciton remained constant during the PL red shift. When the CdSe or InP is re-dissolved, the PL blue shifted to its original position.

The preliminary TEM images (figure 5.4a) of the initial stages of the etching show a clustering of nanoparticles in between 5 and 6 nm aggregates. The red shift is most likely due to the nearest neighbor dipole-dipole interaction within the

aggregates. Work is in progress to verify that the blue shift is accompanied with dissolution of the aggregates. The most dramatic red shift is seen in the $\text{In}_{0.970}\text{Ga}_{0.0297}\text{P}$ nanoparticles. This may be due to the accelerated rate of etching that Ga plays at the surface of the nanoparticles.

5.5 Conclusion

In conclusion, it was shown that the microwave drive formation of InGaP is efficient and simply by manipulating the degree of coordination by tertiary Lewis bases, various sizes of quantum dots can be isolated. Photochemical etching with HF can greatly enhance the quantum yield of InGaP from 0.04 up to 0.80, the highest reported for a III-V phosphor to date. The efficiency and rate of photo chemical etching of InP can be enhance by the addition of small amount of Ga to the reaction. The Ga precursor has a negative effect on the reaction if it is present greater than 10 % by mole ratio to In. The resulting chemically etched nanoparticles have a significantly high QY of 0.80 in ambient light.

5.6 References

1. D'Andrade, B. W.; Forrest, S. R., *Advanced Materials* **2004**, 16, (18), 1585-1595.
2. Shibayama, K.; Hiraki, M.; Saitou, Y.; Hosono, A., *Japanese Journal of Applied Physics Part 1-Regular Papers Short Notes & Review Papers* **2003**, 42, (6A), 3698-3701.
3. Alivisatos, P., *Nature Biotechnology* **2004**, 22, (1), 47-52.

4. Parak, W. J.; Gerion, D.; Pellegrino, T.; Zanchet, D.; Micheel, C.; Williams, S. C.; Boudreau, R.; Le Gros, M. A.; Larabell, C. A.; Alivisatos, A. P., *Nanotechnology* **2003**, 14, (7), R15-R27.
5. Tomaselli, M.; Yarger, J. L.; Bruchez, M.; Havlin, R. H.; deGraw, D.; Pines, A.; Alivisatos, A. P., *Journal of Chemical Physics* **1999**, 110, (18), 8861-8864.
6. Sonnichsen, C.; Alivisatos, A. P., *Nano Letters* **2005**, 5, (2), 301-304.
7. Hikmet, R. A. M.; Chin, P. T. K.; Talapin, D. V.; Weller, H., *Advanced Materials* **2005**, 17, (11), 1436-+.
8. Hu, J. T.; Li, L. S.; Yang, W. D.; Manna, L.; Wang, L. W.; Alivisatos, A. P., *Science* **2001**, 292, (5524), 2060-2063.
9. Bowers, C. R.; Pietrass, T.; Barash, E.; Pines, A.; Grubbs, R. K.; Alivisatos, A. P., *Journal of Physical Chemistry* **1994**, 98, (38), 9400-9404.
10. Zimmer, J. P.; Kim, S. W.; Bawendi, M. G., *Abstracts of Papers of the American Chemical Society* **2005**, 229, U1082-U1082.
11. Fu, H. X.; Zunger, A., *Physical Review B* **1997**, 56, (3), 1496-1508.
12. Michalet, X.; Pinaud, F.; Lacoste, T. D.; Dahan, M.; Bruchez, M. P.; Alivisatos, A. P.; Weiss, S., *Single Molecules* **2001**, 2, (4), 261-276.
13. Peng, P.; Milliron, D. J.; Hughes, S. M.; Johnson, J. C.; Alivisatos, A. P.; Saykally, R. J., *Nano Letters* **2005**, 5, (9), 1809-1813.
14. Bakkers, E.; Hens, Z.; Kouwenhoven, L. P.; Gurevich, L.; Vanmaekelbergh, D., *Nanotechnology* **2002**, 13, (3), 258-262.

15. Huynh, W. U.; Dittmer, J. J.; Libby, W. C.; Whiting, G. L.; Alivisatos, A. P., *Advanced Functional Materials* **2003**, 13, (1), 73-79.
16. Huynh, W. U.; Dittmer, J. J.; Alivisatos, A. P., *Science* **2002**, 295, (5564), 2425-2427.
17. Talapin, D. V.; Gaponik, N.; Borchert, H.; Rogach, A. L.; Haase, M.; Weller, H., *Journal of Physical Chemistry B* **2002**, 106, (49), 12659-12663.
18. Micic, O. I.; Sprague, J.; Lu, Z. H.; Nozik, A. J., *Applied Physics Letters* **1996**, 68, (22), 3150-3152.
19. Muthuvel, M.; Stickney, J., *Journal of the Electrochemical Society* **2006**, 153, (1), C67-C73.
20. Adachi, S., *Materials Science and Engineering B-Solid State Materials for Advanced Technology* **2006**, 126, (1), 49-52.
21. van Vugt, L. K.; Veen, S. J.; Bakkers, E.; Roest, A. L.; Vanmaekelbergh, D., *Journal of the American Chemical Society* **2005**, 127, (35), 12357-12362.
22. Adam, S.; Talapin, D. V.; Borchert, H.; Lobo, A.; McGinley, C.; de Castro, A. R. B.; Haase, M.; Weller, H.; Moller, T., *Journal of Chemical Physics* **2005**, 123, (8).
23. Blackburn, J. L.; Ellingson, R. J.; Micic, O. I.; Nozik, A. J., *Journal of Physical Chemistry B* **2003**, 107, (1), 102-109.
24. Micic, O. I.; Nozik, A. J.; Lifshitz, E.; Rajh, T.; Poluektov, O. G.; Thurnauer, M. C., *Journal of Physical Chemistry B* **2002**, 106, (17), 4390-4395.

25. Borchert, H.; Talapin, D. V.; Gaponik, N.; McGinley, C.; Adam, S.; Lobo, A.; Moller, T.; Weller, H., *Journal of Physical Chemistry B* **2003**, 107, (36), 9662-9668.
26. Adam, S.; McGinley, C.; Moller, T.; Talapin, D. V.; Borchert, H.; Haase, M.; Weller, H., *European Physical Journal D* **2003**, 24, (1-3), 373-376.
27. Hashizume, T.; Saitoh, T., *Applied Physics Letters* **2001**, 78, (16), 2318-2320.
28. Kikuchi, D.; Adachi, S., *Materials Science and Engineering B-Solid State Materials for Advanced Technology* **2000**, 76, (2), 133-138.
29. Ishikawa, H.; Kobayashi, S.; Koide, Y.; Yamasaki, S.; Nagai, S.; Umezaki, J.; Koike, M.; Murakami, M., *Journal of Applied Physics* **1997**, 81, (3), 1315-1322.
30. Erne, B. H.; Vanmaekelbergh, D., *Journal of the Electrochemical Society* **1997**, 144, (10), 3385-3392.
31. Preusser, S.; Herlem, M.; Etcheberry, A.; Jaume, J., *Electrochimica Acta* **1992**, 37, (2), 289-295.
32. Paul, T. K.; Bose, D. N., *Journal of Applied Physics* **1991**, 70, (12), 7387-7391.
33. Hollinger, G.; Bergignat, E.; Joseph, J.; Robach, Y., *Journal of Vacuum Science & Technology a-Vacuum Surfaces and Films* **1985**, 3, (6), 2082-2088.
34. Gerbec, J. A.; Magana, D.; Washington, A.; Strouse, G. F., *Journal of the American Chemical Society* **2005**, 127, (45), 15791-15800.
35. Battaglia, D. M.; Li, J. J.; Peng, X. G., *Abstracts of Papers of the American Chemical Society* **2003**, 225, U44-U44.

36. Micic, O. I.; Ahrenkiel, S. P.; Nozik, A. J., *Applied Physics Letters* **2001**, *78*, (25), 4022-4024.

Liu, X.; Andrews, J. W.; Irene, E. A., *Journal of the Electrochemical Society* **1991**, *138*, (4), 1106-1111.
38. Gu, G.; Li, H. J.; Ogryzlo, E., *Journal of the Chemical Society-Faraday Transactions* **1995**, *91*, (18), 3021-3026.

Leatherdale, C. A.; Kagan, C. R.; Morgan, N. Y.; Empedocles, S. A.; Kastner, M. A.; Bawendi, M. G., *Physical Review B* **2000**, *62*, (4), 2669-2680.
40. Kagan, C. R.; Leatherdale, C. A.; Kastner, M. A.; Bawendi, M. G., *Abstracts of Papers of the American Chemical Society* **1997**, *213*, 320-PHYS.
41. Kagan, C. R.; Murray, C. B.; Nirmal, M.; Bawendi, M. G., *Physical Review Letters* **1996**, *76*, (9), 1517-1520.
42. Beard, M. C.; Turner, G. M.; Murphy, J. E.; Micic, O. I.; Hanna, M. C.; Nozik, A. J.; Schmittenmaer, C. A., *Nano Letters* **2003**, *3*, (12), 1695-1699.

Chapter 6. III-V core/shell heterostructures

6.1 Introduction

The PLQY for nanocrystals prepared by colloidal methods is often low due to poor passivation, internal glide plane defects, and the presence of vacancies which give rise to recombination donor and acceptor sites in the gap¹. This behavior is worse for small nanomaterials (< 4 nm) where the large ratio of surface atoms to bulk material leads to rapid nonradiative recombination at surface defects and vacancies that effectively compete with luminescence². This is particularly true for InP QD's where P vacancies have been implicated in the poor QY performance³ of these materials where typical QYs on the order of 1- 4% are observed for organically passivated InP cores.

In order to improve the stability of InP, a deeper level of understanding of the nature of the recombination centers arising from vacancy defects is needed. The trap centers in InP are associated with mid-gap donor levels arising from P vacancies at the surface following a 1×1 reconstruction of the $\langle 001 \rangle$ face⁴⁻⁸. The P vacancies can be removed by treatment with fluoride ion, effectively replacing the vacant P site. In fact, Talapin, et al⁹ and Nozik, et al¹⁰⁻¹² demonstrated chemical etching of InP (ref) can increase the PLQY up to 0.014, discussed in chapter 5 in detail. Treatment under UV photolysis has demonstrated the process is an activated etching process in analogy to wet-chemical etching of InP wafers. Unfortunately, the fluoride ion is unstable to dissociation, which leads to re-oxidation of the nanomaterial surface. The

Chapter 6. III-V core/shell heterostructures

6.1 Introduction

The PLQY for nanocrystals prepared by colloidal methods is often low due to poor passivation, internal glide plane defects, and the presence of vacancies which give rise to recombination donor and acceptor sites in the gap¹. This behavior is worse for small nanomaterials (< 4 nm) where the large ratio of surface atoms to bulk material leads to rapid nonradiative recombination at surface defects and vacancies that effectively compete with luminescence². This is particularly true for InP QD's where P vacancies have been implicated in the poor QY performance³ of these materials where typical QYs on the order of 1- 4% are observed for organically passivated InP cores.

In order to improve the stability of InP, a deeper level of understanding of the nature of the recombination centers arising from vacancy defects is needed. The trap centers in InP are associated with mid-gap donor levels arising from P vacancies at the surface following a 1x1 reconstruction of the <001> face⁴⁻⁸. The P vacancies can be removed by treatment with fluoride ion, effectively replacing the vacant P site. In fact, Talapin, et al⁹ and Nozik, et al¹⁰⁻¹² demonstrated chemical etching of InP (ref) can increase the PLQY up to 0.014, discussed in chapter 5 in detail. Treatment under UV photolysis has demonstrated the process is an activated etching process in analogy to wet-chemical etching of InP wafers. Unfortunately, the fluoride ion is unstable to dissociation, which leads to re-oxidation of the nanomaterial surface. The

liability of the fluoride ion at the InP solution interface therefore only leads to increased PLQY for a short period with rapid re-oxidation leading the QY loss. Chemical etching does not appear to protect the crystalline core from native oxidation. Hence the PLQY of chemically etched InP decays in time as the native oxidation penetrates toward the core of the crystallite. It has been established in the bulk literature for InP <001> that the surface readily oxidizes with the formation of InPO_4 ¹³⁻¹⁷ and In_2O_3 ^{4, 13-18} surfaces that have a native oxide thickness on the order of 3 nm⁸. This is detrimental to phosphide nanoparticles when considering the native oxide thickness of InP at 3 nm is equivalent to the radius of the larger nanoparticles that can be prepared. Inhibiting the formation of a thermodynamically stable oxide is a critical step in establishing a device quality III-V quantum dot with high PLQY.

To increase the efficiency of luminescence of these materials, vacancy defects need to be reduced, and the wave function of the electron-hole pair must be confined by increasing the potential energy barriers at the nanocrystal surface. Decreasing vacancy defects is achievable by use of MW chemistry coupled with etching of the surface, as outlined previously. To increase the confinement potential the most effective means is shelling the surface with a high bandgap semiconductor where minimal lattice mismatch occurs¹⁹. Lattice mismatch requires reconstruction of the crystallite faces which may lead to sub gap donor and acceptor levels in that the interface, and thus recombination centers. In CdSe, the quintessential nanomaterial, it has been observed that core shell capping leads to a vast improvement in the optical performance²⁰⁻²⁴.

Strategies involving chemical modification of the quantum dot surface and epitaxial growth of a wider band gap material around each core quantum dot forming a core-shell structure have been previously demonstrated to increase the room temperature PLQY. In fact several examples exist in the literature, most notably CdSe/ZnS²¹, CdSe/ZnSe, CdSe/CdS²⁵, HgTe/CdS²⁶. These are effective strategies at increasing the PLQY and in the latter case an effective inhibition of oxidation of the crystalline core. The ease of epitaxial growth of the II-VI core/shell structures does not translate to the III-V core/shell heterostructures. ZnCdSe²⁷ and ZnS²⁸⁻³⁰ are the only successful reports of core shell structures on InP. Nozic et al. has demonstrated InP/ZnCdSe₂ heterostructure in which they propose the shell material alloys into the InP core particle²⁷. In either case, the surface must undergo a reconstruction to accommodate the lattice mismatch and in the III-V/II-V case, a charge balance.

To date, the literature has not shown an effective epitaxial shelling technique for the InP quantum dots. In general, the following shelling is the highest reported QY on InP 0.14. This is an improvement of the PLQY of the out of batch nanoparticles but is not high enough to be useful in SSL applications (> 40%), which are typically reported to be less than 0.01. In general, the crystalline structure or more specifically the interface of the core and shell materials has not been investigated. From TEM, the shells are incomplete and in some cases reveal quantum dots that have formed from the shelling precursor reducing the reactive monomers required for shell formation^{19, 27, 31}. No follow up reports for heterostructure of InP have occurred most likely to the great difficulty of the particle

growth and the innate chemical instability of the phosphide nanoparticles. The following sections will outline results of core shell structures on InGaP and InP with several shell compositions.

6.2 Synthesis of Core/Shell Nanoparticle Heterostructures

Synthesis of nanoparticles and nanoparticle core/shell structures have many variables associated with it. This is easily recognized when one considers the mechanism of crystal formation, possible alternative morphologies, the thermodynamics of reaction, and the competition of kinetically trapped structures during nanomaterial growth. In bulk crystallization processes, nucleation must occur by formation of a minimal cluster size composed of a discrete number of ions. The growth at this point is controlled by thermodynamics via the rate of addition and stabilization of energy (surface energy vs crystal energy), as well as concentration of the elements in solution. While in bulk materials this is largely thermodynamic control, in a nanomaterial often the reaction is under kinetic control which results in vacancies and self-terminating growth trajectories. Further considerations in nanomaterial growth include, cation:anion mol ratio, total ion concentration, ligand chain length and head group and shell reactant injection temperature. Likewise, for core/shell structures we not only worry about lattice matching and lattice mismatch in ion size, we worry about the variables induced by simultaneous injection versus alternating cation/anion injection, concentration of shell precursor, basicity of the coordinating solvent and injection temperature.

Considerations for the core-shell heterostructure material are the band gap of the overlayer material and the lattice mismatch with the host or core particle. Table 1 outlines some possible heterostructures for InP quantum dots. The shell material should have a wider band gap than that of the core and similar lattice constants. ZnS for example can exist in the zinc blende structure with a lattice mismatch of 7.68% where as CdS has a lattice mismatch of 0.68%. For commercial applications, however Cd based materials are not considered viable candidates due to the environmental toxicity of the ion. ZnS on the other hand has a similar lattice constant with a band gap of 3.68 eV.

Core-Shell Structure	Lattice Mismatch (%)	Shell Eg (eV)
InP- ZnS	7.68	3.68
InP-ZnSe	3.24	2.82
InP-ZnTe	3.93	2.39
InP-CdS	0.683	2.50
InP-GaN	23.2	3.23

Table 6.1 Lattice mismatch and band gaps of semiconductor shell material on InP.

Figure 6.1 illustrates the competitive pathways that can occur during epitaxial quantum dot heterostructure formation in solution. The chemical route to achieve the growth of the shell material onto the nanocrystal core is high temperature injection of volatile shell precursors to achieve the core particle surface reconstruction and

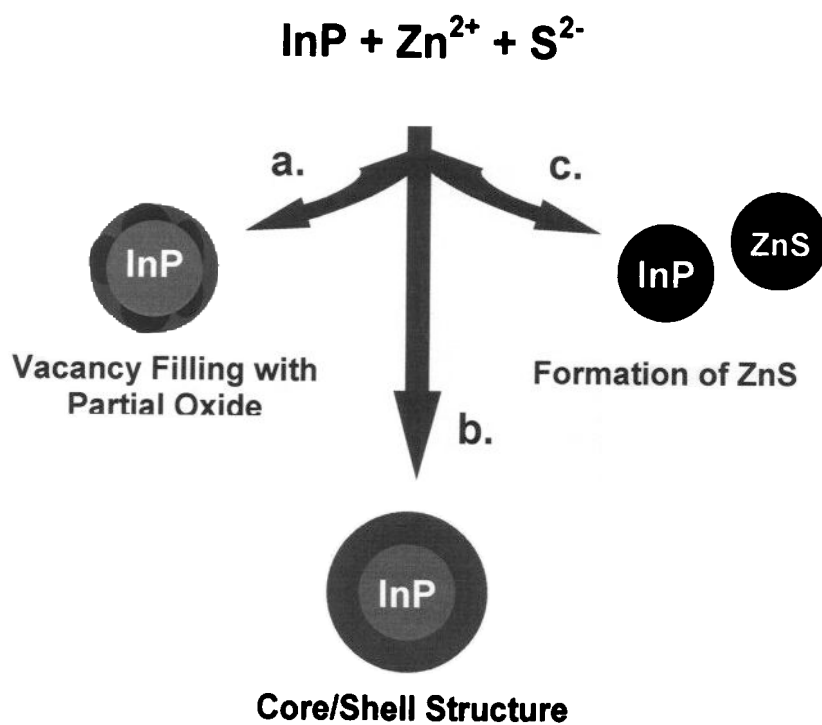


Figure 6.2. Illustration showing the competitive pathways for the formation of core-shell quantum dot heterostructures by solution based chemical methods.

ultimately the growth of the shell to a desired thickness. The processes are considerably complex when one examines the variables associated with a typical reaction trajectory. For the formation of well defined heterostructures follows path b in Figure 6.1. Factors to consider for solution phase epitaxial growth are nanoparticle concentration, temperature, basicity of the coordinating solvent, injection speed of the shell precursors and lastly the concentration of the shell precursors. If the temperature is too low the probability of nucleating ZnS nanoparticles is likely (path c. in Figure 6.1). In addition, if the concentration of the shell precursors is too high, injected too fast or the concentration of the core nanoparticles is too low, then path c is preferred.

In this section of the thesis, we explore shelling behavior on microwave grown (low vacancy materials) core InP nanocrystals by ZnS, GaN and GaP. Shelling with the II-VI ZnS material results in a PLQY of 0.40, a substantial improvement over previously reported results by Weller et al²⁹. Disappointingly, the introduction of the III-V precursors had an inverse effect from shelling. The core nanoparticles were dissolved leaving a clear/colorless solution. The ternary phase of the core nanoparticles seems to make a “softer” material.

6.3 Experimental Methods

6.3.1 Introduction.

Solution phase epitaxial shell formation was carried out on binary and ternary III-V core nanoparticles with ZnS and attempted with GaP and GaN. The core particles were synthesized, isolated and purified prior to the shell growth. The shell growth was performed by two methods. One method utilizes layer by layer growth simply by performing alternating injections of anion and cation shelling reactants. The other method is a slow formation by simultaneous injection of the cation/anion shelling reactants.

6.3.2 Preparation of InGaP/ZnS.

The preparation of InGaP/ZnS was carried out by alternating reactant injections and simultaneous injections. Shelling was performed on as prepared material and surface modified material where the growth phase surfactant was stripped with pyridine prior to the shell formation.

InGaP core nanocrystal preparation. The preparation of the core particles are based on a modification of literature methods^{32, 33}. The In and Ga intermediates were prepared by mixing 2.71 mmol indium (III) acetate and 0.271 mmol of gallium (III) 2,4-pentanedionate and 8.94 mmol hexadecanoic acid with 190 ml of octadecene (ODE) in a three neck flask. The cation intermediates were formed by heating the solution to 110 °C under vacuum for two hours with four cycles of Ar backfilling. The temperature of the solution was allowed to cool to 50 °C at which time 1.50 mmol of tris(trimethylsilyl)phosphine was injected (TMSP). The In/Ga/P precursor solution immediately turned from colorless to yellow. The In/Ga/P precursor solution

was kept under Ar at 50 °C as a stock solution for later use. For a typical reaction, 5 ml of the stock solution was removed by Teflon syringe and placed in a reaction tube. The microwave power applied during the ramp period was set to 300 W to reach the reaction temperature in the least amount of time. Once the desired reaction temperature was reached, active cooling (~ 3 – 7 psi compressed air) was employed to stabilize the reaction temperature at an applied power of 280 W. Once the reaction was complete the power was reduced to 0 W and the compressed air flow was increased to 70 psi for maximum cooling. This minimizes Ostwald ripening processes.

The isolation and purification of the nanomaterials is achieved under an Ar atmosphere by dissolution of the room temperature reaction mixture in a minimum of toluene, addition of a 2:1 anhydrous butanol / methanol solution to induce particle precipitation, and collection of the solid via centrifugation. The process is repeated 3 times to remove unwanted reactants.

Ligand exchange. Intermediate steps that involved pyridine, a series of ligand exchange steps were carried out. Recapping involved placing 10 mg of purified InGaP in a reaction tube with 1ml of dry pyridine and heating in the microwave to 80°C for 15 minutes. The material was precipitated with dry hexane and the supernatant was removed under Schlenk techniques. 1ml of pyridine was placed in the reaction tube and this process was repeated 3 times or until the material could be solubilized by pyridine at room temperature.

InGaP/ZnS by Simultaneous Injection. Core shell composites prepared by simultaneous injection (injection of an equal mole mixture of Zn and S precursors) were carried out by massing 8.7g HDA and 50mg purified InGaP quantum dots into a three neck flask. The mixture was heated to 100°C and degassed for one hour with three cycles of Ar backfilling. The temperature of the mixture was raised to 250°C. At this temperature, 2ml of a 0.5M solution of Me₂Zn and bis(trimethylsilyl)sulfide ((TMS)₂S) in tri-n-octylphosphine was injected dropwise. The evolution of the PL was monitored by removing aliquots from the reaction mixture during the addition of the shelling reactants.

InGaP/ZnS by alternating cation-anion Injection. Core-shell composites prepared by alternate injections (separate injections of Zn and S) of cations and anions were done in the same way except that 0.5M solutions of Me₂Zn and (TMS)₂S were prepared separately in tri-n-octylphosphine. The initiation of the epitaxial growth of ZnS was performed at 250°C by injecting 0.3ml of the (TMS)₂S solution dropwise followed by 0.3ml of the Me₂Zn solution. The S and Zn injections were repeated until the red shift in the first exciton stabilized and no further shift was observed.

6.3.3 Preparation of InGaP/GaP and InGaP/GaN

Shelling on InGaP by III-Vs. The preparation and purification of the core InGaP quantum dots is the same as described in the previous example for the InGaP/ZnS heterostructures. The reaction mixture of the InGaP was prepared in

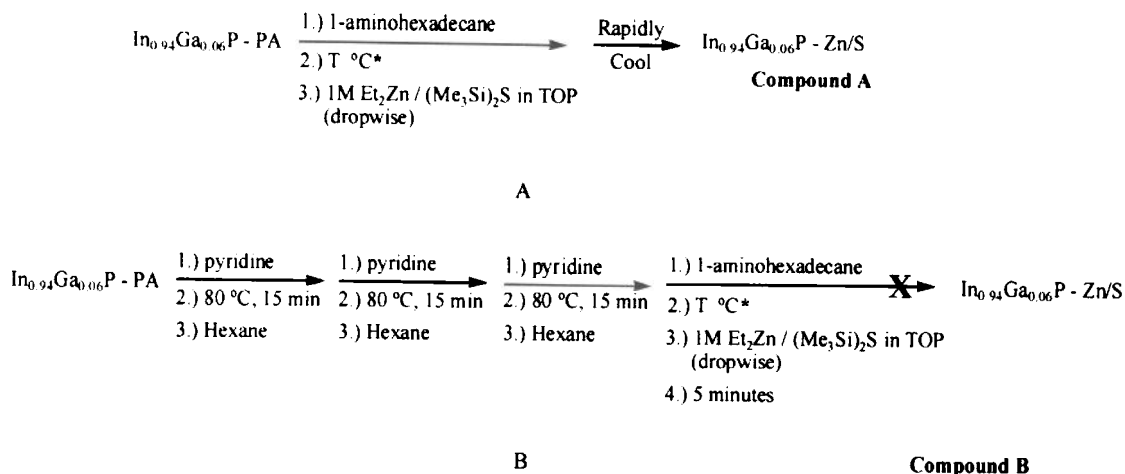
HDA in the same manner as the previous example. A 0.5M solution of GaCl_3 in tri-n-octylphosphine was prepared. A 0.5M solution of $(\text{TMS})_3\text{P}$ in dry hexadecane. Lastly, a 0.5M solution of nonamethyltrisilazane (NMTS) was prepared in dry hexadecane.

The shelling reaction was initiated at 260°C with the slow dropwise injection of 0.5ml of the anion solution followed by the injection of 0.5ml of the cation solution. This injection sequence was repeated three times after which the reaction was rapidly cooled.

6.3.4 Preparation of InP/ZnS

Preparation of InP/ZnS was conducted by simultaneous injections of Zn and S reactants to a hot solution of InP in dodecylamine. The InP quantum dots were prepared in the same manner as InGaP prepared in octadecene, keeping the cation:anion mol ratio 2:1 and the cation:ligand mol ratio at 1:3, and maintained at 50°C under Ar. 5.0ml of the InP stock solution was injected into the microwave reaction tubes prior to each reaction. The isolation and purification of the as prepared InP proceeds in the same manner as described in the InGaP/ZnS heterostructure example.

The core particles were prepared for shelling by massing 10g of dodecylamine and 10mg of InP quantum dots passivated with hexadecanoic acid into a three neck flask. The mixture was heated to 80°C and degassed for 1hr with three



*T °C indicates the reaction was performed at 150, 200, 250 °C

Scheme 6.1. Reaction schemes for ZnS shelling process at 150, 200, and 250°C with palmitic acid capped and pyridine capped material.

cycles of Ar backfilling. The temperature of the mixture was quickly raised to 250°C. At this time 7ml of a 0.05M solution of Me₂Zn and (TMS)₂S in tri-n-butylphosphine was slowly added by dropwise injection. The reaction solution was then quickly cooled to room temperature.

6.4 InGaP/ZnS Heterostructures

In an attempt to optimize the temperature at which shell formation takes place, alternating injections of Zn and S were performed at 150, 200 and 250°C. Two differently capped InGaP nanoparticles prepared by MW techniques were used in the following shelling process: one sample was left with the hexadecanoic acid mixture;

and the other was ligand exchanged with pyridine to remove hexadecanoic acid by dissolution in pyridine.

Hexadecanoic acid capped and pyridine capped InGaP nanoparticles were placed in reaction vials under Ar, inserted into the parallel plate reactor, and diluted with 10 ml of 1-aminohexadecane. The temperature of the reactor plate was raised to 150°C and 2 ml of the ZnS solution dissolved in TOP was added dropwise. The vials were removed from the plate after the injection was complete and allowed to cool to RT under Ar. The plate temperature was then increased to 200°C and another ZnS injection was done in the palmitic acid and pyridine capped material. Lastly, the plate temperature was raised to 250°C and the final ZnS injection was done and the vials removed from the plate and allowed to cool.

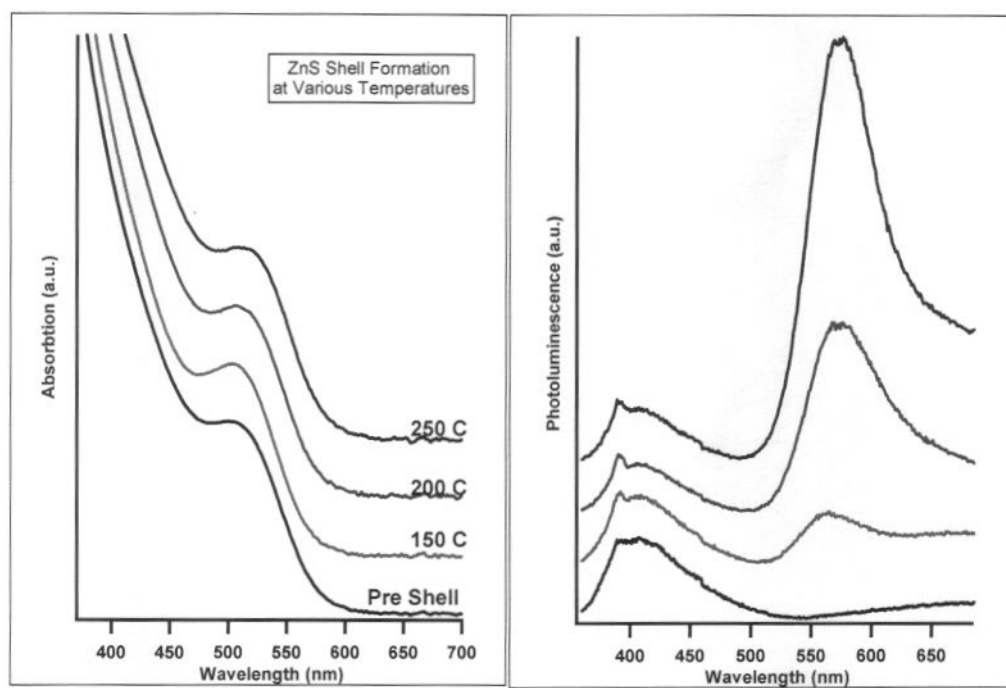


Figure 6.2. Room temperature absorption and photoluminescence of InGaP-PA in toluene at 150, 200, and 250 °C ZnS shelling temperatures.

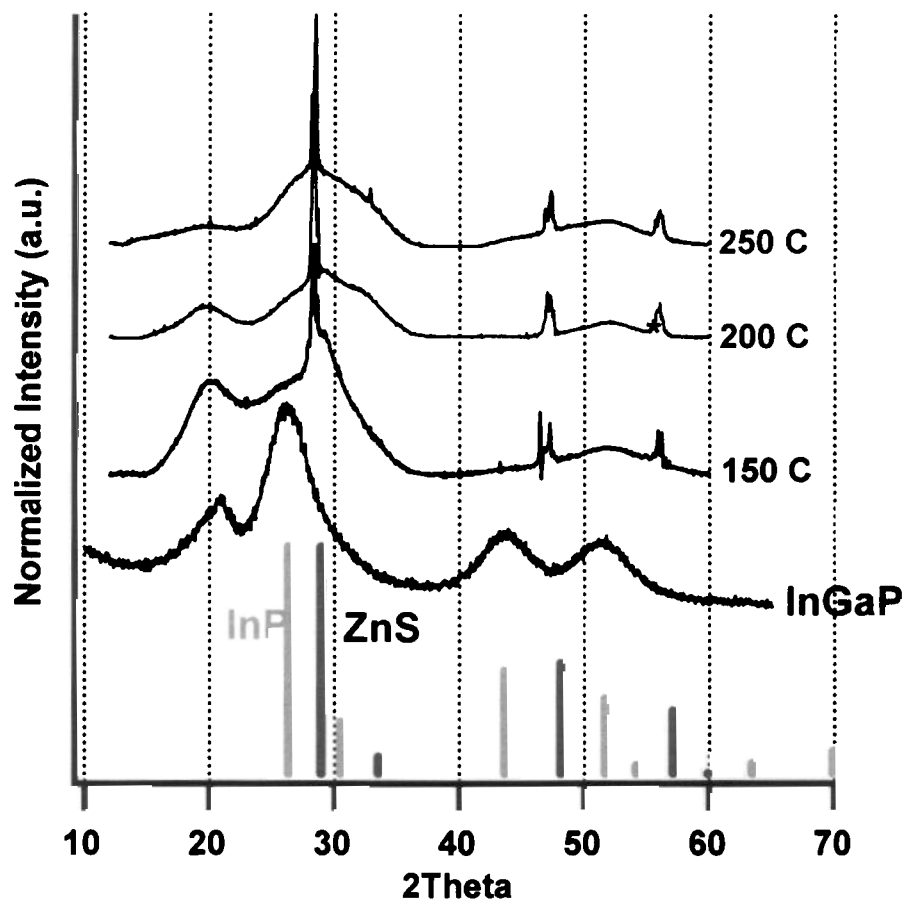


Figure 6.3. pXRD of InGaP/ZnS at various shelling temperatures from palmitic acid capped core nanomaterial.

The first injection of the Zn and S precursors to the acid capped material increased the band edge PL solution QE to 0.05 from 0.01. The 200°C injection yielded a solution QY of 0.05 and the final injection yielded a 0.10 QY. The colloidal stability was not improved over previously reported material most likely due to vacancy filling only. It is shown that the PL increases from 150 to 250°C. This can be described by a more discrete InP – ZnS material interface. Reconstruction of the InP surface is more favorable at higher temperatures. Thus, the intensity of the PL band increases. The broad band centered at 400nm is most likely Zn and In coordination compound bi-products that remain in solution during the purification steps.

The pXRD for the composite material is shown in figure 6.3. For each of the injection temperatures a discrete reflection of the $\langle 111 \rangle$ reflection of InGaP and ZnS is observed. As the injection temperature increases, the $\langle 111 \rangle$ reflections become broad and indistinguishable. This is likely a result of phase segregation. In other words, minimum shelling has occurred on InP to allow substantial ZnS to form, broadening all reflections of the two materials. The 150°C injection displays the most intense reflection of the ZnS $\langle 111 \rangle$. With increasing injection temperature an increase in the intensity of the $\langle 111 \rangle$ InP is observed relative to ZnS. Based on the data it appears that elevating the reaction temperature of the reaction enhances formation of the ZnS shell. At the lowest reaction temperature it is likely that ZnS nanoparticles are formed preferentially. Elevated reaction temperatures appear to favor epitaxial growth of ZnS onto the preformed InGaP nanocrystal.

Surprisingly, the pyridine capped core material responded dramatically different to the ZnS shelling process. There was no discernable increase in the PLQY. Figure 6.5 shows the resulting optical absorbance and photoluminescence of the post shelling procedure. There was a blue shift in the exciton of InGaP with increasing injection temperatures. The PL shows a significant broad band at 400nm which indicates significant cation bi-products. In addition, the materials was prone to precipitation, so the optical characterization was performed immediately after the shelling procedure. This behavior is similar to the III-V shelling process which will be addressed in the forthcoming section.

The InGaP-py solutions turned from a clear solution to an insoluble yellow powder when cooled to room temperature. The pXRD (figure 6.6) of the yellow powder does not reveal any definitive InGaP or ZnS reflections respectively. The closest match to this powder is a ZnInS alloy with possibly small amounts of elemental sulfur. The two major reflections centered at $2\theta = 23$ could be 1-aminohexadecane, but other alloy phases of Zn and In can't be ruled out and are presently being investigated.

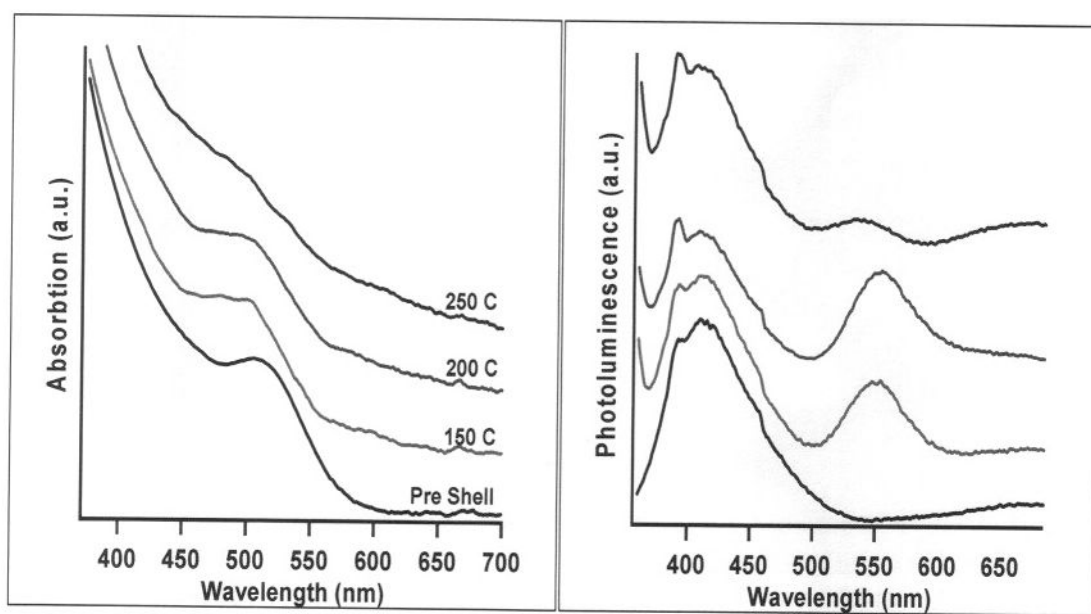


Figure 6.4. Room temperature absorption and photoluminescence of pyridine capped InGaP material shelled with ZnS at various temperatures.

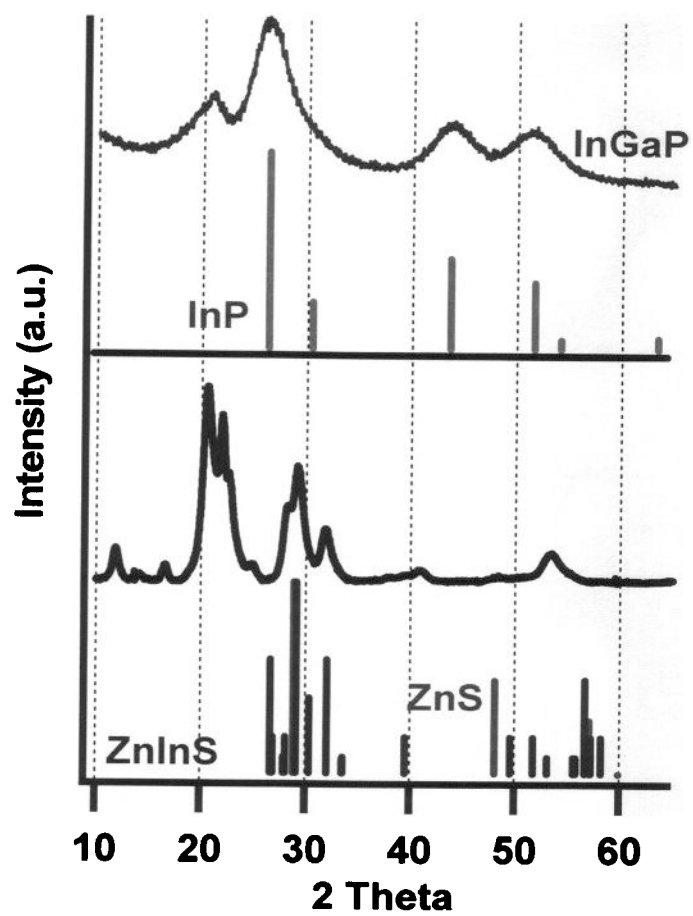
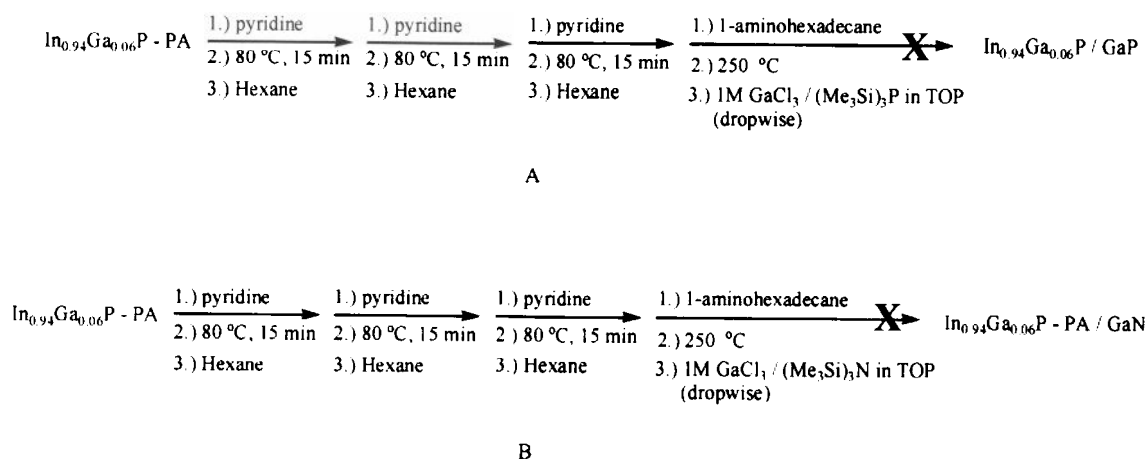


Figure 6.5. pXRD of 4.3 nm pyridine capped InGaP material shellied with ZnS at 150 °C compared to 4.3 nm core pyridine capped InGaP.

6.5 InGaP/GaP and InGaP/GaN Heterostructures

Each reaction was quickly heated to 250°C to avoid Ostwald ripening of the core nanoparticles. The Ga and P precursors were mixed in a syringe and injected dropwise into the core nanoparticle solution (500 µL in total). Initially the InGaP-py/HDA solution was red/clear. Minutes after the injection, the observed color of the solution began to blue shift; turning orange, yellow and finally clear/colorless. The absorption of the clear/colorless solution did not show either MLCT of any metal coordination complexes or wide gap nanocrystal excitons.



Scheme 6.2. Synthetic schemes for the preparation of III-V / III-V core shell structures.

The reaction of the core nanoparticles with the Ga and N precursors showed the same effect but less dramatic in terms of the rate of dissolution of the core

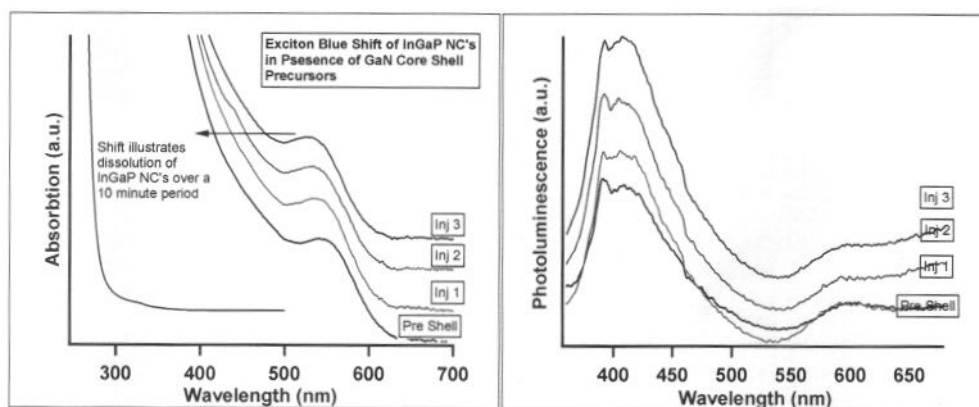
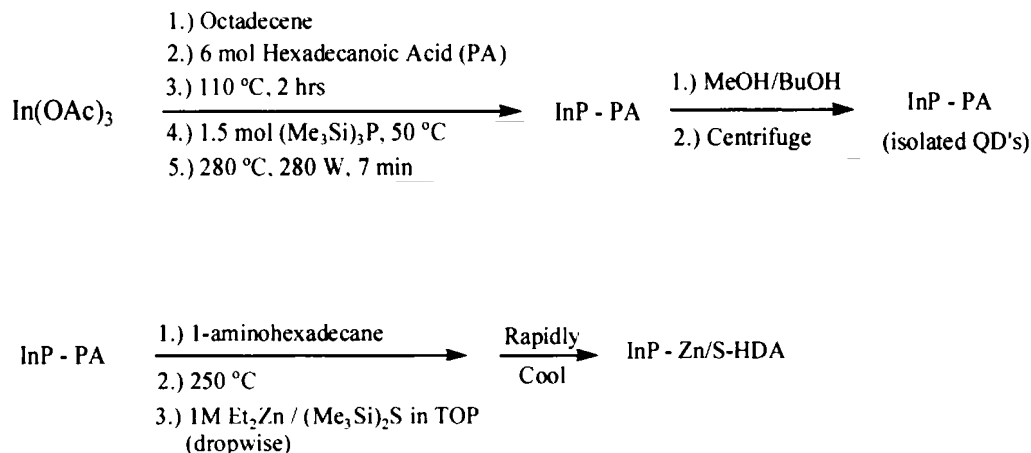


Figure 6.6. Room temperature absorption (left) and photoluminescence (right) of InGaP core nanoparticles in the presence of GaN shell precursors in toluene.

particles. This reaction was slow, no PL increase was observed so several injections were performed. Each injection accompanied a blue shift in the exciton. Over a ten minute period after the third injection, the core nanoparticles dissolved to form a clear/colorless solution as illustrated in figure 6.6. The Phase diagrams of binary and ternary phase diagrams are being investigated to help elucidate the phenomenon of particle dissolution.

6.6 InP/ZnS Heterostructures

The synthesis of InP, outlined in Scheme 6.3, was performed by the MW method by mixing indium (III) acetate and palmitic acid in octadecene in a three neck flask. The mixture was heated to 110°C for two hours under reduced pressure. When the solution formed an optically clear colorless solution the temperature was reduced to 50°C followed by an injection of tris(trimethylsilyl)phosphine. The resulting mixture formed an optically clear yellow/orange solution.



Scheme 6.3. Reaction scheme for ZnS shell process on binary InP.

5 ml of this solution was placed in a MW reaction vial and heated to 280°C for 15 minutes. The as prepared InP nanoparticles were approximately 4 nm in diameter and displayed orange/yellow photoluminescence and a solution QE of 0.01. The nanoparticles were isolated from the reaction solution, dispersed in toluene and precipitated with MeOH/BuOH.

A simultaneous injection method of Zn and S was used to grow the ZnS shell on InP. The InP core materials was rapidly heating in a round bottom flask to 250°C. Once that temperature was achieved, a slow, drop wise injection of Zn and S was carried out. To once the shelling was complete, the heating mantle was removed and the reaction was cooled. A similar procedure of shelling InP

The isolated nanoparticles showed a slight red shift in the first exciton by 25 nm illustrated in figure 6.7. The red shift in the core shell structures have been seen in CdSe/CdS, CdSe/ZnS and InP/ZnS from the core particle absorption. This has been attributed to alloying of the surface. The TEM of the InP shows approximately _____

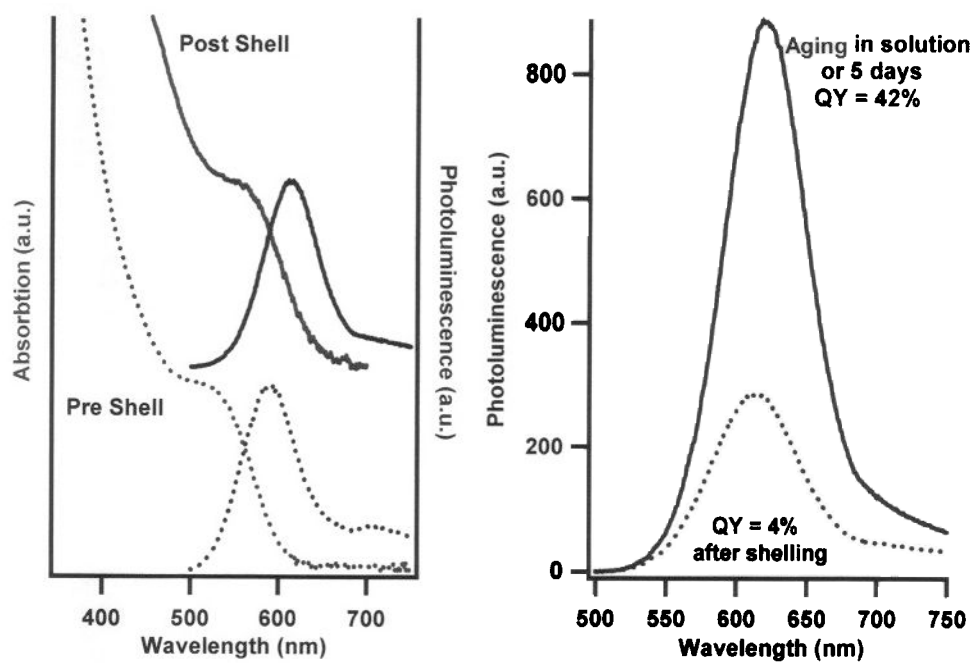


Figure 6.7. Room temperature absorption and photoluminescence of InP and InP/Zns (left) and photobrightening of InP/Zns in solution after 5 days.

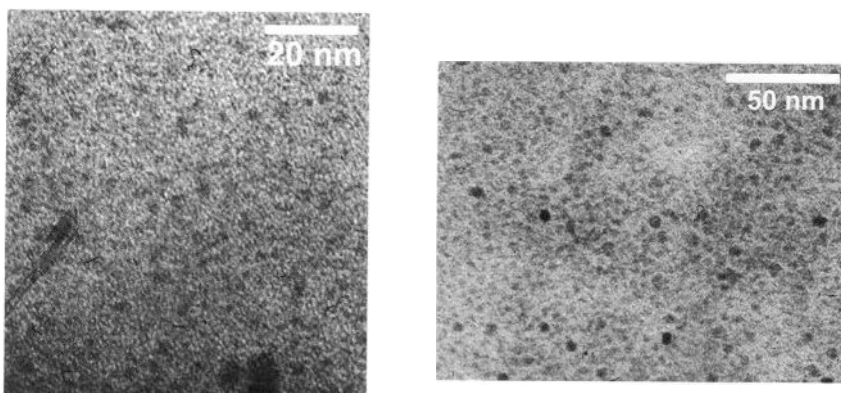


Figure 6.8. TEM of InP (left) and InP/ZnS (right). Samples were mounted on 400 mesh holey carbon grids. Images were taken on a Philips CM120 operated at 120KV

3.5 nm diameter particles (figure 6.7). After the ZnS shelling process the diameter increases to approximately 6nm. The shelled nanoparticles are better resolved at 120kV by the ZnS due to a larger electron density in the unit cell. Zinc Sulfide has a smaller lattice parameter than InP by 8%.

We have observed that simply reducing the speed of the injection (demonstrated in previous reports) of the shell precursors leads to a significant improvement in the heterostructure formation of InP/ZnS. In addition this process yields composite materials that exhibit a solution PL quantum efficiency of 40%, stable to precipitation in wet toluene in ambient conditions greater than 3 months.

Following a previously reported procedures for shell formation (i.e. using HDA or DDA coordinating solvent with diethylzinc and bis(trimethylsilyl)sulfide), it was observed that injecting the shell precursors at a rate of one drop every 2 seconds yields a considerably more resolved composite material as identified by XRD (below). The pXRD of InP/ZnS (figure 6.9) shows a more resolved heterostructure of the two materials than the InGaP/ZnS example. The $\langle 111 \rangle$ of InP ($2\theta = 26$) and ZnS ($2\theta = 29$) are clearly present when compared to the InGaP case. The ZnS intensity is less attributing it to only one or two atomic layers including a reconstruction of the InP and ZnS interface. Powder x-ray diffraction characterization reveals a significant shift in the peak positions to smaller lattice parameter indicative of ZnS as seen in Figure 6.9. It is clear that the heterostructure shifts to smaller lattice parameters from that of pure InP. The initial inspection of the diffraction from the heterostructure appears to be zinc blende with the $\langle 111 \rangle$ at 28

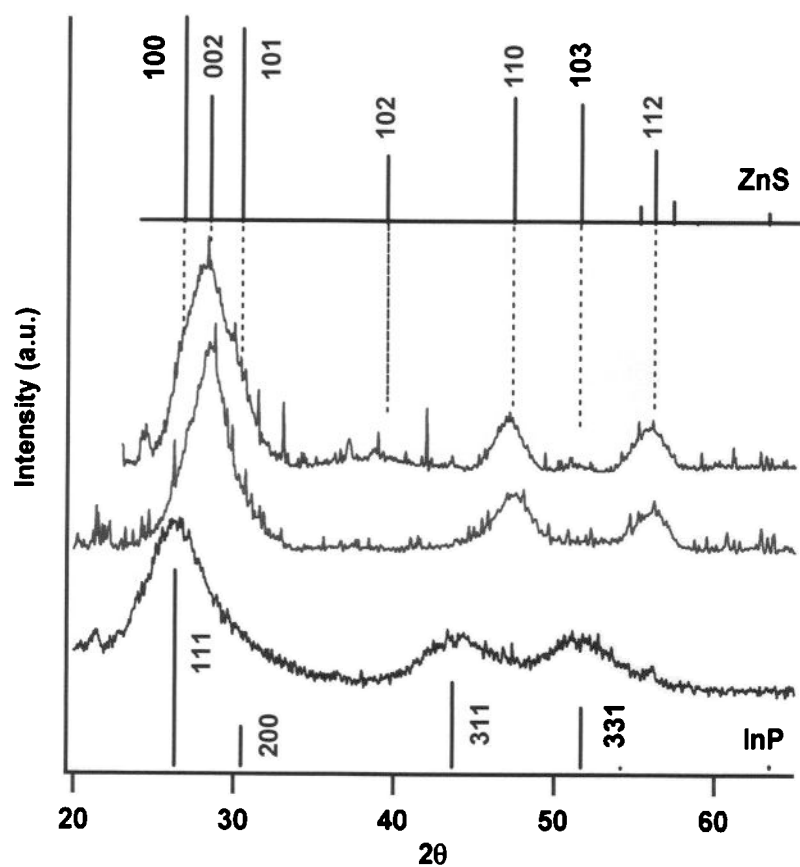


Figure 6.9. Powder x-ray diffractogram of pure InP nanoparticles, InP/ZnS heterostructure nanoparticles and pure ZnS nanoparticles. The ZnS nanoparticles were synthesized by the same method for forming core-shell structures with the same Zn and S concentrations.

2theta and the <220> and <311> at 47 and 56 2theta respectively. When this is compared to pure ZnS, a hexagonal phase can be fit. It shows a broadend, asymmetric <002> face. This may reveal that the first several monolayers of ZnS adopt the zinc blende structure to accommodate the strain. When sufficient layers are grown, the layers will relax to the lower energy hexagonal phase. TEM and XPS analysis are currently under way to elucidate how many atomic layers are present.

Based on the current experimental results it is believed that several atomic layers are present because the first layer will represent a strongly reconstructed layer. The strain is expected to propagate into the second and third layer. In the same manner, the strain will propagate into the core InP layers acting to compress the core surface to accommodate the smaller lattice parameter of ZnS. The powder diffraction is expected to show an average of the strain depending on the magnitude of the strain into both layers, which may be why no InP reflections are observed. Further analysis is needed to fully understand the observed pXRD coupled to the evident PL emission for InP.

Compound	Planes	Distance (Å)
Cubic ZnS - Bulk	220/311	9.972
Hexagonal ZnS - Bulk	110/112	10.04
ZnS - Nano	110/112	10.04
InP/ZnS - Nano	*/*	10.04
InP - Nano	220/311	10.98

Table 6.2. Distance between similar planes for the x-ray diffraction of compounds in figure 6.9. The planes listed are those that were used to calculate the distance.

To further elucidate which crystalline phase is adopted by the heterostructure, the planar distances were calculated (Table 6.2.) for the compounds in figure 6.9. The planar distance between $\langle 110 \rangle$ and $\langle 112 \rangle$ of bulk hexagonal ZnS is 10.04 Å. Comparing this to the cubic phase of ZnS, the distance between the $\langle 220 \rangle$ and $\langle 311 \rangle$ is 9.972 Å. Comparing the similar reflections from the heterostructure, the distance is 10.04 Å. This is surprising in that the cubic core lattice adopts a hexagonal phase. To what extent the hexagonal phase propagates is unclear at this time.

6.7 Conclusion

Reducing the injection speed of the Zn and S precursors has made a considerable improvement in the InP/ZnS heterostructures. The QE of the core-shell is stable at 40% in solution and stable towards precipitation. Surface reconstruction of the InP is optimized by reducing the speed of the shell precursors. In other words, a more ordered interface between InP and ZnS may be giving rise to higher QE. The structure of the core-shell adopts the a hexagonal ZnS crystalline phase. The reflection of InP are shifted to lower d spacing due to the compression of the core lattice by the Shell material.

ZnS shelling on InGaP has shown to be very difficult to control based on the limited number of reactions I have been able to perform. Binary and ternary phase diagrams may help to explain the phenomenon of particle dissolution and secondary ternary alloy byproducts. Acid capped versus pyridine capped material shows a

dramatic difference in reactivity towards Zn and S precursors in a solvothermal reaction

6.8. References

1. Shimizu, K. T.; Woo, W. K.; Fisher, B. R.; Eisler, H. J.; Bawendi, M. G., *Physical Review Letters* **2002**, 89, (11).
2. Qu, L. H.; Peng, X. G., *Journal of the American Chemical Society* **2002**, 124, (9), 2049-2055.
3. Micic, O. I.; Nozik, A. J.; Lifshitz, E.; Rajh, T.; Poluektov, O. G.; Thurnauer, M. C., *Journal of Physical Chemistry B* **2002**, 106, (17), 4390-4395.
4. Sung, M. M.; Kim, C.; Bu, H.; Karpuzov, D. S.; Rabalais, J. W., *Surface Science* **1995**, 322, (1-3), 116-132.
5. Ponchet, A.; Lecorre, A.; Godefroy, A.; Salaun, S.; Poudoulec, A., *Journal of Crystal Growth* **1995**, 153, (3-4), 71-80.
6. Jin, J. M.; Lewis, L. J., *Surface Science* **1995**, 325, (3), 251-262.
7. Anderson, G. W.; Hanf, M. C.; Norton, P. R.; Lu, Z. H.; Graham, M. J., *Applied Physics Letters* **1994**, 65, (2), 171-173.
8. Srivastava, G. P., *Reports on Progress in Physics* **1997**, 60, (5), 561-613.
9. Talapin, D. V.; Gaponik, N.; Borchert, H.; Rogach, A. L.; Haase, M.; Weller, H., *Journal of Physical Chemistry B* **2002**, 106, (49), 12659-12663.

10. Kuno, M.; Fromm, D. P.; Gallagher, A.; Nesbitt, D. J.; Micic, O. I.; Nozik, A. J., *Nano Letters* **2001**, 1, (10), 557-564.
11. Micic, O. I.; Cheong, H. M.; Fu, H.; Zunger, A.; Sprague, J. R.; Mascarenhas, A.; Nozik, A. J., *Journal of Physical Chemistry B* **1997**, 101, (25), 4904-4912.
12. Micic, O. I.; Sprague, J.; Lu, Z. H.; Nozik, A. J., *Applied Physics Letters* **1996**, 68, (22), 3150-3152.
13. Robach, Y.; Besland, M. P.; Joseph, J.; Hollinger, G.; Viktorovitch, P.; Ferret, P.; Pitaval, M.; Falcou, A.; Post, G., *Journal of Applied Physics* **1992**, 71, (6), 2981-2992.
14. Chen, Y.; Luo, Y. S.; Seo, J. M.; Weaver, J. H., *Physical Review B* **1991**, 43, (5), 4527-4530.
15. Yamaguchi, M., *Journal of Applied Physics* **1982**, 53, (3), 1834-1835.
16. Griffiths, J. E.; Schwartz, G. P.; Sunder, W. A.; Schonhorn, H., *Journal of Applied Physics* **1982**, 53, (3), 1832-1833.
17. Olivier, J.; Faulconnier, P.; Poirier, R., *Journal of Applied Physics* **1980**, 51, (9), 4990-4995.
18. Soukiassian, P.; Bakshi, M. H.; Hurych, Z., *Journal of Applied Physics* **1987**, 61, (7), 2679-2681.
19. Cao, Y. W.; Banin, U., *Journal of the American Chemical Society* **2000**, 122, (40), 9692-9702.
20. Reiss, P.; Bleuse, J.; Pron, A., *Nano Letters* **2002**, 2, (7), 781-784.

21. van Sark, W.; Frederix, P.; Van den Heuvel, D. J.; Gerritsen, H. C.; Bol, A. A.; van Lingen, J. N. J.; Donega, C. D.; Meijerink, A., *Journal of Physical Chemistry B* **2001**, 105, (35), 8281-8284.
22. Gerion, D.; Pinaud, F.; Williams, S. C.; Parak, W. J.; Zanchet, D.; Weiss, S.; 9
23. Peng, X. G.; Schlamp, M. C.; Kadavanich, A. V.; Alivisatos, A. P., *Journal of the American Chemical Society* **1997**, 119, (30), 7019-7029.
24. Schlamp, M. C.; Peng, X. G.; Alivisatos, A. P., *Journal of Applied Physics* **1997**, 82, (11), 5837-5842.
25. Banin, U.; Bruchez, M.; Alivisatos, A. P.; Ha, T.; Weiss, S.; Chemla, D. S., *Journal of Chemical Physics* **1999**, 110, (2), 1195-1201.
26. Harrison, M. T.; Kershaw, S. V.; Rogach, A. L.; Kornowski, A.; Eychmuller, A.; Weller, H., *Advanced Materials* **2000**, 12, (2), 123-125.
27. Micic, O. I.; Smith, B. B.; Nozik, A. J., *Journal of Physical Chemistry B* **2000**, 104, (51), 12149-12156.
28. Borchert, H.; Haubold, S.; Haase, M.; Weller, H., *Nano Letters* **2002**, 2, (2), 151-154.
29. Haubold, S.; Haase, M.; Kornowski, A.; Weller, H., *Chemphyschem* **2001**, 2, (5), 331-334.
30. Langof, L.; Fradkin, L.; Ehrenfreund, E.; Lifshitz, E.; Micic, O. I.; Nozik, A. J., *Chemical Physics* **2004**, 297, (1-3), 93-98.

31. Dabbousi, B. O.; RodriguezViejo, J.; Mikulec, F. V.; Heine, J. R.; Mattoussi, H.; Ober, R.; Jensen, K. F.; Bawendi, M. G., *Journal of Physical Chemistry B* **1997**, 101, (46), 9463-9475.
32. Battaglia, D.; Peng, X. G., *Nano Letters* **2002**, 2, (9), 1027-1030.
33. Strouse, G. F. G., J.A.; Magana, D. Method for Synthesis of Colloidal Nanoparticles.

Chapter 7. Synthesis of Wide Band Gap Semiconductors Nanoparticles by microwave heating.

7.1 Introduction

A largely undeveloped area in nanoparticle synthesis is a large class of metal oxide, nitride and oxynitride materials. These wide band gap nanocrystalline colloids have promising application in solar cells^{1,2}, flat panel displays³⁻⁶, sensors⁷⁻⁹.

Transparent conducting oxides (TCO's), like In_2O_3 , have a wide variety of application stemming from there high temperature stability and conductivity¹⁰⁻¹³.

UV and blue GaN based diodes for example, are being integrated into solid state lighting architectures and display applications¹⁴⁻¹⁶. These are a strikingly stable, high performance material that shows promising applications in the nanoscale size domain.

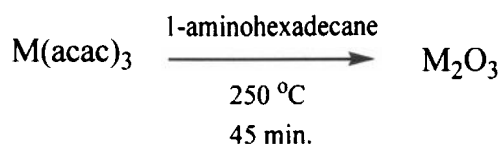
On the nanoscale, one can extrapolate the general stability of crystalline colloids in the order:

oxide > oxy nitride > nitride > oxy sulfide > sulfide

simply by considering the size. Since most transition metal and semiconductor bulk materials have a native oxide layer at the surface with nanometers deep depending on the material, at the nanoscale for the , a 4 nm spehere for example, the entire nanocrystal can be considered a surface and fully oxidize in time. Based on this

assumption, metal oxide and oxynitrides have thermodynamically stable structures compared to their calcogenide and pnitide analogs. Considering the harsh environment that solid state lighting phosphors will be exposed to, temperatures in excess of 150°C and intense UV irradiation, building off of the crystalline framework and wide gap of the metal oxides and oxynitride materials is advantageous. Moreover, they are good candidates to evaluate doped phases based on Eu^{2+} , Ce^{2+} and Y^{3+} to name a few new visible phosphors.

This chapter will demonstrate that indium and gallium oxide nanoparticles can be readily synthesized from a metal acetylacetonate in hexadecylamine by microwave heating where the acac ligand acts as the oxygen source. XPS and pXRD was performed on In_2O_3 to confirm the oxide phase. It is shown that the binding energy of the In 3d5/2 of the InGaP overlaps with that of In_2O_3 indicating that the surface has an oxide layer indicative of In_2O_3 .



Scheme 7.1 General reaction of metal acetylacetonate salts in hexadecylamine to form a metal oxide or mixed metal oxides by microwave synthesis.

It has been observed in literature for many years that metal acetates and acetylacetonates decompose at high temperatures in the solid state to form oxide

films¹⁷⁻²⁰. The decomposition of metal acetylacetonates in hexadecylamine yields very crystalline nanoparticles. Scheme 7.1 is a general synthetic path used to form oxides of indium and gallium. Microwave heating of the precursors at 250°C for 45 minutes yields isolable oxide nanoparticles. The pXRD and TEM show that these materials are highly crystalline and approximately 10 nm or less in diameter.

Lastly, the colloidal synthesis of indium oxynitride and indium nitride was examined. The reaction between indium III acetylacetonate or indium III acetate and nonamethyltrisilazane in trioctylphosphine was examined and well as several reactions utilizing indium III chloride. Structural characterization of the material revealed that the crystalline phase is In_2O_3 , but the absorbance and photoluminescence show a tremendous red shift compared to binary In_2O_3 . This is not surprising given that metallic acetylacetonates decompose readily to yield a thermodynamically stable oxide. More work is need to fully characterize the surface to identify N independently from the ligand shell and is currently being conducted

7.2 Experimental Methods

Synthesis of Ga_2O_3 Synthesis of Ga_2O_3 is based on a modification of literature methods²¹. Gallium-2-4-pentanedionate (400mg) and hexadecylamine (3.15g) were massed into a microwave reaction tube and sealed with a septum seal. The contents were heated to 50°C and degassed by 3 cycles of vacuum/Ar purging. The reaction vessel was then placed into the microwave and heated to 250°C for 45min. The

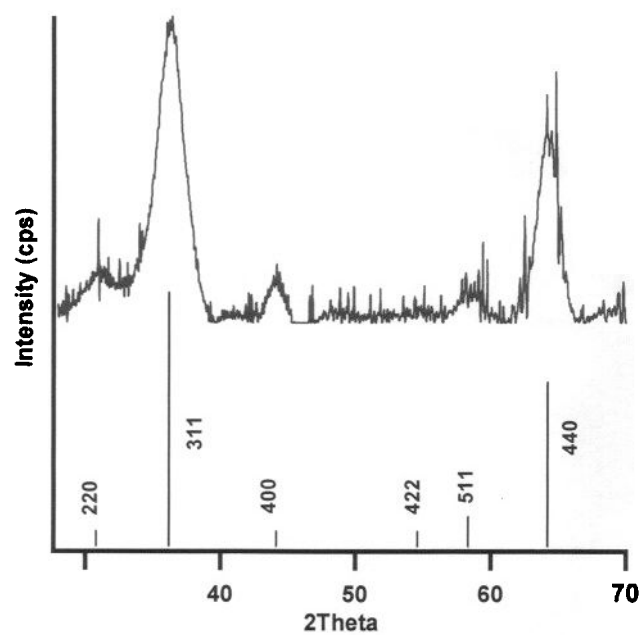
resulting white slurry was diluted with 10ml of chloroform. The Ga_2O_3 nanoparticles were collected by adding copious amounts of methanol to induce flocculation and the solid was collected by centrifugation.

Synthesis of In_2O_3 Synthesis of In_2O_3 is based on a modification of literature methods²¹. Indium-2-4-pentanedionate (710mg) and hexadecylamine (5.0g) were massed into a microwave reaction tube and sealed with a septum seal. The contents were heated to 75°C and degassed by 3 cycles of vacuum/Ar purging. The reaction vessel was then placed into the microwave and heated to 250°C for 45min. The resulting off white slurry was diluted with 6ml of chloroform. The In_2O_3 nanoparticles were collected by adding copious amounts of acetone to induce flocculation and the solid was collected by centrifugation.

Synthesis of $\text{In}_2\text{N}_x\text{O}_{y-x}$ Synthesis of indium oxynitride was investigated using microwave methods. A solution of indium III acetylacetonate and hexadecylamine was prepared in trioctylphosphine and degassed at 90°C. Separately, a stock solution of nonamethyltrisilazane was prepared in fractionally distilled hexadecene. The precursors were mixed in a microwave vial to make 5 ml of solution with a N:In mole ratio of 1.5. The solution was slowly heated to 220°C followed by rapid thermal quenching. The crystallites were isolated from the mother solution by precipitation with 1:1 methanol:acetone mixture. The crystallites were collected by evaporation of chloroform to yield approximately 1 mg of clear colorless crystals.

7.3 Synthesis of Ga₂O₃

The synthesis of gallium oxide by microwave heating is stunningly straight forward. Heating gallium III acetylacetonate, a single source precursor, in hexadecylamine yields highly crystalline, cubic phase colloidal nanopowders observed in figure 7.1a. The colloids can easily be dispersed in toluene for optical measurements. Figure 7.1b shows the optical absorbance and photoluminescence of colloidal gallium oxide. This shows a well resolved excitonic feature centered around 270nm. Overlaid is the PL profile which shows a shoulder center 295nm with a long rising edge toward lower energy. The shoulder is weak band edge PL with majority of defect emission beyond 300nm.



X-ray diffraction of as prepared materials identified as the cubic

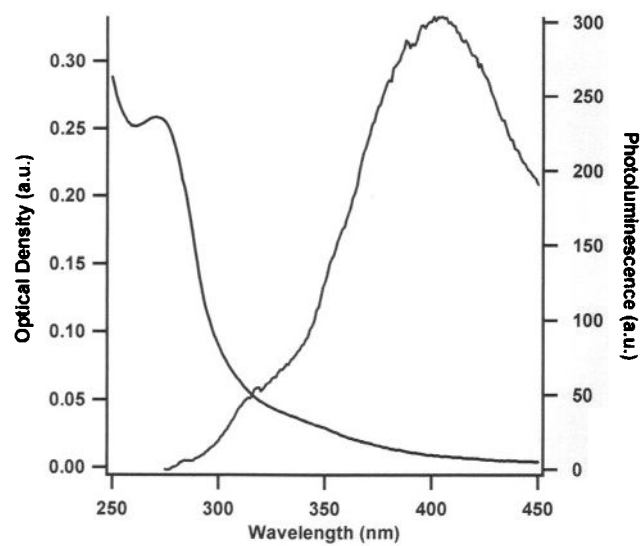


Figure 7.1b. Optical absorbance and photoluminescence of as prepared Ga_2O_3 at room temperature diluted in toluene.

7.4 Synthesis of In₂O₃

Indium oxide was prepared by the same procedure as gallium oxide using indium III acetylacetonate. The x-ray diffractogram in figure 7.2a shows highly crystalline indium oxide in the cubic phase. The TEM micrograph in figure 7.2b shows nearly spherical isolated domains approximately 10 nm in diameter.

The surface of the material was characterized by x-ray photoelectron spectroscopy (XPS). The survey spectrum in figure 7.3a shows characteristic signals from In 3d_{5/2} and O 1s and 2s. A high resolution spectrum of the In 3d_{5/2} (figure 7.3b) shows the binding energy of In 3d_{5/2} is 444.2 eV which agrees with literature²².

23

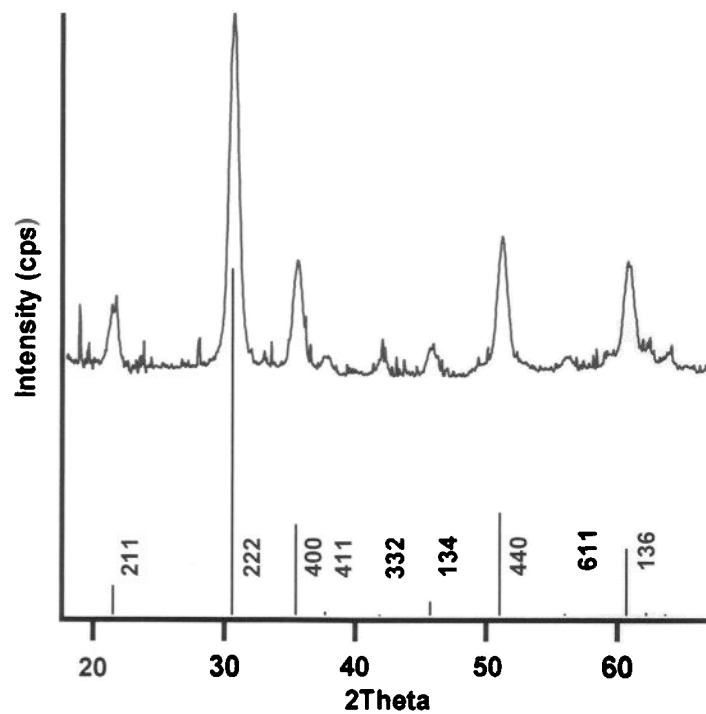


Figure 7.2a. Xray diffraction of powder collected from microwave reaction of $\text{In}(\text{acac})_3$ and hexadecylamine.

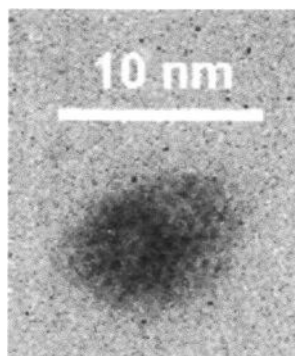


Figure 7.2b. TEM of colloidal material prepared by $\text{In}(\text{acac})_3$ and hexadecylamine.

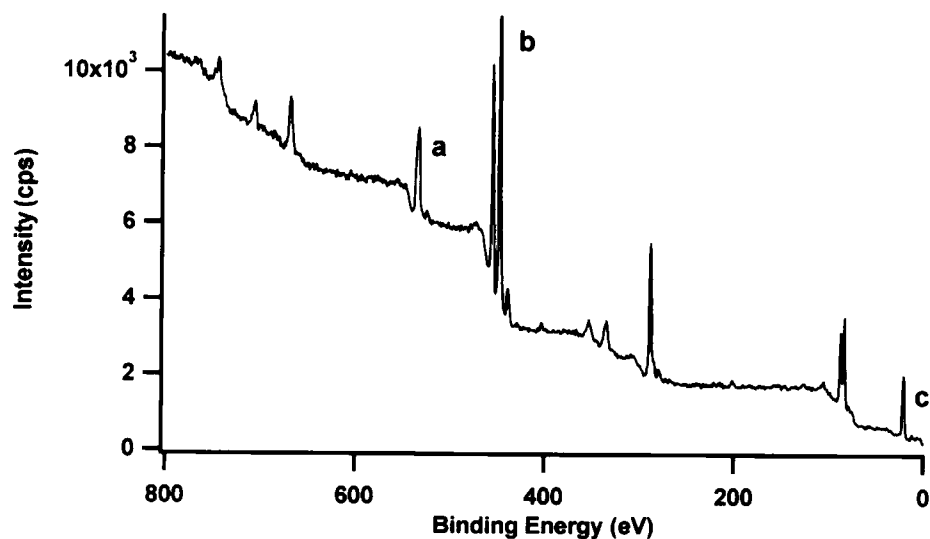


Figure 7.3a. X-ray photoelectron survey spectra of as prepared In_2O_3 in hexadecylamine; (a) oxygen 1s, (b) indium 3d $_{5/2}$ and (c) oxygen 2s.

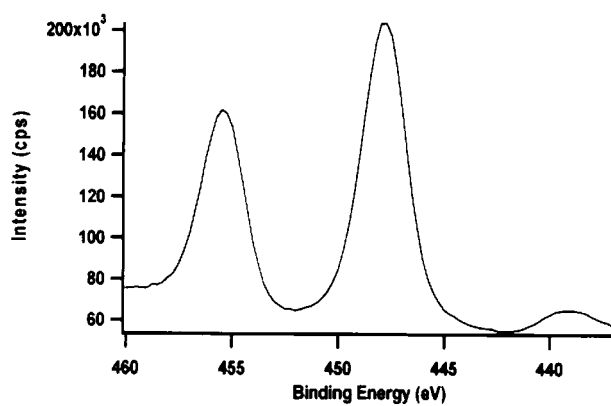


Figure 7.3b. High resolution spectrum of indium 3d $_{5/2}$.

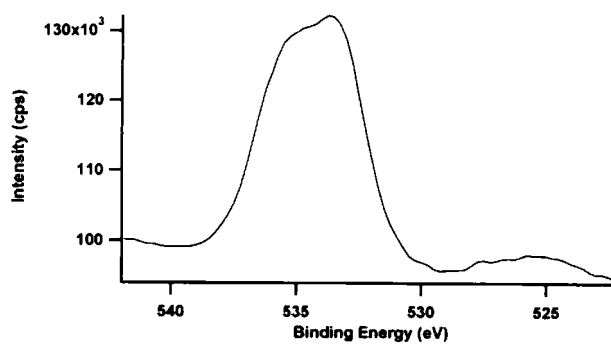
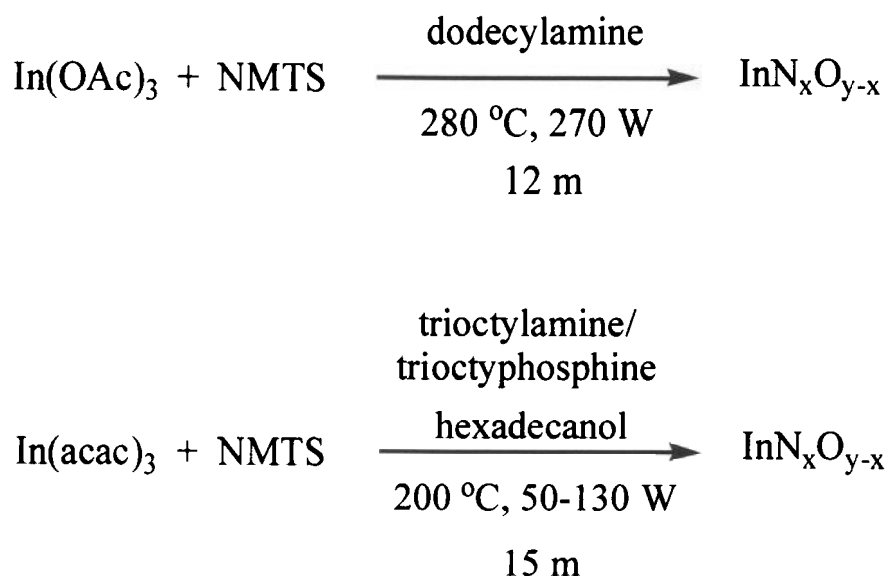


Figure 7.3c. High resolution spectrum of oxygen 1s.

7.5 Synthesis of Oxynitrides

Indium oxynitride was successfully grown with microwave heating at low temperature. This is the first report of high quality photoluminescence from a colloidal indium oxide/oxynitride nanoparticle. The following scheme illustrates two possible reaction pathways to grow oxynitride particles.



Scheme 7.2. Microwave driven reactions developed to form oxide/oxynitride colloidal nanoparticles. Nonamehtytrisilazane (NMTS) was used at the nitrogen source each each example. If indium III acetate (OAc) is used in place of indium III acetcetyacetate (acac), no excitonic absorbance is observed.

The indium salt has a profound influence of the optical properties of the as prepared material. If indium III acetylacetonate is used as the starting material, the colloids show very intense band edge luminescence. However, if indium III acetate is used,

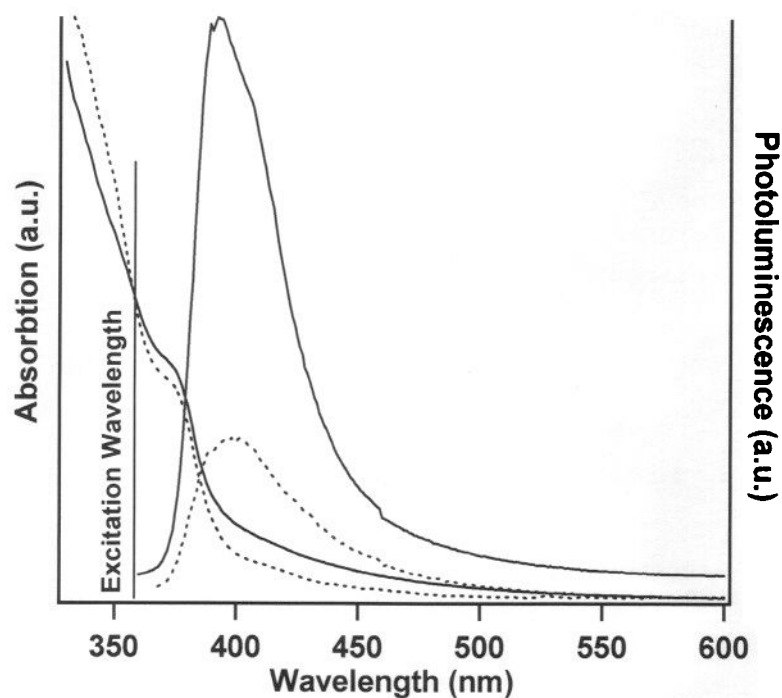


Figure 7.4. Optical absorbance and photoluminescence of as prepared indium oxynitride nanoparticles diluted in toluene. The excitation feature is largely unchanged by increasing the temperature ramp rate from 13°C/min (solid trace) to 25°C/min (dotted trace) during the formation of the nanoparticles. But the PL show a dramatic decrease in intensity by a factor of three when the ramp rate is 25°C/min.

there is no measurable band edge luminescence. Most interesting is the influence of the rate of heating and final reaction temperature on the band edge PL when the acac salt is used shown in figure 7.4. If the reaction proceeds with a slow ramp rate, approximately 13°C/min, intense PL is observed. If the ramp rate is increased (~25°C/min) the luminescence intensity is decreased by a factor of three. This observation may be due to either of the following: 1. a slow and steady decomposition of the pnictide precursor or 2. a slow formation of the lattice inhibiting defect sites

In figure 7.4, the tailing edge of the absorption from 390 to 500 nm is most likely due to nanoparticle aggregates. The surfactants used in the growth are not strongly bound to the surface by steric effects and the N atom being sp³ hybridized. This hybridization decreased the s character of the N reducing its sigma donating ability. These factors will contribute to aggregates in solution, but they promote the most favorable growth of any reaction scheme thus far.

The as prepared material is extremely difficult to isolate from the reaction solution as a powder. Ethanol, 2-propanol, and 1-butanol are miscible with the reaction solution, but it doesn't promote precipitation to any appreciable extent. This made HRTEM unsuccessful. Further work is needed to develop a purification method to isolate the nanoparticles.

X-ray diffraction was performed on this sample as seen below in figure 7.5. The crystallites were insoluble after sitting at ambient conditions for 3 hours. The reflection intensity ratios and d spacing indicate that a cubic phase of In₂O₃ is present

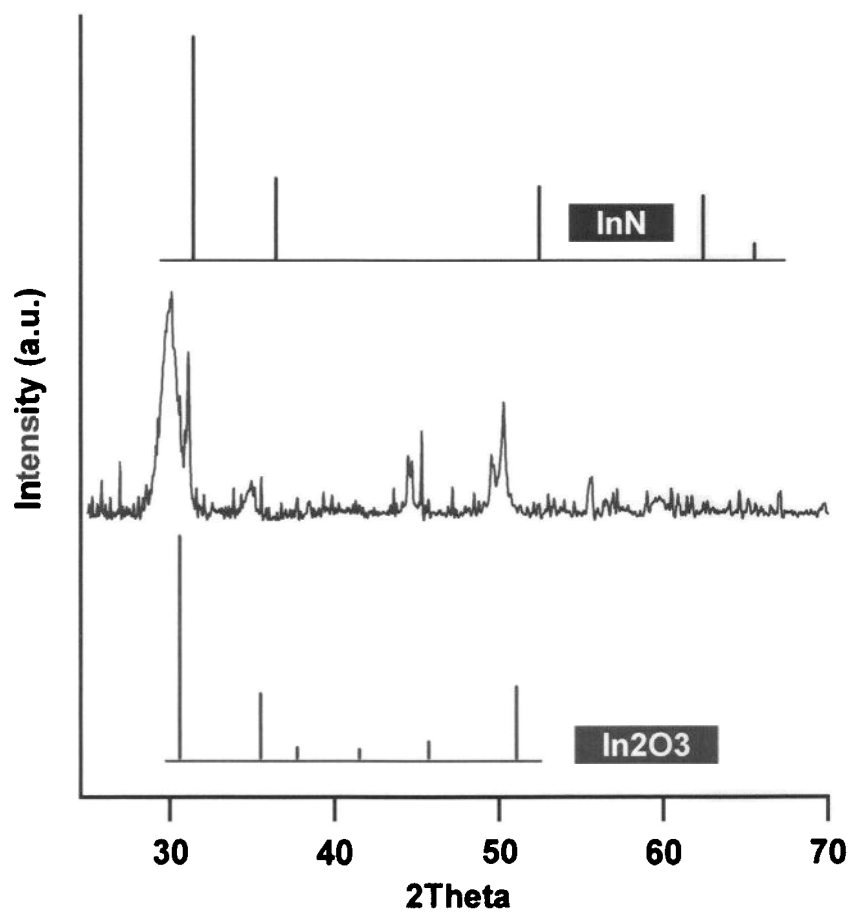


Figure 7.5. Powder x-ray diffraction of material collected from the reaction of $\text{In}(\text{acac})_3$ and $\text{N}(\text{SiMe}_3)_3$ in TOP.

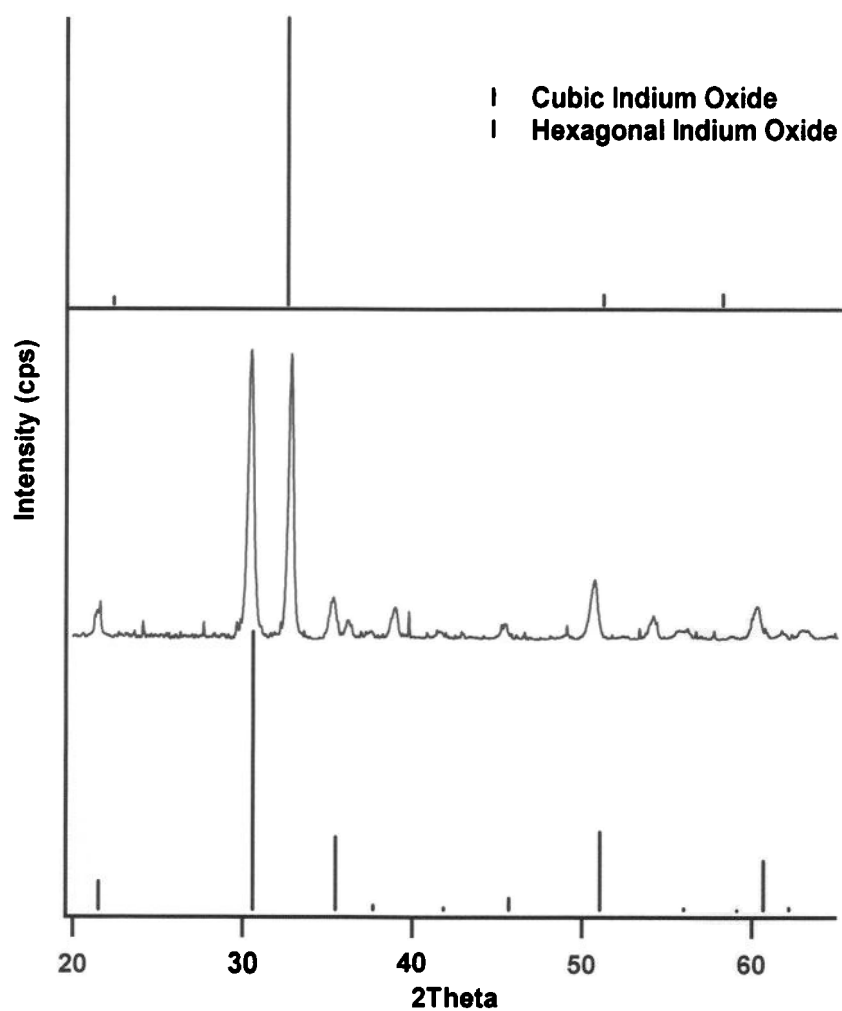


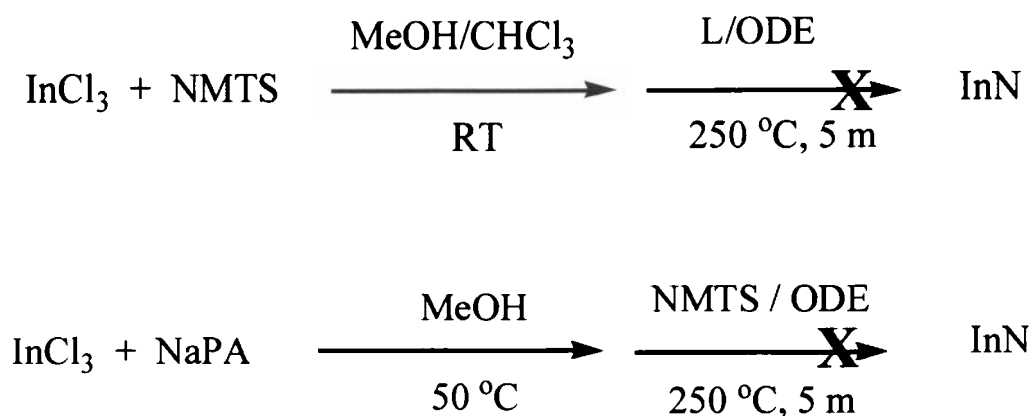
Figure 7.6. XRD of black precipitate formed at temperatures greater than 220 °C from the reaction of $\text{In}(\text{acac})_3$ and $\text{N}(\text{SiMe}_3)_3$ in TOP.

in solution. This is surprising that an oxide phase can be synthesized at such low temperatures (less than 220 °C) in less than 20 minutes.

If the temperature of the reaction is raised above 220°C, a black precipitate is formed. The black precipitate was identified as a mixture of cubic and hexagonal phase of In_2O_3 by x-ray diffraction. The intensity and the narrow FWHM of the hexagonal $\langle 110 \rangle$ and the cubic $\langle 222 \rangle$ suggest that both phases are bulk and present in similar concentrations.

The formation of group III nitrides is not possible under the current reaction conditions. That is, the solution phase reaction between oxygen containing group III salts and nonamehtyltrisilazane. The thermodynamic path for forming the metal oxides is preferred over the nitride formation. In part this is due to the degradation of the group III salt in which the ligand donates the oxygen needed for oxide formation (i.e. acetate or 2,4-pentanedionate). The mechanism for oxide formation under these conditions is being investigated.

In an effort to form the pure phase of InN in solution, indium III chloride was substituted as the metallic starting material to eliminate oxygen as a reactant toward the oxide nanoparticles. The two general reaction paths that were used are shown in scheme 7.3.



Scheme 7.3. Reaction scheme used for the attempted formation of InN nanoparticles. In the scheme, L denotes the ligands which were used in separate reactions. They are as follows, octylamine, dodecylamine, hexadecylamine, polyvinylpyrrolidone, and trioctylamine. The mole ratio of L to ODE was fixed at 1 for each reaction. NaPA denotes palmitic acid sodium salt.

A dehalosilation reaction was attempted between indium III chloride and nonamethyltrisilazane in a 1:1 mole ratio of coordinating and noncoordinating solvent. The preparation of the reaction and loading of the microwave vials was carried out with anhydrous solvents in a glove box with an equipped dry-train system. Octadecene and the amines were dried and distilled prior to use.

Briefly, indium III chloride and nonamethyltrisilazane were dissolved in a mixture of chloroform/methanol for working stock solutions. The reactants were mixed in microwave vials and diluted with coordinating/noncoordinating solvent. The ratio of N:In was 1.5 with a concentration of 20mM in In (total volume of 5 ml). The reactions were carried out in the microwave for a reaction time of 5 minutes at 250°C.

Different chain length amines were added to identical reactions to observe reactivity differences of the starting material. The reactions containing trioctylamine, octylamine, dodecylamine and hexadecylamine displayed the same characteristics in terms of slow ramping rates and no nanoparticle formation. Even with extended reaction times of 3 hours at 250°C, no observable change in the starting material was seen by UV-Vis spectroscopy. Polyvinylpyrrolidone (PVP) had a peculiar reactivity towards the ions. The reaction temperature rose rapidly due the absorption of the PVP. The resulting product was an insoluble brown residue on the sides of the reaction vials which displayed green/blue luminescence under 365 nm hand lamp excitation. The supernatant was clear colorless and illuminated blue from the polymer excitation.

Lewis acid/base adduct formation between indium III chloride and nonamethyltrisilazane is unfavorable due to the steric hindrance of the trimethylsilyl substituents on the nitrogen. Other routes to InN using indium amido dimers and organometallic clusters are being investigated as suitable precursors for the formation of InN nanoparticles. GaN nanoparticles were also tried in the same manner as described previously for InN, but no particle formation was observed.

7.6 Conclusion

Metal oxides are readily formed from their parent acetylacetonate salts in hexadecylamine acting as a “single source precursor”. The decomposition of the acac donates the oxygen. This hinders these salts or any oxygen containing salts from

being used as precursors for group III nitrides. It was observed by XPS analysis that the surface of is that of indium oxide.

Continuing work is needed to characterize the indium oxide/oxy-nitrides. XPS is needed to characterize the extent of nitridation of the surface. Nitrogen doping at the surface is what gives rise the violet emission observed from an oxide host.

Lastly, InN is one of the most difficult semiconductor colloids to form by solution phase chemistry. Excluding the oxygen containing In salts leaves indium III chloride and trimethylindium and indium amido dimers. The lewis acid/base adduct formation between nonamethyltrisilazane and indium III chloride is unfavorable. The steric hindrance of the nitrogen reduces the basicity and renders it non-reactive.

The synthesis of InN will need a more elegant approach. Two considerations have to be made due to its high thermodynamic barrier for In-N bond formation, a more reactive nitrogen source and a preformed In-N bond. Synthesis of (Me)NH(SiMe₃) should be investigated as a N source as well as the synthesis of a series of indium/nitrogen dimeric starting materials.

7.7 References

1. Xia, Y. N.; Yang, P. D.; Sun, Y. G.; Wu, Y. Y.; Mayers, B.; Gates, B.; Yin, Y. D.; Kim, F.; Yan, Y. Q., *Advanced Materials* **2003**, 15, (5), 353-389.
2. Torrison, L.; Tolle, J.; Tsong, I. S. T.; Kouvetakis, J., *Thin Solid Films* **2003**, 434, (1-2), 106-111.

3. Gubin, S. P.; Kataeva, N. A.; Khomutov, G. B., *Russian Chemical Bulletin* **2005**, 54, (4), 827-852.
4. Gautam, U. K.; Sardar, K.; Deepak, F. L.; Rao, C. N. R., *Pramana-Journal of Physics* **2005**, 65, (4), 549-564.
5. Law, M.; Goldberger, J.; Yang, P. D., *Annual Review of Materials Research* **2004**, 34, 83-122.
6. Bae, S. Y.; Seo, H. W.; Choi, H. C.; Park, J.; Park, J., *Journal of Physical Chemistry B* **2004**, 108, (33), 12318-12326.
7. Kinski, I.; Scheiba, F.; Riedel, R., *Advanced Engineering Materials* **2005**, 7, (10), 921-927.
8. Kaskel, S.; Chaplais, G.; Schlichte, K., *Chemistry of Materials* **2005**, 17, (1), 181-185.
9. Janik, J. F., *Powder Technology* **2005**, 152, (1-3), 118-126.
10. Zhang, W.; Huang, Z.; Li, T.; Tang, Q.; Ma, D. K.; Qian, Y. T., *Chemistry Letters* **2005**, 34, (1), 118-119.
11. Cao, H. Q.; Qiu, X. Q.; Liang, Y.; Zhu, Q. M.; Zhao, M. J., *Applied Physics Letters* **2003**, 83, (4), 761-763.
12. Yu, B. L.; Bu, H. J.; Wu, X. C.; Zhang, G. L.; Tang, G. Q.; Chen, W. J.; Zhu, C. S.; Gan, F. X., *Acta Physica Sinica* **1999**, 48, (2), 320-325.
13. Yu, B. L.; Zhu, C. S.; Gan, F. X.; Huang, Y. B., *Optical Materials* **1997**, 7, (3), 103-107.
14. D'Andrade, B. W.; Forrest, S. R., *Advanced Materials* **2004**, 16, (18), 1585-1595.

15. Haerle, V.; Hahn, B.; Kaiser, S.; Weimar, A.; Bader, S.; Eberhard, F.; Plossl, A.; Eisert, D., *Physica Status Solidi a-Applied Research* **2004**, 201, (12), 2736-2739.
16. Shatalov, M.; Chitnis, A.; Adivarahan, V.; Lunev, A.; Zhang, J.; Yang, J. W.; Fareed, Q.; Simin, G.; Zakheim, A.; Khan, M. A.; Gaska, R.; Shur, M. S., *Applied Physics Letters* **2001**, 78, (6), 817-819.
17. Denomme, D. R.; Richardson, A. A.; Miller, D. O.; Slusher, L. E.; Vohs, J. K.; Fahlman, B. D., *Abstracts of Papers of the American Chemical Society* **2005**, 229, U1070-U1071.
18. Guzman, J.; Gates, B. C., *Langmuir* **2003**, 19, (9), 3897-3903.
19. Tsuchiya, T.; Watanabe, A.; Imai, Y.; Niino, H.; Yamaguchi, I.; Manabe, T.; Kumagai, T.; Mizuta, S., *Japanese Journal of Applied Physics Part 2-Letters* **1999**, 38, (10A), L1112-L1114.
20. Van der Voort, P.; White, M. G.; Vansant, E. F., *Langmuir* **1998**, 14, (1), 106-112.
21. Seo, W. S.; Jo, H. H.; Lee, K.; Park, J. T., *Advanced Materials* **2003**, 15, (10), 795.
22. Zhang, J.; Qing, X.; Jiang, F. H.; Dai, Z. H., *Chemical Physics Letters* **2003**, 371, (3-4), 311-316.
23. Zhou, H. J.; Cai, W. P.; Zhang, L. D., *Materials Research Bulletin* **1999**, 34, (6), 845-849.

Appendix A. Method for measuring relative quantum yield

Appendix A outlines the results obtained from calculating the relative quantum efficiencies of etched InGaP nanoparticles in toluene compared with rhodamine 6G in ethanol. Two approaches to the data collection were used to observe the effect of self absorption of the nanoparticle and dye as well as the concentration effect of both species to the observed quantum efficiency of the nanoparticle.

As the use of nanoparticle phosphors become more of a commercial reality, the most accurate measure of the quantum efficiency is very important. The literature over the past several years have reported a broad range of quantum yields of II-VI (visible / UV) and III-V (visible / IR) for nanoparticles. For example, the reports have ranges from 0.20 to 0.95 for CdSe and from 0.005 to 0.40 for InP (chemically etched and unetched). Yet these reports do not include experimental details on how the quantum efficiency was obtained. This fosters ambiguity when researchers attempt to reproduce stated quantum efficiencies of nanoparticles prepared by the same method.

One example in the current literature is the surprisingly low quantum efficiencies calculated by Wilcoxon and co-workers [1] for CdSe/ZnS purchased from a commercial supplier. A more detailed description of the QE measurement is outlined by Wilcoxon than most other reports. Wilcoxon calculates QE's of the core/shell nanoparticles ranging from 0.02 to 0.32 depending on the size of the

cluster. This begs the question about what is the most accurate approach to calculate solution quantum efficiencies.

This report suggests a suitable way to calculate solution quantum yields for a highly luminescent nanoparticle. The comparative standard to the etched InGaP is Rhodamine 6G. It was chosen as the dye standard for several reasons: 1. it is commonly used to compare QE of visible fluorescent nanoparticles, 2. the fluorescence is stable in ethanol for months, 3. the QE is constant over a broad excitation range in pure ethanol.

Kubin et al [2] has performed a detailed study on using rhodamine as a comparison for the QE of other dyes. Their conclusion is that when rhodamine is used as a comparative dye the PL maxima should be obtained on an infinitesimally dilute solution. Because of the small stokes shift in rhodamine dyes, self absorption is a cogent issue.

The expression used to determine the QE is outlined by Crosby and co-workers [3]:

$$\phi_{em} = \phi'_{em} \left(I / I' \right) \left(A' / A \right) \left(n / n' \right)^2 \quad (1)$$

Where I (sample) and I' (reference) are integrated emission peak areas. A (sample) and A' (reference) are the absorbance at the excitation wavelength, and n (sample) and n' (reference) are the refractive indices of the solvents. ϕ'_{em} is the quantum efficiency of the reference.

The InGaP was etched according to methods stated in previous progress reports. Rhodamine 6G was purchased from Exciton Inc (Dayton, OH). Toluene and ethanol were spectroscopic purity (UHP). The 10 mm x 10 mm and 10 mm x 4 mm quartz fluorescence cells were purchase from Starna (Atascadero, CA). The solutions were prepared and studied under ambient conditions with no degassing. The absorbance measurements were collected on a Varian Bio Eclipse UV – Vis spectrometer. The Fluorescence spectra were collected on a Varian Cary fluorescence spectrometer with the PMT at 600 V and excitation and emission slits at 5 nm. Alternatively, fluorescence spectra were collected on a SPEX 1622 Fluorolog spectrometer with water cooled detector and double monochromator for comparative spectra. Figure 1 illustrates the absorbance profiles of the nanoparticle and dye used in the study. As stated by Kubin et al², the absorbance of dye was adjusted to below 0.1 for excitation at 480 nm and below. The subsequent dilutions were performed by analytical 1 in 10 dilutions of the original dye solution. The fluorescence spectra were collected from a thin path cell (10 mm x 4 mm). Due to such low concentrations of the dye ($< 10^{-7}$ M) between the 370 and 460 nm, the absorbance values become arbitrary and well below the error of the instrument and not reliable for QE comparison. This is illustrated in the graph of QE vs. excitation wavelength. The QE values rise above 1 in this range which is nonsensical leading to erroneous values. The plot shows that when the significant difference in the absorbance between QD high and QD low has a small effect on the QE at 360 and 480 nm excitation. In

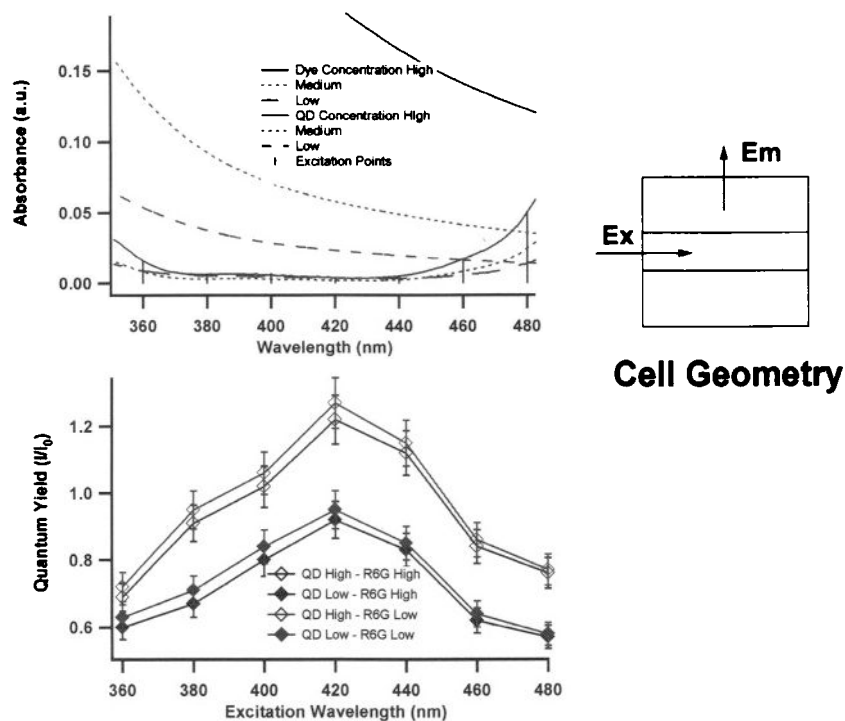


Figure A.1. Absorbance profiles of etched quantum dot in toluene and rhodamine 6G in ethanol at various concentrations (top), and quantum efficiency calculated using a thin path cell, 10 mm x 4 mm, at the indicated excitation wavelengths for the illustrated absorbance profiles (bottom).

addition, the dye absorbance has a negligible effect on the observed QE of the nanoparticle at an absorbance below 0.07.

When the cell geometry changes from thin path to square (10 mm x 10 mm), the change in the observed QE of the nanoparticle is drastically decreased. When the same solutions that were studied in the thin path cell are measured in a square cell, the QE is reduced by 3 orders of magnitude. Figure 2 illustrates the observed QE of InGaP nanoparticles obtained in a square cell geometry. Irrespective of the dye concentration, the observed QE is constant at 0.21 (+/- 0.05). The consideration of the path length of the fluorescence of the nanoparticle now becomes a significant issue. In the square geometry, the fluorescence is filtered through a more significant fraction of the solution. This can lead to self absorption by the nanoparticle. The intensity of the emission is minimized by the path length in the square geometry.

In addition, the comparison of the cell geometry was tested on a second highly luminescent nanoparticle. Recently we have reproduced Peng and co-workers [4] CdSe core nanoparticle that were reported to have a QE of 0.95. Using the thin path cell geometry a QE can be measured at 0.89 for the as prepared material. When the measurement was repeated in a square cell, a value of 0.25 was measured.

In conclusion, the most appropriate conditions to obtain highly luminescent nanoparticle QE's are in a thin path fluorescence cell. The dye and nanoparticle absorbance should be < 0.1 at the excitation wavelength and a dye of

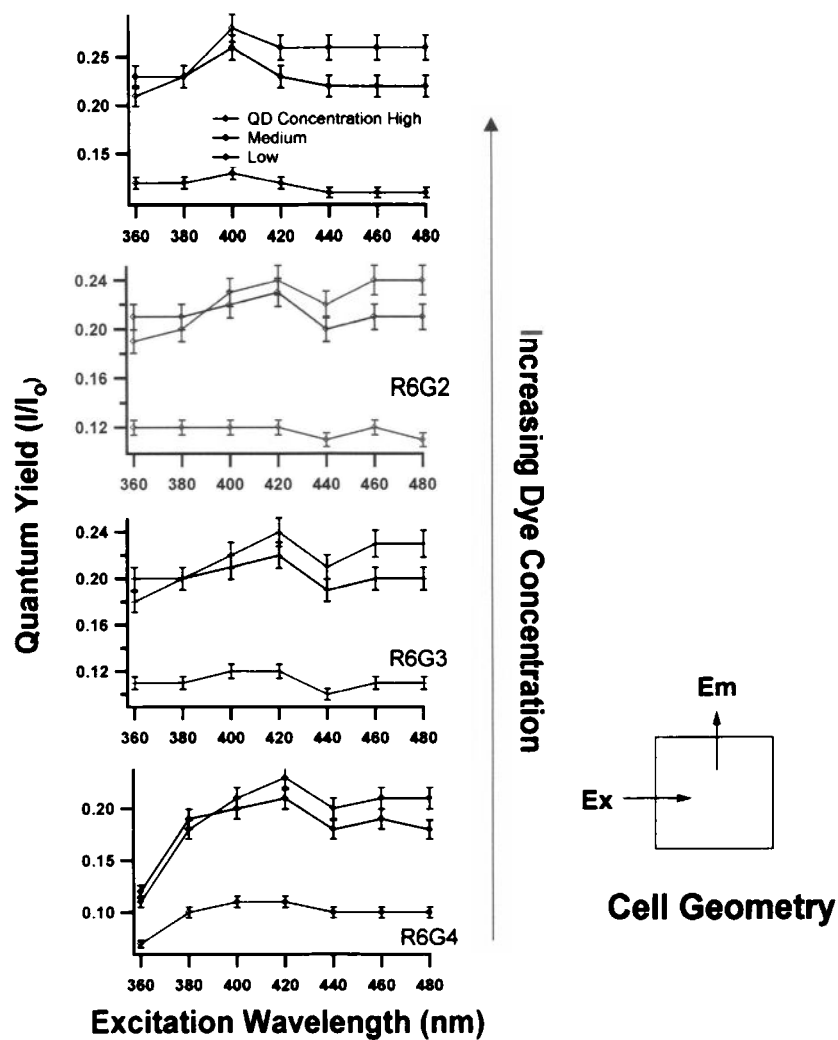


Figure A.2. Quantum efficiencies of quantum dots calculated from the same solutions illustrated in figure 1 but calculated from data obtained from a square cell, 10 mm x 10 mm.

comparable QE to the nanoparticle should be used that is stable in the respective solvent.

References

1. Wilcoxon et al., *J. Phys. Chem. B.*, **2005**, ASAP Article
2. Kubin et al., *J. of Lumin*, 27, **1982**, 455
3. Crosby et al., *J. of Phys. Chem.*, 75, **1971**, 991
4. Peng et al., *J. Am. Chem. Soc.*, 124, **2002**, 2049